Spatio-Temporal Properties of Coherent Backscattering of Light from Dense Disordered Media

Katsuhiro ISHII

Spatio-Temporal Properties of Coherent Backscattering of Light from Dense Disordered Media

A Dissertation
Submitted to
Graduate School of Engineering
Hokkaido University
for the Doctor Degree
(Engineering)

By
Katsuhiro ISHII

1998

Contents

Chapter 1

Introductory Remarks

1.1 Overview

Light will pass through a medium as long as physical properties related with the group velocity of the wave is uniform in the medium, which are characterized by its permittivity and permeability. Whenever there are spatio-temporal discrete variations in the permittivity and permeability due to the presence of particle or small-scale density fluctuations, part of the light radiation is scattered in all directions with some frequency changes. This is the *light scattering phenomenon.*

The scattering of light exists everywhere around us and is a quite familiar phenomenon. Hardly ever is light observed directly from its source. Most of the lights we see reach our eyes in an indirect way. Looking at an object such a tree, or a house, we see diffusely reflected sunlight. Looking at clouds in the sky, we see scattered sunlight. The blue and red colors of the sky in the daytime and sunset are caused by the scattering of sunlight by the air molecules. To give other interesting examples of optical phenomena in the atmosphere, the rainbow, the glory, the corona, and the halo are due to scattering either by aerosols, by ice crystals, or by water droplets. The turbidity in liquids or solids results from the scattering of light in which they are viewed, either by their constituent molecules or by suspended particles.

The scattering of light is one of the most important and powerful sources to provide information about the structure and dynamics of a medium. There are two classes of problems to extract the information from scattered light—the *direct scattering problem* and the *inverse scattering problem.* The direct scattering problem is to calculate theoretically, to observe experimentally, or to simulate numerically the scattering by a well-defined system. The inverse scattering problem is to characterize the system from a knowledge of light scattering obtained by experiment or observation. In the succeeding subsections, we summarize the development and application of the light scattering along the history of

scattering, classifying the four categories: light scattering formulation by a single particle, intensity of light scattering, spatial behavior of light scattering, and light propagation and scattering in random media.

1.1.1 Light scattering by a single particle

The concept of relating light scattering to media dates back to the 19th century when J. B. Richter reported observations of the phenomenon of light scattering by colloidal gold. After him, M. Faraday reported an observation of light scattering phenomenon by various metallic particles in colloidal suspension [1].

The first scientific light scattering experiment was performed by Tyndall in 1869 [2,3], who observed the natural light scattered by particles whose size was small compared with the incident wavelength and noticed the appearance of a blush hue in the scattering radiation. These experimental studies were followed from 1871 onwards by Lord Rayleigh's theoretical works [4,5]. He explained the observed color and polarization of the sunlight scattered in the atmosphere, where he concerned scattering from assemblies of non-interacting particles sufficiently small compared to the wavelength of light to be regarded as point-dipole oscillators. In 1881, he also expanded an approximate theory for particles of any shape and size having a relative refractive index approximately equal to unity and found that, for non-interacting, non-absorbing, and optically isotropic particles with sizes very smaller than the wavelength of the incident light, the amount of scattering should be inversely proportional to the fourth power of the wavelength [6]. The theory of scattering by particles with sizes very smaller than the wavelength of the incident light is now known as the *Rayleigh scattering* after Load Rayleigh's great contribution. He also explained the blue color of the sky and the red sunsets as due to the preferential scattering of blue light by the molecules in the atmosphere [7].

In subsequent papers [8-10], Rayleigh derived the full formula for sphere of arbitrary size. For these larger particles, there are fixed phase relations between waves scattered from different points of the same particle, but each scattering element of the particle was regarded as an independent point-dipole oscillator. Debye made further contributions to the theory of these large particles and extended the calculations to particles of non-

spherical shape [11]. Gans also contributed to the theory of large particles with the relative refractive index approximately equal to one [12-14]. The scattering by such a particle is now referred to as the *Rayleigh-Debye scattering* or, sometimes, the *Rayleigh-Gans scattering*.

The exact solution to the scattering by large particles with the relative refractive index much larger than one is a formidable and complex problem. There are not only fixed spatial relations between the scattering elements, there is also a strong dependence of the electric field amplitude on the position in the particle. Mie [15] and independently Debye [16] derived the exact solution of this problem only for the case of the sphere on the basis of the Maxwell's electromagnetic wave equation. This type of scattering is now referred to as the *Mie scattering*.

The scattering theory for a single isolated particle gives a basis of the direct scattering problem and still opened the way to investigation of scattering for random media. All above formulae has been well reviewed in major monographs: *Light Scattering by small particles* by H. C. van de Hulst [17] and *The Scattering of light and Other Electromagnetic radiation* by M. Kerker [18].

History in the subject about light scattering by a single particle was comprehensively reviewed by Logan [19], Lilienfeld [20], and Kerker [21].

1.1.2 Spatial behavior of the scattered light

In condensed media or whenever the scatterers are close to one another, a detailed computation of the induced electromagnetic field surrounding a particle becomes very complex because intermolecular interactions have to be taken into account. The intensity of scattering by condensed media was less than that predicted by single scattering formula by more than one order of magnitude. This effect was correctly attributed to the destructive interference between the wavelets scattered from different molecules. Smoluchowski [22] and Einstein [23] elegantly overcame this difficulties by considering the liquid to be a continuous medium and in which thermal fluctuations give rise to local inhomogeneities and thereby to density and concentration fluctuation, which is known as a *fluctuation theory of light scattering*. Moreover, these investigations continue to that on

the temporal behavior of the scattered light though they did not calculate the spectral profile of the scattered light. According to this theory, the intensity of the scattered light can be calculated from the mean-square magnitude of fluctuations in density on the basis of the statistical mechanics approach, assumed that the local density fluctuation in neighboring volume elements could be independent of one another. This theory could explain the scattering of light from pure liquids and predicted the enormous increase in the scattered light as the liquid-gas critical point was approach. This theory did not account for the angular dissymmetry of the strong scattering intensity in opalescent system but it is remains valid for the scattering angle of forward direction.

Ornstein and Zernike investigated the scattering behavior in opalescent system at the scattering angles deviated from the forward direction by including the effects of correlation between fluctuation of neighboring volume elements [24-26]. They showed that the marked increase of the scattered light in the turbidity of the fluids near the gas-fluid critical point is a consequence of the fact that the pair-correlation function of the system near its critical point becomes infinity in the long range. Later, the scattering from a system of particles whose positions are correlated under a government of the pair-correlation function was investigated by Zernike and Prins in connection with the theory of X-ray diffraction by liquids [27].

In foregoing phenomenological theory, no attempt was made to describe the effects of molecular optical anisotropy on the intensity, angular dependence, and polarization characteristics of the scattered light. Subsequent works dealt with a molecular theory of optically anisotropic scatterers [13,14,28]. In 1940s, Debye synthesized the Rayleigh-Debye scattering and the phenomenological points of view and developed the light scattering as a method for studying molecular weights, sizes, shapes, and interaction of molecules in the solution. This is now known as the *molecular light scattering*. Today, light scattering techniques apply successfully in the field of chemist, physics, meteorology, and biophysics [29].

As one of the interest application of light scattering technique, there is a scattering phenomenon by fractal aggregates of particles and fractal clusters. The angular intensity distribution of the *small-angle forward scattering* from fractal aggregates is given by a structure factor that is the Fourier transformation of the density-density correlation function

and decreases with an increase of the scattering angle in accordance with a power-law function, which provides the fractal dimension of the medium [30-32]. Schaefer and Martin[33] and Weitz et al. [34] measured the dimension of the colloidal aggregates of small silica particles and the aggregates of gold colloids, respectively.

1.1.3 Temporal behavior of the scattered light

There is a development in the studies of the light scattering phenomena in regard to the influence of the temporal behavior of the thermal fluctuation in the medium. Brillouin realized that the local density fluctuation in a liquid could be considered as thermally excited sound waves [35,36]. By retaining the temporal behavior of thermal phonons, Brillouin reported the first consideration of the spectrum of light scattered from a condensed medium. The fluctuations that propagated with a velocity give rise to "doublet" in the frequency distribution of the scattered light that were shifted in frequency by an amount proportional to the velocity of the fluctuation from the frequency of the incident light. Mandel'shtam had independently deduced the spectrum of light scattered by thermal phonons and obtained the frequency shift [37]. This two symmetrical frequency-shifted components around the unperturbed spectral line (*Rayleigh line*) are referred to as the *Mondel'shtam-Brillouin doublet*.

Gross experimentally observed the Mondel'shtam-Brillouin doublet and the Rayleigh line in his series of light scattering experiments on liquids [38,39]. Landau and Placzek theoretically explained the Rayleigh line using the non-propagating local temperature fluctuation [40]. They also showed that the ratio of the integrated intensity of the central line to that of the doublet is determined by the heat capacity ratio. A further fine structural change in the spectrum was founded by Raman in relation to the internal dynamics of molecules in the scatterers [41]. Though these studies suggest an applicability of the light scattering to dynamic problems in studying a whole phase of materials including gases, liquids, and solids, accurate measurements on the spectrum were quite difficult to be done due to the lack of intense monochromatic light sources and sufficiently high-resolution spectrometers.

The invention of the laser in early 1960s [42] changed this situation and these

measurements of frequency shift became a major tool for investigating the characteristics of the medium that contains small particles or small-scale local density fluctuation. In 1964, Pecora showed that the frequency profile of the scattered light was broadened by the diffusion process of the macromolecules and, under certain conditions, might be used to study rotational motion and flexing of macromolecules [43]. The half-width at the half-height of the central peak in the spectral profile is a direct measure of the translational diffusion coefficient of macromolecules. The first experiment using lasers as the source of incident light for the investigation of macromolecule solutions was by Cummins, Knable, and Yeh [44], and that for pure fluids near the critical point was by Ford and Benedek [45]. This method has been used in monitoring the time-dependence of the time-varying scattered intensity from a medium and measuring the dynamic characteristics of scatterers from the mid 1970s because of the later successfully determination of molecular weights and shapes. This is now referred as to the *dynamic light scattering* (DLS) [46,47].

The major variation in the DLS occurred in 1971, when Ware and Flygare reported DLS studies on bovine serum albumin in the static electric field [48,49]. The effect of applied electric field was to superimpose a constant drift velocity proportional to the electrophoretic mobility of the species on the random Brownian motion of the charged particles. The resulting spectrum was composed of peaks that are Doppler-shifted from the central frequency. This technique is referred to as the *Doppler shift spectroscopy* [47].

From an experimental point of view, the new spectroscopic technique called *optical-mixing* technique [50,51] contributed to the development of the DLS measurements. The optical-mixing technique classifies into the heterodyne and the homodyne methods. These techniques permitted measurements of very small frequency shifts of the scattered light by macromolecular solutions in diffusion process [44], in fluid flow [52], and pure fluids near the critical point [45]. Another important technique is the photon correlation spectroscopy where photons of scattered light are counted to compute the autocorrelation function, which permits the measurements of the extremely fast phase transition in real time [53].

The DLS technique has also been used in measurements of the spatial characteristics for fractal aggregates of particles and fractal clusters. For the fractal aggregates, the first

cumulant of the temporal autocorrelation function becomes a moment of the cluster-size distribution function and, therefore, DLS can be available to monitoring the time dependence of the growth process in the aggregation [31,54,55]. Weitz et al. measured the mean cluster radius of gold colloids with time and found the scaling behavior of it on time [54]. Feder et al. studied experimentally the aggregation of immunoglobulin proteins of the IgG type using DLS [55].

1.1.4 Light propagation and scattering in disordered media

The problems of light propagation and scattering in disordered media such as atmosphere, colloidal suspension, and biological media have become increasingly important in recent years. These media are, in general, randomly varying in space and time so that the amplitude and the phase of light may also fluctuate randomly in space and time, thus being described in the statistical sense. Because of the complexities in the phenomenon of the light scattering, an exact theoretical analysis of the optical field scattered by random media does not exist yet. In this section, we summarize the formulations and applications of the light propagation and scattering in disordered media.

When the particle density is tenuous, the single scattering theory is adequate. In the approximation called the *single scattering approximation*, it is assumed that the incident light from the source reaches the detector after encountering very few particles. The scattered light is assumed to be produced by a single scattering from a particle and the multiple scattering is assumed to be negligible. The formulation for this case has already mentioned in the preceding sections [17,18,46,47] and many applications have been done. The single scattering approximation is also identical to the Born approximation [56].

As the particle density increases, it is no longer possible to assume that the direct light is identical to the incident light, the attenuation due to the scattering and absorption along indirect paths has to be taken into account. The scattered light in this approximation is that the light is scattered once by a particle and attenuated by scattering and absorption during propagation along the scattering path. This approximation is referred to as *first-order multiple scattering* [57-60].

The two approximations mentioned above become inadequate as the particle density

further increases and the coherent intensity becomes comparable to or less than the incoherent intensity. The multiple scattering becomes dominant in this situation. Historically, there are two distinct approaches to describe the light propagation and scattering in dense disordered media. One is the *radiative transfer theory* of *transport theory* and the other is the *multiple scattering theory* [61-65].

The transport theory deals directly with the transport of energy through a medium containing particles but not with the wave equation. Even though diffraction and interference effects are included in the scattering and absorption phenomena by a single particle, the transport theory ignores these effects. Assuming with this theory, the scattered light field is assumed to be formed by the incoherent addition of scattered light rather than coherent addition since there is no correlation between the scattered fields. The basic differential equation is called the *equation of transfer* and is equivalent to be *Maxwell-Boltzmann collision equation* used in the kinetic theory of gasses [66] and the neutron transfer theory [67]. Although the transport theory was developed on the basis of the incoherent addition of the scattered light, it includes both the field correlation and the polarization effect via a Stokes matrix [68,69].

When the volume fraction becomes much greater than 1%, the diffusion approximation to the transport theory gives relatively simple and good solutions. It has been successfully used in the analysis on the optical fiber oximeter of blood on the assumption that the light scattered by many particles produces the diffuse intensity, the equation of transfer reduces to the diffusion equation [70-72]. The diffusion approximation holds only the field formed in the region far from the boundary and source because of the boundary condition.

The application of the diffusion approximation to the temporal behavior of the multiply scattered light is called the *diffusing wave spectroscopy* (DWS) [73-78]. This technique is an extension of DLS to the dense disordered media and uses the diffusive nature of the transport of photons. In the DWS theory that the trajectory traveled by an individual photon is described as a random walk and the temporal fluctuation of the scattered light is caused by displacements of particles due to the Brownian motion. The temporal autocorrelation function of the multiply scattered light is determined by a Laplace transformation of a total path-length distribution. The decreasing behavior of the temporal correlation function depends on the diffusion coefficient of particles and, thereby,

is able to apply to the measurements of the concentration and the size of the particle. An important feature is that DWS can probe the particle motion over the length scale of the scattering medium much shorter than the wavelength of light. Furthermore, Wo et al. and Bicout et al. extend the DWS technique to probe a velocity profile in liquid flow [79,80].

The other approach to formulate the multiple scattering, the *multiple scattering theory*, is originated from the basic differential equations such as the Maxwell's electromagnetic wave equation and the scalar wave equation. It is based on the differential of integral equations for statistical quantities such as a variance and a correlation function. Early studies on the multiple scattering include those by Ryde [81], Ride and Cooper [82], Foldy [83], Lax [84], and Synder and Scott [85]. Twersky extended these and obtained the Twersky's integral equation [68,69,86-90]. The analytic method based on Feynman diagram leads to the diagram representation of the Dyson equation for the average field and the Bethe-Salpeter equation for a correlation function as a kernel [91,92]. This is mathematically rigorous in the sense that in principle all the multiple scattering, diffraction, and interference effect can be included though, in practical, it is impossible to obtain analytically a formation which includes all these effects. The simplest and most useful approximation of this theory is the *first order smoothing approximation*. The relationship between the multiple scattering theory and the radiative transfer theory was investigated by many scientists and showed that they are equivalent to each other under a certain condition [68].

In mid 1980, Tsang and Ishimaru [93,94], Albada and Lagendijk [95], and Wolf and Maret [96] experimentally demonstrated the *coherent backscattering effect* or the *weak-localization of photons* which presented not only a deviation from diffusion approximation of light but also the precursor to the Anderson localization [93-106]. In the coherent backscattering effect, an intensity peak in the direction of retroreflection appears in the angular dependence of the backscattered light in contrast with the angular isotropy in the multiple scattered light under the diffusion approximation. The multiple scattering theory successfully explains this phenomenon due to the constructive interference between the light waves propagating along time-forward and -reversed paths. In the meteorological point of view, the intensity profile of the coherent backscattering contains the statistical information about the structure of a scattering medium and permits measurements of the

spatial characteristics of particle distribution.

The main purpose of this dissertation is to reveal spatio-temporal properties of the coherent backscattering of light from dense disordered media and apply it to measurements of a fractal aggregate of particles at the high concentration. In the dissertation, an angular intensity distribution and a temporal autocorrelation function of copolarized and cross-polarized light distributions backscattered multiply from dense disordered media are discussed. The investigation is conducted with the numerical simulations, experiments, and theoretical analyses.

1.2 Organization

The dissertation consists of ten chapters. Chapters 1 and 10 describe the Introductory Remarks and the Concluding Remarks, respectively.

Chapters 2-5 are concerned with spatio-temporal properties of the coherent backscattering of light from homogeneously disordered media. In Chapter 2, the basic theory of light scattering is given as preliminary preparations for the studies in the subsequent chapters. The theories of static light scattering by a single particle are discussed based on the Rayleigh scattering and Rayleigh-Debye scattering which is a key theory in our numerical simulation. Moreover, the coherent backscattering of light and DWS is explained under the diffusion approximation.

Chapter 3 reveals theoretically and experimentally the angular dependence of an autocorrelation function of the time-varying intensity fluctuation backscattered multiply from a dense disordered medium. The theory is derived under the framework of a diffusion approximation by renormalizing the coherent interference effect to the path-length distribution function. A comparison between the theoretical and experimental results is carried out by changing the diameter of scattering particles.

In chapter 4, the angular polarization dependence of the autocorrelation function of the multiply-backscattered intensity fluctuations is investigated by means of a Monte-Carlo simulation. The algorithm of the simulation is built on the basis of the Rayleigh-Debye scattering theory, which enable us to analyze the dependence of temporal statistics on the polarization and the particle size. A comparison of the numerical results with the

experimental ones and the diffusive transport theory gives qualitative discussions about the influence of coherent backscattering on temporal features of the multiply backscattered light. It makes clear the limitations of simulations and the diffusion approximation in the theory.

Chapters 5-9 are concerned with spatio-temporal properties of coherent backscattering of light from a fractal aggregate of particles. In Chapter 5, a free path-length distribution function (FPDF) of the multiply backscattered light is theoretically derived for the fractal aggregate of particles. An effective mean free path-length ℓ_D is newly introduced as a measure of randomness from the analogy of mean free path-length ℓ for the homogeneously random medium. The validity of the FPDF is confirmed by demonstrating agreement between the dimensions of media designed for particle distributions generated by a random walk following the FPDF and estimated by using a radius-gyration method. Moreover, the FPDF is applied to Monte Carlo simulations for the copolarized light backscattered multiply from the fractal aggregate of particles. As a result, the validity of the fractal model as the spatial structure of the particle aggregation and the applicability of the derived FPDF to the numerical simulation are confirmed from the results.

The polarized peak intensity distribution backscattered multiply from the fractal aggregate of particles is numerically investigated using Monte Carlo simulations in Chapter 6. It is confirmed only for the copolarized intensity component that an effective mean free path-length ℓ_{D} defined for a fractal medium has the same physical meaning as a mean free path-length ℓ for a homogeneously random medium. The spatial structure in the polarized peak intensity distribution of coherent backscattering of light is discussed on the basis of the two-dimensional Fourier transform relation between the peak intensity distributions in the far-field and the boundary planes. Finally, the empirical formulae of the decreasing slope in the copolarized and cross-polarized peak intensity distributions of the backscattering enhancement with relation to the fractal dimension are obtained from the results of the Monte-Carlo simulations.

In chapter 7, the copolarized and cross-polarized peak intensity distributions backscattered multiply from aggregated and non-aggregated particles in colloidal

suspension are experimentally studied. The decreasing behavior of the enhanced backscattering of light is studied by following the aggregation process of particles in the suspension. The dimensions of media are estimated by applying the decreasing slope of the peak intensity distributions to the empirical formulae obtained in Chapter 6. The relation between the estimated dimensions and the spatial structure of the particle aggregation is discussed to clarify the information that they possess. The dependence of the decreasing behavior in the intensity distribution on the absorption of suspensions is also investigated, and shows that these remarkable properties are independent of absorption in the colloidal suspension. As a result, the spatial properties of the intensity enhancement phenomenon show the ability to watch the aggregation process of particles and to estimate the dimension for dense media.

Chapter 8 devotes the investigation on the temporal autocorrelation function of time-varying intensity fluctuations backscattered multiply from the fractal aggregate of particles under Brownian motions in absorbent media by means of the Monte-Carlo simulation. Discussions are given with relation to the scattering-order distribution function to compare the simulations with the diffusion approximation. Angular dependence of the autocorrelation function on the dimension and the absorption of the medium are clarified.

Chapter 9 is concerned with a study on the temporal autocorrelation function of time-varying intensity fluctuation backscattered multiply from a cluster-cluster structure on the basis of the results obtained in the preceding chapter. The cluster-cluster structure in the fractal medium is replaced with a polydisperse random medium by renormalizing clusters to particles with different sizes. As the particle size-distribution, a simple summation of particles with two radii, a Gaussian function, and a power law function are used in the numerical simulations. The investigation is carried out about how the cluster-cluster structure affects a decreasing rate of the peak intensity distribution and a relaxation time in the autocorrelation function of the time-varying intensity. As a result, it is concluded that the temporal autocorrelation function of the time-varying light intensity scattered multiply from the cluster-cluster structure is applicable to measure the average cluster size of the particle aggregations.

In Chapter 10, this dissertation concludes by surveying the main results obtained in every chapter.

Chapter 2

Theoretical Basis

2.1 Single scattering

This section is concerned with the detail descriptions of the Rayleigh and Rayleigh-Debye scattering theories. The Rayleigh scattering theory contains the important concept of the radiation from an electric dipole oscillator, which gives the basis of the Rayleigh-Debye scattering theory. The Rayleigh-Debye scattering theory adopted in the numerical simulation has advantages in applicability to the light scattering by a particle with arbitrary shape and in simplicity of description on the polarization though it is restricted in the relation between the size and the relative refractive index of the particle.

2.1.1 Rayleigh scattering theory

Illuminating by a linearly polarized light, a dielectric particle electrically polarizes due to the displacements of electrons in the particle. Assumed that the particle is much smaller than the wavelength of light, the instantaneous electromagnetic field induced by the incident light is uniform inside the particle and only the electric phenomenon is effective, thus the particle being simply considered as an electric dipole.

The internal electric field $\boldsymbol{E}$ generated by applying external electric field $\boldsymbol{E}_0$ is parallel to the external electric field and given by

$$\boldsymbol{E} = \frac{3\varepsilon_2}{\varepsilon_1 + 2\varepsilon_2}\boldsymbol{E}_0 , \tag{2.1}$$

where ε_1 and ε_2 are permittivities of the particle and the external medium, respectively. Outside the particle, the field is composed of the incident electric field, which an electric dipole generates. If the particle is assumed to be optically isotropic, the induced electric dipole in the particle also is parallel to the external electric field and the dipole moment is

given by

$$\boldsymbol{P} = 4\pi\varepsilon_2\alpha\boldsymbol{E}_0, \tag{2.2}$$

where α denotes the polarizability of the particle. For the case of the spherical particle with the radius a, the polarizability α is expressed as

$$\alpha = \frac{\varepsilon_1 - \varepsilon_2}{\varepsilon_1 + 2\varepsilon_2} a^3. \tag{2.3}$$

If the incident light oscillates harmonically at an angular frequency ω, the induced electrical dipole follows synchronously so that

$$\boldsymbol{P}\, e^{j\omega t} = 4\pi\varepsilon_2\alpha\boldsymbol{E}_0 e^{j\omega t}, \tag{2.4}$$

where t denotes time and exponential factor describes the time-dependent factor. An oscillating electric dipole radiates electromagnetic wave in all directions as the scattered light.

According to the electromagnetic theory [107], the electric field of radiation by the oscillating electric dipole at the origin is given as

$$\boldsymbol{E}_s(\boldsymbol{r}) = -\frac{\exp(ikr)}{4\pi\varepsilon_2 r}\boldsymbol{k}\times\boldsymbol{k}\times\boldsymbol{P} \tag{2.5}$$

at a position $\boldsymbol{r}$ far away from the origin, where $\boldsymbol{k}$ denotes the wave vector and time dependence is dropped. By substituting Eq. (2.2) to Eq. (2.5), the relation between incident and the scattered electric field is obtained as

$$\boldsymbol{E}_s(\boldsymbol{r}) = -\frac{\alpha\exp(ikr)}{r}\boldsymbol{k}\times\boldsymbol{k}\times\boldsymbol{E}_0. \tag{2.6}$$

The expression in terms of intensities of incident and scattered light, I_0 and I_s, is given by taking square of both sides in Eq. (2.6) as

$$I_s = \frac{k^4|\alpha|^2}{r^2} I_0 \sin^2\chi, \tag{2.7}$$

where χ denotes the angle measured from the scattering direction to the dipole axis. Moreover, the integration of the scattered light over whole solid angle leads the scattering cross section,

$$C_{sca} = \frac{8}{3}\pi k^4|\alpha|^2. \tag{2.8}$$

Equation (2.7) shows that the amount of scattering is inversely proportional to the forth

power of wavelength for the case that the single scattering is dominant, which causes the blue sky or the red sunset. On the other hand, Eq. (2.5) means that the polarization of scattered light can be simply calculated from the incident polarization and the scattered direction.

2.1.2 Rayleigh-Debye scattering theory

The Rayleigh-Debye scattering theory is valid for the particles satisfying the assumption:

(a) The relative refractive index, m, is close to 1: $|m-1| \ll 1$.

(b) The phase shift is small : $2ka|m-1| \ll 1$.

Here a is a dimension of the particle. For spherical particle, a denotes the radius. There is a restriction on the size of particles with a given refractive index and, however, this restriction is not as severe as that of Rayleigh scattering theory.

The concept of the Rayleigh-Debye scattering is that the each volume element in the scattering particle gives rise to the Rayleigh scattering independently of the other volume element. Because the field inside the particle may be approximated by the incident field under the conditions (a) and (b), each volume element is illuminated by the incident beam and the scattered light from it leaves the particle without any scattering by others. However, the light waves scattered in a given direction by all volume elements interfere because of different paths that scattered light propagate along.

To show that the mathematical expression of the Rayleigh-Debye scattering theory, the polarizability $\alpha' = \alpha / V$ per unit volume is introduced since it is proportional to the volume of a particle V. The Rayleigh scattering by a volume element dV is expressed as

$$\boldsymbol{E}_s(\boldsymbol{r}) = -\frac{\alpha' \exp(ikr)}{r} \boldsymbol{k} \times \boldsymbol{k} \times \boldsymbol{E}_0 dV \,. \tag{2.9}$$

Taking the interference effect into account, the Rayleigh-Debye scattering is given as

$$\boldsymbol{E}_s(\boldsymbol{r}) = -\int_V \frac{\alpha' \exp(ikr) \exp[i\delta(\theta,\phi,\boldsymbol{r}')]}{r} \boldsymbol{k} \times \boldsymbol{k} \times \boldsymbol{E}_0 dV \,, \tag{2.10}$$

where $\delta(\theta,\phi,\boldsymbol{r}')$, θ, ϕ ,and $\boldsymbol{r}'$ denote the relative phase difference, the zenith angle of the scattered direction, the azimuth angle of the scattered direction, and the position in the

particle, respectively. This integration over the particle reduces to

$$\boldsymbol{E}_s(\boldsymbol{r}) = -\frac{\alpha' V \exp(ikr)}{r} \boldsymbol{k} \times \boldsymbol{k} \times \boldsymbol{E}_0 \; R(\theta, \phi) \tag{2.11}$$

by using new function known as a form factor,

$$R(\theta, \phi) = \frac{1}{V} \int_V \exp[i\delta(\theta, \phi, \boldsymbol{r})] dV \,. \tag{2.12}$$

Equation (2.11) demonstrates that the Rayleigh-Debye scattering theory brings an angular dependence into the Rayleigh scattering theory by the form factor $R(\theta, \phi)$ and, still, retains the simplicity in polarization of the scattered light. These are the reason why we adopt the Rayleigh-Debye scattering theory in our numerical simulator.

Figure 2.1 show a geometry to calculate the form factor, where O and the vector OP being an arbitrary origin $\boldsymbol{r}$, respectively. $\boldsymbol{n}$ and $\boldsymbol{m}$ are defined as the unit vectors in the direction for the incident light and for the scattered light, respectively. The path from the infinitely distant source to P is longer by $\boldsymbol{r} \cdot \boldsymbol{n}$ than the path to O. The path from P to the infinitely distant detector is shorter by $\boldsymbol{r} \cdot \boldsymbol{m}$ than the path from O. The phase lag of light scattered at P over the light scattered at O is found by adding the two effects and multiply by k and $\delta = k\boldsymbol{r} \cdot (\boldsymbol{m} - \boldsymbol{n})$.

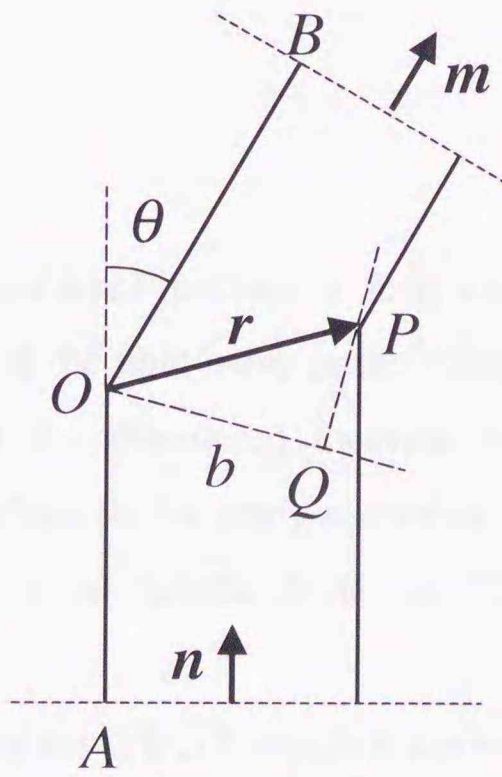

Fig. 2.1 A geometry of the Rayleigh-Debye scattering. $\boldsymbol{m}$ and $\boldsymbol{n}$ denote the directions of the incident and scattered light, respectively.

The vector $\boldsymbol{m} - \boldsymbol{n}$ has the length $2\sin(\theta/2)$ along the bisectrix of the directions of $\boldsymbol{m}$ and $-\boldsymbol{n}$. In Fig. 2.1, the bisectrix of $\angle AOB$ is OQ. The plane brought through P perpendicular to this bisectrix cuts it at Q so that $OQ = b$. All points in this plane have same phase shift of $\delta = kb2\sin(\theta/2)$. This suggests an integration by means of slice perpendicular to the bisectrix. If each slice has an area $S(b)$ and a thickness db, the phase function reduces to the analytical form as

$$R(\theta,\phi) = \frac{1}{V}\int_v S(b)\exp[i2kb\sin(\theta/2)]db\,. \tag{2.13}$$

For the spherical particle with the radius a, it is ready to calculate the phase function by substituting $x = ka$, $b = za$, $u = 2x\sin(\theta/2)$, and $d = zu$ to Eq. (2.13). Then, the slice has a thickness adz and a radius $a\sqrt{1-z^2}$ so that the phase function is obtained as

$$R(\theta,\phi) = \frac{1}{V}\int \exp(izu)\pi a^2\left(1-z^2\right)a\,dz = G(u), \tag{2.14}$$

where

$$G(u) = \frac{3}{2}\int_0^1 \cos zu\cdot\left(1-z^2\right)dz = \frac{3}{u^3}(\sin u - u\cos u) = \left(\frac{9\pi}{2u^3}\right)^{1/2} J_{3/2}(u). \tag{2.15}$$

This phase function is used in our simulation to determine the scattered direction of light at the scattering event.

2.2 Multiple scattering

The light propagation in the disordered medium is dealt with the radiative transfer theory which regards the propagation of the light wave as the transport of the light energy [108]. When the volume density of the disordered medium is much grater than 1%, the propagation of light is fully randomized by many scattering events and the transport of the light energy becomes diffusive as the thermal diffusion. This is known as the diffusion approximation of light.

Let us consider a specific intensity $I(\boldsymbol{r},\hat{s})$, which is the average power flow density in a given direction defined by a unit vector $\hat{s}$ within a unit frequency band centered at frequency ν within a unit solid angle, to be incident to a cylindrical elementary volume

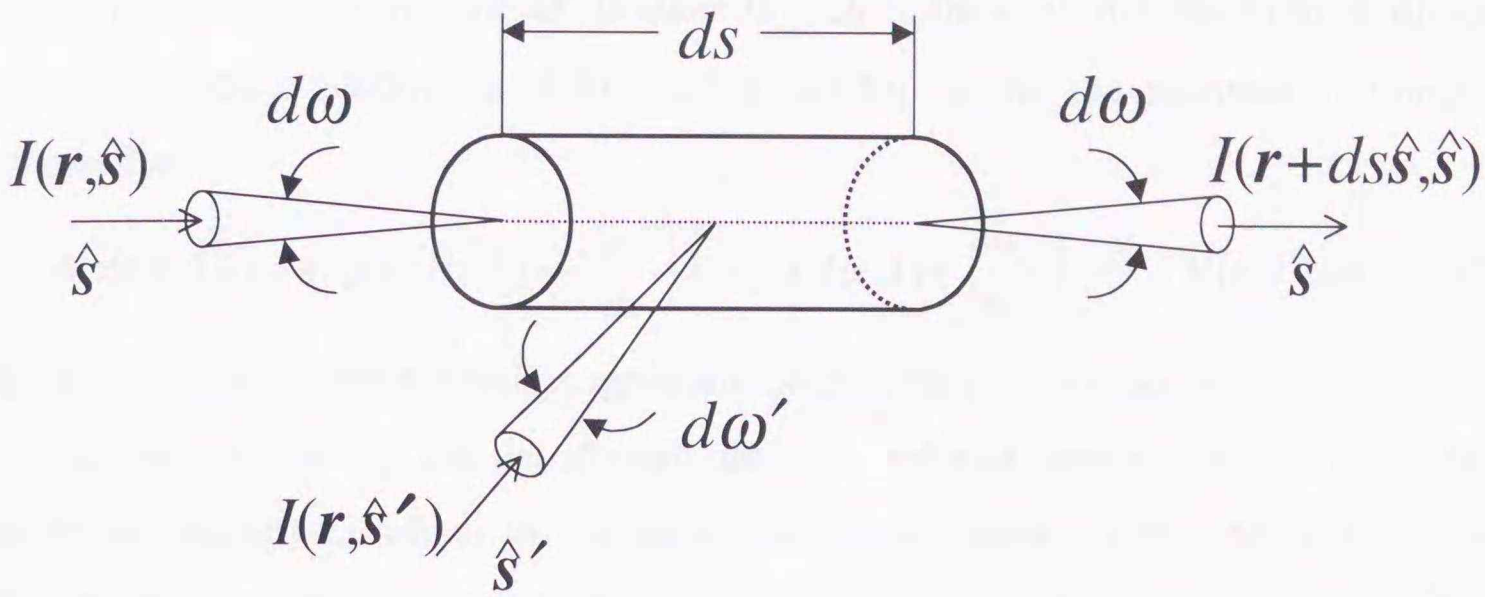

Fig. 2.2 Propagation of specific intensity upon the volume *ds* in the direction **s** and scattering of the specific intensity upon the volume *ds* from the direction **s**′ into the direction **s**.

with a unit cross section and length *ds*, as shown in Fig. 2.2. The volume *ds* contains $\rho\, ds$ particles where ρ is the number of particles in a unit volume and is called the number density. Each particle absorbs the power $\sigma_a I$ and scatters the power $\sigma_s I$. Therefore, the specific intensity decreases by

$$dI(\boldsymbol{r},\hat{\boldsymbol{s}}) = -\rho ds(\sigma_a + \sigma_s) I(\boldsymbol{r},\hat{\boldsymbol{s}}) = -\rho ds \sigma_t I(\boldsymbol{r},\hat{\boldsymbol{s}}) \tag{2.16}$$

for the volume *ds*. At the same time, the specific intensity increases because a portion of the specific intensity $I(\boldsymbol{r},\hat{\boldsymbol{s}}')$ incident to the volume from other directions $\hat{\boldsymbol{s}}'$ is scattered into the direction $\hat{\boldsymbol{s}}$ and added to the specific intensity $I(\boldsymbol{r},\hat{\boldsymbol{s}})$. The scattered specific intensity in the direction $\hat{\boldsymbol{s}}$ due to the incident specific intensity $I(\boldsymbol{r},\hat{\boldsymbol{s}}')$ is expressed as

$$\frac{\sigma_t}{4\pi} p(\hat{\boldsymbol{s}},\hat{\boldsymbol{s}}') I(\boldsymbol{r},\hat{\boldsymbol{s}}') d\omega' \tag{2.17}$$

in terms of a phase function $p(\hat{\boldsymbol{s}},\hat{\boldsymbol{s}}')$ of a single particle. Summing up the incident specific intensity from all directions $\hat{\boldsymbol{s}}'$, the specific intensity scattered into direction $\hat{\boldsymbol{s}}$ by $\rho\, ds$ particles in the volume *ds* is given by

$$\frac{\rho\sigma_t}{4\pi} ds \int_{4\pi} p(\hat{\boldsymbol{s}},\hat{\boldsymbol{s}}') I(\boldsymbol{r},\hat{\boldsymbol{s}}') d\omega', \tag{2.18}$$

where the integration over all ω' is taken to include the contributions from all directions $\hat{s}'$. The total contributions of Eq. (2.16) and Eq. (2.18), the *equation of transfer*, is obtained as

$$\mathrm{div}\left[I(\boldsymbol{r},\hat{s})\hat{s}\right]=\hat{s}\cdot\mathrm{grad}\,I(\boldsymbol{r},\hat{s})=\frac{I(\boldsymbol{r},\hat{s})}{ds}=-\rho\sigma_t I(\boldsymbol{r},\hat{s})+\frac{\rho\sigma_t}{4\pi}\int_{4\pi}p(\hat{s},\hat{s}')I(\boldsymbol{r},\hat{s}')d\omega'. \qquad (2.19)$$

In Eq. (2.19), it is assumed that no quantum-mechanical emission occurs.

The total intensity I can be divided into the reduced incident intensity I_{ri} and the diffusion intensity I_d, which are the no-scattered and scattered components, respectively. The reduced incident intensity decreases due to scattering and absorption and satisfies the equation

$$\frac{I_{ri}(\boldsymbol{r},\hat{s})}{ds}=-\rho\sigma_t I_{ri}(\boldsymbol{r},\hat{s}). \qquad (2.20)$$

Since the total intensity $I(\boldsymbol{r},\hat{s})=I_{ri}(\boldsymbol{r},\hat{s}')+I_d(\boldsymbol{r},\hat{s}')$ satisfies Eq. (2.19), the diffuse intensity satisfies the equation

$$\frac{I_d(\boldsymbol{r},\hat{s})}{ds}=-\rho\sigma_t I_d(\boldsymbol{r},\hat{s})+\frac{\rho\sigma_t}{4\pi}\int_{4\pi}p(\hat{s},\hat{s}')I_d(\boldsymbol{r},\hat{s}')d\omega'+\varepsilon_{ri}(\boldsymbol{r},\hat{s}), \qquad (2.21)$$

where $\varepsilon_{ri}(\boldsymbol{r},\hat{s})$ is the equivalent source function

$$\varepsilon_{ri}(\boldsymbol{r},\hat{s})=\frac{\rho\sigma_t}{4\pi}\int_{4\pi}p(\hat{s},\hat{s}')I_{ri}(\boldsymbol{r},\hat{s}')d\omega' \qquad (2.22)$$

generated by the reduced incident intensity.

The integration of Eq. (2.21) over all 4π of solid angle leads to the conservation of energy

$$\mathrm{div}\,\boldsymbol{F}_d(\boldsymbol{r})=-\rho\sigma_a cU_d(\boldsymbol{r})+\rho\sigma_s cU_{ri}(\boldsymbol{r}), \qquad (2.23)$$

where $\boldsymbol{F}(\boldsymbol{r})$ and $U(\boldsymbol{r})$ denote the flux density vector and the energy density at a point $\boldsymbol{r}$ and are given by

$$\boldsymbol{F}(\boldsymbol{r})=\int_{4\pi}I(\boldsymbol{r},\hat{s})\hat{s}d\omega \qquad (2.24)$$

and

$$U(\boldsymbol{r})=\frac{1}{c}\int_{4\pi}I(\boldsymbol{r},\hat{s})d\omega, \qquad (2.25)$$

respectively. Equation (2.23) physically means that the outflow of the flux of diffuse

intensity per unit volume is equal to the energy of the reduced incident intensity scattered in unit volume minus the energy of the diffuse intensity absorbed in unit volume.

At this stage, it is assumed that the diffuse intensity encounters many particles so that it is scattered almost uniformly in all directions and its angular distribution is almost uniform, which is called the diffusion approximation. However, the angular distribution can not be constant because if it were constant, the flux would be zero and there would be no net energy propagation. Therefore, the diffuse intensity should have slightly more magnitude in the direction of the net flux flow than in the backward direction and is approximated by

$$I_d(\boldsymbol{r},\hat{\boldsymbol{s}}) \cong \frac{c}{4\pi} U_d(\boldsymbol{r}) + C\boldsymbol{F}_d(\boldsymbol{r})\cdot\hat{\boldsymbol{s}}\,, \tag{2.26}$$

where C denotes a constant. The constant C can be determined by noting that

$$F_d(\boldsymbol{r}) = \boldsymbol{F}_d(\boldsymbol{r})\cdot\hat{\boldsymbol{s}}_f = \int_{4\pi} I_d(\boldsymbol{r},\hat{\boldsymbol{s}})\hat{\boldsymbol{s}}\cdot\hat{\boldsymbol{s}}_f\, d\omega\,, \tag{2.27}$$

where $F_d(\boldsymbol{r})$ and $\hat{\boldsymbol{s}}_f$ denote the magnitude and direction of $\boldsymbol{F}_d(\boldsymbol{r})$. Substituting Eq. (2.26) into Eq. (2.27), $C = 3/4\pi$ is obtained and, therefore, the diffusion approximation for the diffuse intensity is given by

$$I_d(\boldsymbol{r},\hat{\boldsymbol{s}}) = \frac{c}{4\pi} U_d(\boldsymbol{r}) + \frac{3}{4\pi}\boldsymbol{F}_d(\boldsymbol{r})\cdot\hat{\boldsymbol{s}}\,. \tag{2.28}$$

Equation (2.28) may be regarded as the first two terms of a Taylor's expansion of I_d in terms of the powers of $\hat{\boldsymbol{s}}\cdot\hat{\boldsymbol{s}}_f$ and, therefore, the second term of Eq. (2.28) must be considerably smaller the first term: $cU_d(\boldsymbol{r}) >> |\boldsymbol{F}_d(\boldsymbol{r})|$.

Substitution of Eq. (2.28) into Eq. (2.21) leads to the equation of transfer under the diffusion approximation as

$$\begin{aligned}\frac{I_d(\boldsymbol{r},\hat{\boldsymbol{s}})}{ds} &= \frac{c}{4\pi}\hat{\boldsymbol{s}}\cdot\operatorname{grad}U_d + \frac{3}{4\pi}\hat{\boldsymbol{s}}\cdot\operatorname{grad}(\boldsymbol{F}_d\cdot\hat{\boldsymbol{s}}) \\ &= -\frac{\rho\sigma_t c}{4\pi}U_d - \frac{3\rho\sigma_t}{4\pi}\boldsymbol{F}_d\cdot\hat{\boldsymbol{s}} + \frac{\rho\sigma_s c}{4\pi}U_d + \frac{3\rho\sigma_t}{4\pi}\boldsymbol{F}_d\cdot\hat{\boldsymbol{s}}\,p_1 + \varepsilon_{ri}\end{aligned}\,, \tag{2.29}$$

where p_1 is given by

$$p_1 = \int_{4\pi} p(\hat{\boldsymbol{s}},\hat{\boldsymbol{s}}')\hat{\boldsymbol{s}}\cdot\hat{\boldsymbol{s}}'\, d\omega'\,. \tag{2.30}$$

Equation (2.29) presents the averaged forward scattering minus the averaged backward scattering of a single particle. In the derivation of Eq. (2.29), it is also assumed that the

phase function $p(\hat{\boldsymbol{s}},\hat{\boldsymbol{s}}')$ is only a function of the angle between $\hat{\boldsymbol{s}}$ and $\hat{\boldsymbol{s}}'$.

The integration of Eq. (2.29) multiplied by $\hat{\boldsymbol{s}}$ over all 4π solid angle derives a equation

$$\int_{4\pi} \frac{I_d(\boldsymbol{r},\hat{\boldsymbol{s}})}{ds}\hat{\boldsymbol{s}}\, d\omega = \frac{c}{4\pi}\operatorname{grad} U_d(\boldsymbol{r}) = -\frac{3\rho\sigma_t}{4\pi}(1-p_1)\boldsymbol{F}_d(\boldsymbol{r}) + \frac{3}{4\pi}\int_{4\pi}\varepsilon_{ri}(\boldsymbol{r},\hat{\boldsymbol{s}})\hat{\boldsymbol{s}}\, d\omega, \qquad (2.31)$$

which is relates to the conservation of momentum because the left side means the average increase of energy flux density vector over all directions at a point $\boldsymbol{r}$ and

$$\text{momentum} = \frac{\text{energy}}{c}.$$

The quantity $\sigma_t(1-p_1)$ presents the cross section of isotropicically scattered component and is called the *transport cross section* σ_{tr}. Physically, Eq. (2.31) means that the momentum of diffuse intensity decreases due to the isotropic scattering and the absorption and increases the anisotropic scattering of reduced incident intensity.

Equation (2.23) gives div $\boldsymbol{F}_d$ in terms of U_d and equation (2.31) gives grad U_d in terms of $\boldsymbol{F}_d$. Therefore, $\boldsymbol{F}_d$ can be eliminated from these two equations by taking $\boldsymbol{F}_d$ from Eq. (2.31) and substituting it into Eq. (2.23). As a result, the differential equation for the energy density U_d of the diffuse intensity is obtained as

$$D\nabla^2 U_d(\boldsymbol{r}) - \frac{c}{\ell_a}U_d(\boldsymbol{r}) = S(\boldsymbol{r}) \qquad (2.32)$$

in terms of diffusion coefficient $D = \ell^* c/3$, the absorption length $\ell_a = 1/\rho\sigma_a$, the free path-length $\ell = 1/\rho\sigma_s$, the transport mean free path-length $\ell^* = 1/\rho\sigma_{tr}$, and the source function due to the reduced incident intensity

$$S(\boldsymbol{r}) = -\frac{c}{\ell}U_{ri}(\boldsymbol{r}) + \ell^*\nabla\cdot\int_{4\pi}\varepsilon_{ri}(\boldsymbol{r},\hat{\boldsymbol{s}})\hat{\boldsymbol{s}}\, d\omega. \qquad (2.33)$$

Equation (2.32) is the fundamental static diffusion equation for the averaged diffuse intensity and means that the propagation of the diffuse intensity becomes diffusive in a dense disordered medium similarly to the thermal diffusion.

In the preceding discussion, it is assumed that the specific intensity, flux density, and energy density are static, whereas they vary in time in practical cases. In the situation, the conservation of energy expressed in Eq. (2.23) must be modified and, then, is given by

$$\operatorname{div}\boldsymbol{F}_d(\boldsymbol{r},t) = -\frac{\partial U_d(\boldsymbol{r},t)}{\partial t} - \rho\sigma_a c U_d(\boldsymbol{r},t) + \rho\sigma_s c U_{ri}(\boldsymbol{r},t), \qquad (2.34)$$

where the first term shows a decrease of the energy density of the diffuse intensity at a point $\boldsymbol{r}$ and a time t due to the variation of the energy density in time. Therefore, the diffusion equation shown in Eq. (2.32) is also modified as

$$D\nabla^2 U_d(\boldsymbol{r},t)-\frac{c}{\ell_a}U_d(\boldsymbol{r},t)-\frac{\partial U_d(\boldsymbol{r},t)}{\partial t}=S(\boldsymbol{r},t), \tag{2.35}$$

which is the time-dependent diffusion equation.

Once the energy density is found by solving the diffusion equation under the appropriate boundary condition, the flux density and the diffuse intensity are calculated from Eq. (2.31) and Eq. (2.28) as

$$\boldsymbol{F}_d(\boldsymbol{r},t)=-D\nabla U_d(\boldsymbol{r},t) \tag{2.36}$$

and

$$I_d(\boldsymbol{r},\hat{\boldsymbol{s}},t)=\frac{c}{4\pi}U_d(\boldsymbol{r},t)-\frac{3}{4\pi}D[\nabla U_d(\boldsymbol{r},t)]\cdot\hat{\boldsymbol{s}}\,, \tag{2.37}$$

respectively.

The boundary condition for the diffuse intensity I_d is that there should be no diffuse intensity at the surface entering the medium from out side:

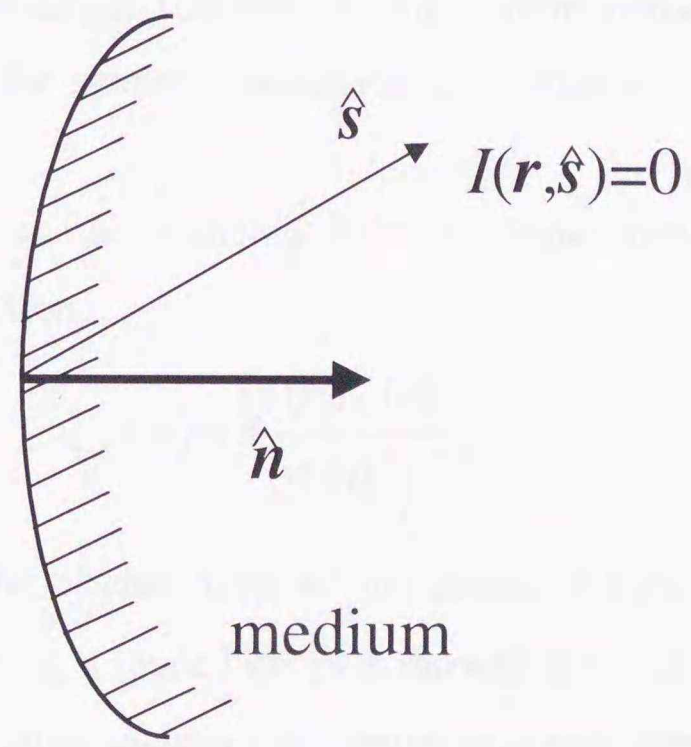

Fig. 2.3 Geometry showing the directions $\boldsymbol{s}$ and $\hat{\boldsymbol{n}}$ for the boundary condition

$$I_d(\boldsymbol{r},\hat{\boldsymbol{s}},t)=0 \tag{2.38}$$

when it is pointed inward, as shown in Fig. 2.3. However, According to the diffusion approximation, the diffuse intensity has a simple angular distribution given by Eq. (2.28) and the diffusion approximation is given in terms of a single scalar function U_d. Thereby, the boundary condition can not be satisfied exactly and some approximate boundary condition must be considered. One such approximation is the condition at a surface the total diffuse flux directed inward must be zero:

$$\int_{2\pi} I_d(\boldsymbol{r},\hat{\boldsymbol{s}})(\hat{\boldsymbol{s}}\cdot\hat{\boldsymbol{n}})d\omega = 0\,, \tag{2.39}$$

where $\hat{\boldsymbol{n}}$ is a unit vector normally directed inward and the integration is performed over 2π solid angle in the hemisphere $\hat{\boldsymbol{s}}\cdot\hat{\boldsymbol{n}} > 0$. The boundary condition given by Eq. (2.39) can be expressed in terms of only energy density of the diffuse light as

$$\frac{c}{4}U_d(\boldsymbol{r},t) - \frac{D}{2}[\nabla U_d(\boldsymbol{r},t)]\cdot\boldsymbol{n} = 0\,. \tag{2.40}$$

2.2.1 Temporal correlation function

The diffusion approximation of light permits the theoretical analysis of the temporal dependence of intensity fluctuation scattered multiply from dense disordered medium though it can not apply to the spatial dependence of fluctuation, that is referred to as speckle.

The temporal fluctuation of the scattered light is characterized by the normalized temporal autocorrelation function,

$$\gamma(\tau) = \frac{\langle E(\tau)E^*(0)\rangle}{\langle |E(0)|^2\rangle}, \tag{2.41}$$

where $E(\tau)$ and τ denote the electric field of the scattered light and the delay time, respectively. To calculate $\gamma(\tau)$, a single light path through the medium is first considered as shown in Fig 2.4. For a given sequence of scattering events at positions $\boldsymbol{r}_1,\ldots,\boldsymbol{r}_n$ and with corresponding successive wave vector transfer $\boldsymbol{q}_i = \boldsymbol{k}_i - \boldsymbol{k}_{i-1}$, the product of the scattered electric fields at times τ and 0 is given as

$$E^{(n)}(\tau)E^{(n)*}(0) = \left|E^{(n)}(0)\right| \exp\left\{ j\sum_i \boldsymbol{k}_i \cdot [\boldsymbol{r}_{i+1}(\tau) - \boldsymbol{r}_i(\tau)] \right\}$$
$$\times \left|E^{(n)}(0)\right| \exp\left\{ j\sum_i \boldsymbol{k}_i \cdot [\boldsymbol{r}_{i+1}(0) - \boldsymbol{r}_i(0)] \right\} \qquad (2.42)$$
$$= \left|E^{(n)}(0)\right|^2 \exp\left[j\sum_i \boldsymbol{q}_i \cdot \Delta\boldsymbol{r}_i(\tau) \right],$$

where $\Delta\boldsymbol{r}_i(\tau) = \boldsymbol{r}_i(\tau) - \boldsymbol{r}_i(0)$ denotes the distance that the *i*-the particle moves in a time *t*.

Assuming that the fields propagating along different paths are added incoherently, the average contribution to the normalized autocorrelation function of all paths with the order *n* is

$$\left\langle E^{(n)}(\tau)E^{(n)*}(0) \right\rangle = I_0 P(n) \left\langle \prod_i \exp[j\boldsymbol{q}_i \cdot \Delta\boldsymbol{r}_i(\tau)] \right\rangle. \qquad (2.43)$$

In Eq. (2.43), $P(n)$ is the fraction of the total scattered intensity I_0 in the *n*-th order paths and $\langle \cdots \rangle$ denotes the average operation over both the particle displacement $\Delta\boldsymbol{r}(\tau)$ and the distribution of the scattering vector $\boldsymbol{q}$. Under the assumption that successive scattering events are uncorrected and particles displace due to Brownian motion, the average over the particle displacement $\Delta\boldsymbol{r}(\tau)$ in Eq. (2.43) yields

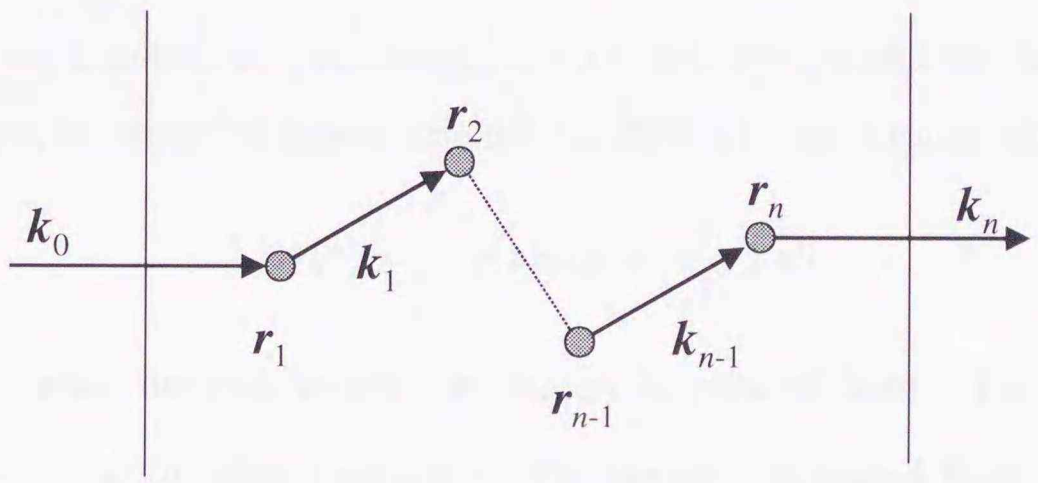

Fig. 2.4 A schematic illustration of a path that light propagates along. The positions of scatterers and wave vectors of the scattered light are labeled as $\boldsymbol{r}_1, \boldsymbol{r}_2, \ldots, \boldsymbol{r}_{n-1}, \boldsymbol{r}_n$ and $\boldsymbol{k}_1, \boldsymbol{k}_2, \ldots, \boldsymbol{k}_{n-1}, \boldsymbol{k}_n$. $\boldsymbol{k}_0$ denotes the wave vector of the incident light.

$$\left\langle E^{(n)}(\tau)E^{(n)*}(0)\right\rangle = I_0 P(n)\left\langle \exp\left[-\frac{q^2\left\langle \Delta r^2(\tau)\right\rangle}{6}\right]\right\rangle_q^n, \tag{2.44}$$

where $\langle\cdots\rangle_q$ denotes the average operation over the distribution of the scattering vector q. For the simple diffusion, $\left\langle \Delta r^2(\tau)\right\rangle = 6D_p\tau$, where D_p being the diffusion coefficient of particles. The average over the distribution of the scattering vector q yields

$$\left\langle E^{(n)}(\tau)E^{(n)*}(0)\right\rangle = I_0 P(n)\exp\left[-\left\langle q^2\right\rangle D_p n\tau\right] \tag{2.45}$$

with the first term of the cumulant expansion. In Eq. (2.45), $\left\langle q^2\right\rangle$ means the average over the scattering angle and is given as $2k^2\ell/\ell^*$ in terms of the mean free path-length ℓ and transport mean free path-length ℓ^*. The simple expression for the contribution of the n-th order scattering path to the autocorrelation function is obtained as

$$\left\langle E^{(n)}(\tau)E^{(n)*}(0)\right\rangle = I_0 P(n)\exp\left(-\frac{2\tau\ell}{\tau_0\ell^*}n\right), \tag{2.46}$$

where $\tau_0 \equiv 1/D_p k^2$.

The total field autocorrelation function $\gamma(\tau)$ is obtained by summing over the scattering paths of all orders as

$$\gamma(\tau) = \sum_{n=1}^{\infty} p(n)\exp\left(-\frac{2\tau\ell}{\tau_0\ell^*}n\right). \tag{2.47}$$

Taking the replacement of path-length $s = n\ell$ and approximating the sum over n by integral over s, the temporal autocorrelation function is finally formulated as

$$\gamma(\tau) = \int_0^{\infty} p(s)\exp\left(-\frac{2\tau}{\tau_0\ell^*}s\right)ds, \tag{2.48}$$

where $p(s)$ means the path-length distribution function of light. Eq. (2.48) shows that the temporal autocorrelation function of the multiply scattered light is described as a Laplace transform of the path-length distribution function which is obtained from the solution of the diffusion equation under the appropriate boundary condition.

2.2.2 Coherent backscattering of light

The intensity of light backscattered multiply from dense disordered media does not distribute uniformly and gives rise to an intensity peak in the direction of retroreflection. This is known as the *coherent backscattering of light* or *weak localization of photons*. Fig. 2.5 shows intensity distributions of the backscattered light from suspended polystyrene latex spheres. The radiative transport theory of light can not explain this phenomenon. The mechanism of coherent backscattering of light and the method to renormalize it into diffusion approximation are taken into consideration.

Figure 2.6 shows a schematic illustration of two light paths. Both light have the same frequency. The light along the path A has the electric field A_{inc} with wave vector $\boldsymbol{k}_{Ainc}$. After n scattering events at positions $\boldsymbol{r}_1,\ldots,\boldsymbol{r}_n$ and with corresponding successive wave vector transfer $\boldsymbol{q}_i = \boldsymbol{k}_i - \boldsymbol{k}_{i-1}$, the light emerges with electric field A_f and wave vector $\boldsymbol{k}_{Af}$. The light along the path B with electric field B_{inc} and wave vector $\boldsymbol{k}_{B\mathrm{inc}}$ propagates in the

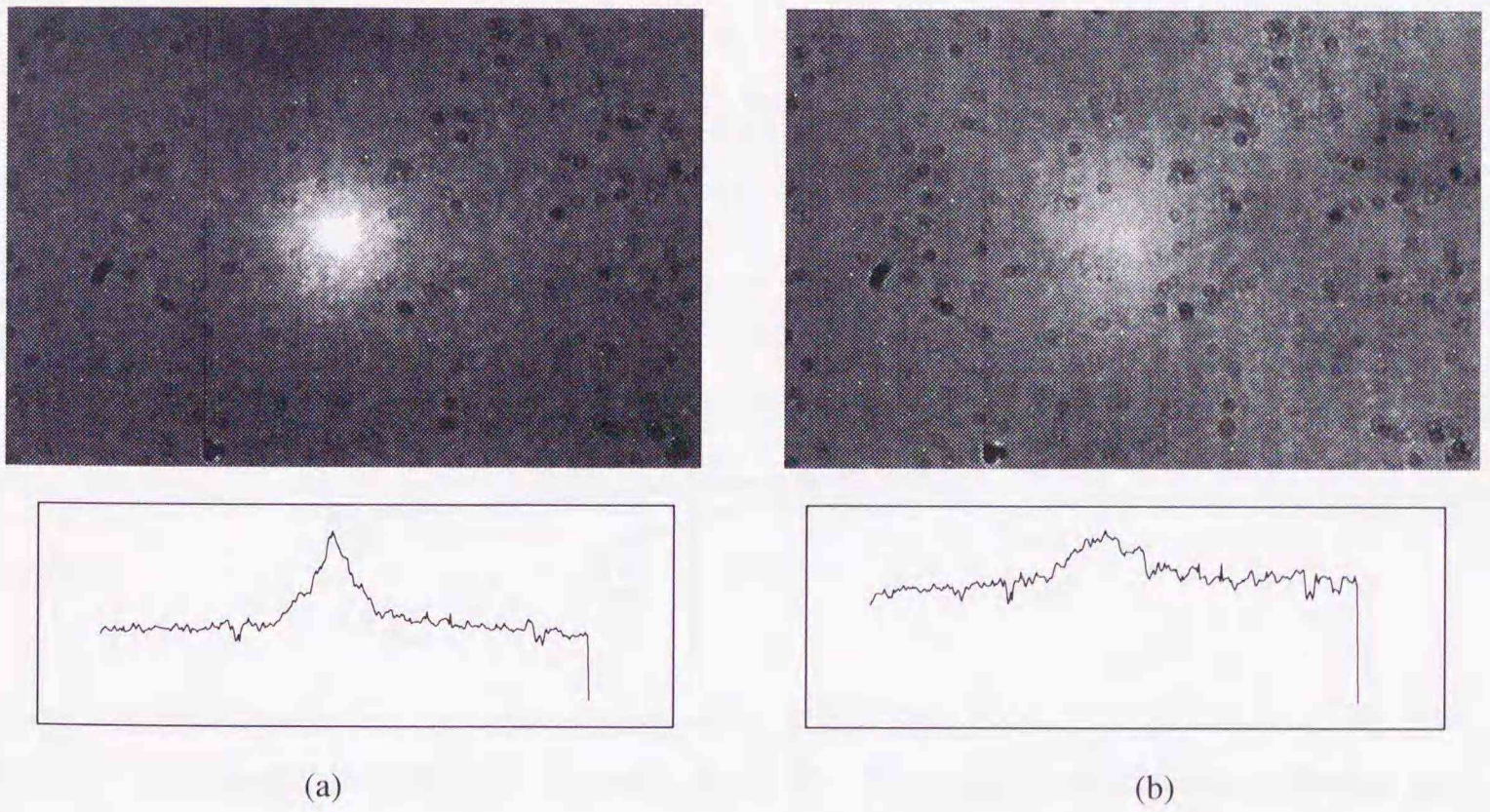

(a) (b)

Fig. 2.5 Typical intensity distributions of multiply backscattered light under the influence of enhanced backscattering for (a) copolarized component and (b) cross-polarized component. The graphs below the pictures show the corresponding intensity distributions along the line through the direction of retroreflection.

inverse order along the same path and emerges with electric field B_f and wave $\boldsymbol{k}_{Bf}$. Then, the electric fields A_f and B_f are given by

$$A_f = A_{inc} G_A \exp\left\{ j\left[\boldsymbol{k}_{Ainc} \cdot (\boldsymbol{r}_1 - \boldsymbol{R}_0) + \boldsymbol{k}_{Af} \cdot (\boldsymbol{r}_0 - \boldsymbol{r}_n) + \sum_i \boldsymbol{k}_i \cdot (\boldsymbol{r}_{i+1} - \boldsymbol{r}_i) \right] \right\} \tag{2.49}$$

and

$$B_f = B_{inc} G_B \exp\left\{ j\left[\boldsymbol{k}_{Binc} \cdot (\boldsymbol{r}_n - \boldsymbol{R}_0) + \boldsymbol{k}_{Bf} \cdot (\boldsymbol{r}_0 - \boldsymbol{r}_1) + \sum_i -\boldsymbol{k}_i \cdot (\boldsymbol{r}_i - \boldsymbol{r}_{i+1}) \right] \right\}, \tag{2.50}$$

respectively, where G_A and G_B denote Green's functions.

When the coherent plane wave is incident to the medium and the scattered light is detected in far field, A_{inc}=B_{inc}, $\boldsymbol{k}_{inc}$= $\boldsymbol{k}_{Ainc}$= $\boldsymbol{k}_{Binc}$, and $\boldsymbol{k}_f$= $\boldsymbol{k}_{Af}$= $\boldsymbol{k}_{Bf}$ are hold. Supposing that $G_A = G_B$,

$$\frac{A_o}{B_o} = \exp\{ j[(\boldsymbol{k}_{inc} + \boldsymbol{k}_o) \cdot (\boldsymbol{r} - \boldsymbol{r}')] \}, \tag{2.51}$$

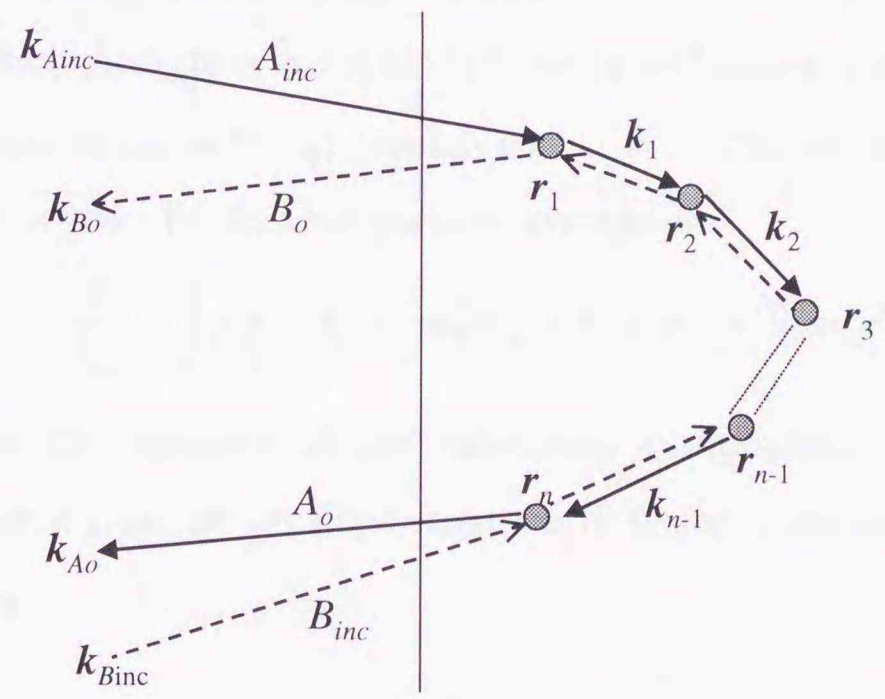

Fig. 2.6 A schematic illustration of two paths, A and B. The positions of scatterers and wave vectors of the scattered light are labeled as $\boldsymbol{r}_1$, $\boldsymbol{r}_2$,…., $\boldsymbol{r}_{n-1}$, $\boldsymbol{r}_n$ and $\boldsymbol{k}_1$, $\boldsymbol{k}_2$,….,$\boldsymbol{k}_{n-1}$, $\boldsymbol{k}_n$, respectively. The light propagating along path A is incident with the electric field A_{inc} and the wave vector $\boldsymbol{k}_{Ainc}$ and emerges with the electric field A_f and the wave vector $\boldsymbol{k}_{Af}$. The light propagating along path B is likewise incident with the electric field B_{inc} and the wave vector $\boldsymbol{k}_{Binc}$ and emerges with the electric field B_f and the wave vector $\boldsymbol{k}_{Bf}$.

in terms of $\boldsymbol{r} = \boldsymbol{r}_1$ and $\boldsymbol{r}' = \boldsymbol{r}_n$. Equation (2.51) means that the light waves along the paths A and B are coherent and interfere with each other in the direction of retroreflection $\boldsymbol{k}_o = -\boldsymbol{k}_{inc}$. Therefore, the intensity of light has to be added coherently and is given as

$$\begin{aligned}(A_o + B_o)(A_o^* + B_o^*) &= |A_o|^2 + |B_o|^2 + A_o B_o^* + A_o^* B_o \\ &= 2|A_o|^2 \{1 + \mathrm{Re}\exp[j(\boldsymbol{k}_{inc} + \boldsymbol{k}_o)\cdot(\boldsymbol{r} - \boldsymbol{r}')]\} \\ &= 2|A_o|^2 \{1 + \cos[(\boldsymbol{k}_{inc} + \boldsymbol{k}_o)\cdot(\boldsymbol{r} - \boldsymbol{r}')]\}.\end{aligned} \tag{2.52}$$

Inside the brackets, the first term is equal to the intensity added incoherently and the second term shows the interference between light waves propagating along time-forward and –reversed paths, which are referred to as the incoherent component and the coherent component, respectively. Equation (2.52) demonstrates that the intensity in the direction of retroreflection is twice compared with the incoherent component and the coherent component decreases with an increase of the backscattering angle. It is called the *coherent backscattering effect*.

The above explanation considers the contributions of only two paths. Taking the all contributions of the intensity of light wave backscattered from the medium, the probability density $p(\boldsymbol{r}, \boldsymbol{r}')$, which the light is incident at position $\boldsymbol{r}$ and emerges at position $\boldsymbol{r}'$, have to be calculated because equation (2.52) depends on $\boldsymbol{r} - \boldsymbol{r}'$. The normalized intensity of the backscattered light is given by the configuration average as

$$\frac{I}{I_{inc}} = \int p(\boldsymbol{r}, \boldsymbol{r}')\{1 + \cos[(\boldsymbol{k}_{inc} + \boldsymbol{k}_o)\cdot(\boldsymbol{r} - \boldsymbol{r}')]\} d\boldsymbol{r} d\boldsymbol{r}', \tag{2.53}$$

where I_{inc} denotes the intensity of the incoherent component. Using the diffusion approximation, $p(\boldsymbol{r}, \boldsymbol{r}')$ can be obtained from the diffusion equation and the appropriate boundary condition.

2.3 Numerical analysis of multiple scattering

2.3.1 Method of ray tracing

The light propagating in a medium undergoes successive scattering events from n particles located at $\boldsymbol{r}_1, \boldsymbol{r}_2, \cdots, \boldsymbol{r}_n$, thus generating the scattered lights with wave vectors $\boldsymbol{k}_1, \boldsymbol{k}_2, \cdots, \boldsymbol{k}_n$ at

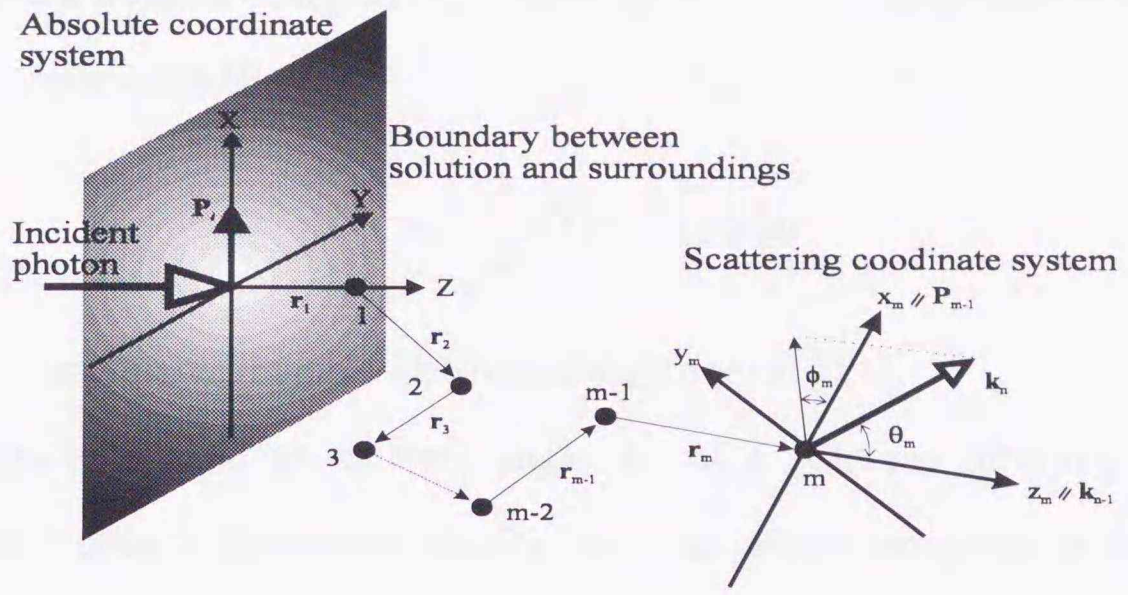

Fig. 2.7 Coordinate systems defined in the simulation.

every event. The scattering geometry is shown in Fig.2.7, where two different Cartesian coordinate systems are defined for the absolute coordinates (X,Y,Z) and the m-th scattering coordinates (x_m,y_m,z_m). The absolute coordinate system is defined in a XY plane between a scattering medium and surroundings. In this case, an origin is located at the entrance position of the incident light with the wave vector $\boldsymbol{k}_i$ and the polarization $\boldsymbol{P}_i$, and Z and X axes coincide with $\boldsymbol{k}_i$ and $\boldsymbol{P}_i$, respectively. The scattering coordinate system is defined with an origin at the m-th scattering point corresponding to the last scattering event. In this system, z_m and x_m axes coincide with the wave vector $\boldsymbol{k}_{m-1}$ and the polarization $\boldsymbol{P}_{m-1}$, respectively. After undergoing n scattering events, the scattered light emerges from the medium at the point of $\boldsymbol{r}_n=(X_n,Y_n,Z_n)$ with the wave vector $\boldsymbol{k}_n$. The Monte Carlo simulations are conducted by tracing all scattering events and paths. The propagation of the light is simulated by generating the random numbers of the distance between the successive particles and the scattering angle at the event following a free path-length distribution function and a Rayleigh-Debye scattering phase function, respectively.

The distance vector $\boldsymbol{r}$ between the successive scattering events is distributed following a free path-length distribution function as

$$p(r)=\frac{1}{\ell}\exp\left(-\frac{r}{\ell}\right) \tag{2.54}$$

In simulations, a random number r_m following Eq.(2.54) is generated by means of the transformation method[109]:

$$u_r = \int_0^{r_m} p(r)dr \Big/ \int_0^{\infty} p(r)dr \tag{2.55}$$

where u_r is a random real number distributed uniformly in [0,1].

A zenith angle θ_m and an azimuth angle ϕ_m of a scattered direction at the m-th scattering event obey a probability density functions which are given in the Rayleigh-Debye scattering theory as the phase functions of

$$p(\theta) \propto (\sin qa - q\cos qa)^2 / q^6 a^6 \tag{2.56}$$

and

$$p(\phi) \propto \sin^2\theta \sin^2\phi + \cos^2\phi\,, \tag{2.57}$$

respectively, where $q = 2k\sin(\theta/2)$ and $k = |\boldsymbol{k}_i| = |\boldsymbol{k}_m|$. In simulations, the zenith angle θ_m and the azimuth angle ϕ_m at the m-th scattering event are generated as random real numbers distributed in the interval $[0,\pi]$ and $[0,2\pi]$ using the transformation method defined as

$$u_\theta = \frac{\int_0^{\theta_m} p(\theta)\sin\theta\, d\theta}{\int_0^{\pi} p(\theta)\sin\theta\, d\theta} \tag{2.58}$$

and

$$u_\phi = \frac{\int_0^{\phi_m} p(\phi)d\phi}{\int_0^{2\pi} p(\phi)d\phi}, \tag{2.59}$$

where u_θ and u_ϕ denote random real numbers distributed uniformly in [0, 1].

In the Rayleigh-Debye scattering theory, the scattering produces a sequence of rotation

of the polarization vector. When the last scattered wave with the polarization $\boldsymbol{P}_{m-1}$ is incident to the m-th particle, the polarization $\boldsymbol{P}_m$ radiated from the m-th scattering event is given by

$$\boldsymbol{P}_m = -\boldsymbol{k}_m \times (\boldsymbol{k}_m \times \boldsymbol{P}_{m-1}) \equiv \boldsymbol{S}(\boldsymbol{k}_m)\boldsymbol{P}_{m-1}. \tag{2.60}$$

After undergoing n scattering events, the scattered light emerges from the medium at the location of $\boldsymbol{r}_n$ with the wave vector $\boldsymbol{k}_n$. The final polarization vectors $\boldsymbol{P}_{nf}$ is obtained as

$$\boldsymbol{P}_{nf} = \boldsymbol{S}_{nf}\boldsymbol{P}_i = \prod_{i=1}^{n} \boldsymbol{S}_i \boldsymbol{P}_i , \tag{2.61}$$

where the scattering matrix for the final polarization with the n-th scattering order is defined as

$$\boldsymbol{S}_{nf} = \begin{pmatrix} S_{XXn} & S_{XYn} & S_{XZn} \\ S_{YXn} & S_{YYn} & S_{YZn} \\ S_{ZXn} & S_{ZYn} & S_{ZZn} \end{pmatrix}. \tag{2.62}$$

In Eq.(2.62), S_{UV} denotes an amplitude component whose polarization is transformed from the positive-V direction to the positive-U direction. In simulations, the direction and the polarization of the scattered wave at each event are determined in the scattering coordinate system. On the other hand, a product of polarization matrices is estimated in the absolute coordinate system after taking the transform of the coordinates.

2.3.2 Coherent backscattering of light

The intensity is detected by changing the detecting position on the X axis of the observation plane, thus the intensity distribution as a function of the backscattering angle being obtained. In addition, the copolarized and cross-polarized components of the light intensity scattered along the path with the n th scattering order are observed through an analyzer placed in parallel with and perpendicular to direction of the polarization of light

incident onto the medium, respectively. Under such a consideration, the copolarized and cross-polarized components of the scattered light are formulated as

$$I_{nco} = \begin{cases} \dfrac{I_{nXf} + I_{nXr}}{I_{nXf} + I_{nYf}} & (n = 1) \\ \dfrac{I_{nXf} + I_{nXr}}{I_{nXf} + I_{nYf}} \left(1 + \Gamma_{nX} \cos \Phi_n\right) & (n \neq 1) \end{cases} \tag{2.63}$$

and

$$I_{ncross} = \frac{I_{nYf} + I_{nYr}}{I_{nXf} + I_{nYf}} \left(1 + \Gamma_{nY} \cos \Phi_n\right), \tag{2.64}$$

respectively, where $\Phi_n \approx k\theta X$ denotes the phase difference due to the distance X between the incident and emerging points. Two pair of the two intensities of I_{nXf} and I_{nXr} and I_{nXf} and I_{nXr} are obtained by

$$\begin{cases} I_{nXf} = \left(S_{XX} \cos\theta + S_{ZX} \sin\theta\right)^2 \\ I_{nXr} = \left(S_{XX} \cos\theta + S_{XZ} \sin\theta\right)^2 \end{cases}, \tag{2.65}$$

and

$$\begin{cases} I_{nYf} = \left(S_{YX}\right)^2 \\ I_{nYr} = \left(S_{XY}\right)^2 \end{cases}, \tag{2.66}$$

respectively, and the total intensity propagating in the forward direction is defined by

$$I_{nf} = S_{nXX}^2 + S_{nYX}^2 . \tag{2.67}$$

In Eqs. (2.63) and (2.64), Γ_{nX} and Γ_{nY} indicate degrees of the correlation between the waves propagating in time-forward and -reversed directions and are defined as

$$\Gamma_{nX} = \frac{\sqrt{I_{nXf} I_{nXr}}}{I_{nXf} + I_{nXr}} \tag{2.68}$$

and

$$\Gamma_{nY} = \frac{\sqrt{I_{nYf} I_{nYr}}}{I_{nYf} + I_{nYr}}, \tag{2.69}$$

respectively.

The total intensities of the multiply backscattered light are given by adding contributions of all paths with all scattering orders as

$$I_{co} = \sum_{n=1}^{\infty} \langle I_{nco} \rangle_{ex} \tag{2.70}$$

and

$$I_{cross} = \sum_{n=1}^{\infty} \langle I_{ncross} \rangle_{ex}, \tag{2.71}$$

respectively, where $\langle \cdots \rangle_{ex}$ stands for the ensemble average over the distribution of the emerging positions from the medium.

2.3.3 Temporal autocorrelation function

The statistical properties of a time-varying amplitude $E(\tau,\theta)$ scattered multiply in the direction of the backscattering angle θ from the disordered medium are described by a temporal autocorrelation function as

$$\Gamma(\tau,\theta) = \langle E(\tau,\theta) E^*(0,\theta) \rangle = \sum_{n=1}^{\infty} \langle |E_n(0,\theta)|^2 \rangle_{ex} \left\langle \prod_{m=1}^{n} \exp[i\boldsymbol{q}_m \cdot \Delta \boldsymbol{r}_m(\tau)] \right\rangle_{\boldsymbol{q},\Delta \boldsymbol{r}}, \tag{2.72}$$

where $\boldsymbol{q}_m = \boldsymbol{k}_m - \boldsymbol{k}_{m-1}$ and $\Delta \boldsymbol{r}_m(\tau) = \boldsymbol{r}_m(\tau) - \boldsymbol{r}_m(0)$ denote the scattering vector at the m-th scattering event and the displacement of the m-th particle motion in time τ, respectively. $E_n(0,\theta)$ is a contribution of the amplitude scattered along a path of n scattering events to the total scattered field, and $\langle \cdots \rangle_{ex}$ stands for the ensemble average over the distribution of the exit positions from the medium. The second term of Eq. (2.72) is a contribution of the

total phase change due to the displacement of all n scattering particles, $\langle\cdots\rangle_{q,\Delta r}$ standing for the ensemble average over both the distributions of the scattering vector $\boldsymbol{q}_m$ and the particle displacement $\Delta \boldsymbol{r}_m(\tau)$. By assuming that the displacements of all particles are produced by Brownian motions, $\Delta \boldsymbol{r}_m(\tau)$ obeys the zero-mean Gaussian statistics. Therefore, the ensemble average of the second term with respect to the displacement $\Delta \boldsymbol{r}_m(\tau)$ yields

$$\Gamma(\tau,\theta)=\sum_{n=1}^{\infty}\left\langle |E_n(0,\theta)|^2\right\rangle_{ex}\left\langle \exp\left(-\frac{4\tau}{\tau_0}\sum_{m=1}^{n}\sin^2\frac{\theta_m}{2}\right)\right\rangle_{q}, \tag{2.73}$$

where $\tau_0=\left(D_p k_i^2\right)^{-1}$ is an order of the single scattering relaxation time in a homodyne autocorrelation function and $q_m=2k_i\sin\theta_m/2$ has been used in the derivation, D_p standing for the diffusion constant of particles depending on the particle size and the notations of $q_m=|\boldsymbol{q}_m|$ and $k_i=|\boldsymbol{k}_i|=|\boldsymbol{k}_m|$ being used. Furthermore in Eq. (2.73), the ensemble average of the second term may be reduced to that over the distribution of the scattering angle at each scattering event. To investigate the dependence of the temporal autocorrelation function on the backscattering angle θ, the normalized autocorrelation function is finally obtained as

$$\gamma(\tau,\theta)=\frac{\Gamma(\tau,\theta)}{\Gamma(0,\theta)}=\sum_{n=1}^{\infty}p(n,\theta)\left\langle \exp\left(-\frac{4\tau}{\tau_0}\sum_{m=1}^{n}\sin^2\frac{\theta_m}{2}\right)\right\rangle_{\theta_m}, \tag{2.74}$$

where $p(n,\theta)$ denotes a fraction of the total intensity leaving in the direction of the backscattering angle θ after scattering along a path of n scattering events and is defined by

$$p(n,\theta)=\left\langle \left|E_n(0,\theta)\right|^2 \right\rangle_{ex} \Big/ \sum_{n=1}^{\infty} \left\langle \left|E_n(0,\theta)\right|^2 \right\rangle_{ex}$$

$$= \begin{cases} \left\langle I_{nco} \right\rangle_{ex} \Big/ \sum_{n=1}^{\infty} \left\langle I_{nco} \right\rangle_{ex} & (co-polarized\ case) \\ \left\langle I_{ncross} \right\rangle_{ex} \Big/ \sum_{n=1}^{\infty} \left\langle I_{ncross} \right\rangle_{ex} & (cross-polarized\ case) \end{cases} . \qquad (2.75)$$

Equations (2.72) and (2.75) are evaluated by using the results of Monte Carlo simulations. The scattering order n, all the scattering angles $\theta_m \left(m=1,\cdots,n\right)$ at all scattering events, the coordinates (X,Y,Z) of the position where the wave leaves from the medium, and the nth order amplitudes of the scattering wave, $\boldsymbol{P}_{nf}$ and $\boldsymbol{P}_{nr}$, for the incidence of a single photon are obtained numerically in the simulations. By changing a seed of the random generator, 10^6 data for a given scattering order n were obtained.

Chapter 3

Theoretical Analysis under the Diffusive Transport Theory of Photons

3.1 Introduction

A phenomenon of the coherent backscattering from a highly disordered medium has attracted much attention in the research fields of light scattering and mesoscopic physics. One of the characteristic spatial features is that the multiply backscattered light produces an intensity peak in the direction of retroreflection, which is called an enhanced backscattering in the medium [93,96]. This phenomenon results from the constructive interference between the scattered lights traveling along the time-forward and -reversed paths in the medium. Thus, the wave nature of the scattered light plays an important role in generating the enhanced backscattering phenomenon [97-99]. By increasing the fraction of the scattering medium, the propagation of light can be regarded as a diffusive transport of photons because of many scattering events. The diffusive transport theory of photons simplifies greatly the theoretical analyses. Therefore, the theory established under the framework of a diffusion approximation has succeeded in describing the spatial features of enhanced backscattering phenomena by renormalizing the coherent interference effect to the path-length distribution function [100].

On the other hand, the scattered field varies in time due to the Brownian motion of scattering particles [101]. It is theoretically shown under the framework of a diffusion approximation that a temporal correlation function of the multiply-scattered light field can be expressed as a Laplace transform of the path-length distribution function. The studies based on the diffusive transport theory of photons have been developed to the Diffusion Wave Spectroscopy [73-75]. Since the wave nature of the scattered light plays an important role in the temporal properties of dynamic multiple scattering, it can be expected that there exists the angular dependence of temporal features under the influence of the

constructive interference between the scattered lights traveling along the time-forward and -reversed paths. The angular dependence of the temporal correlation of multiply-scattered intensity fluctuations was discussed quantitatively [101], demonstrated experimentally [76], and connected with that of the path-length distribution function [77].

So far, there has not been an analytical form of the temporal autocorrelation function in which the coherent interference effect in the enhanced backscattering is taken into consideration. The purpose of this chapter is to reveal theoretically and experimentally the angular correlation dependence of time-varying fluctuations of light scattered multiply from a dense disordered medium. The theory is derived under the framework of a diffusion approximation by renormalizing the coherent interference effect to the path-length distribution function following an analogy with the theoretical derivation in the spatial feature. A comparison between the theory and experiments is conducted by changing the diameter of scattering particles.

3.2 Theory

The light enters a scattering medium at a given location, undergoes a large number of scattering events, and exits at a certain location from the medium. For a large number of scattering events, the propagation of light in a dense disordered medium can be described as a diffusion process of the photons. The theory of diffusing wave spectroscopy gives an autocorrelation function of the scattered amplitude which is related with a Laplace transform of the path-length distribution function. However, it fails to describe how the coherent backscattering effect influences an angular dependence of the autocorrelation function of time-varying light fluctuations of light scattered multiply from the medium. We analyze the coherent backscattering effect on the temporal autocorrelation function of multiply-backscattered light fluctuations on the basis of a photon diffusion approximation.

To consider the coherent backscattering effect, the incident and exit directions of scattered waves which interfere constructively need to be introduced to the path-length distribution function. Then, the autocorrelation function of multiply-scattered light fluctuations is rewritten on the amplitude by

$$\gamma(\tau,\boldsymbol{k}_i,\boldsymbol{k}_f)=\int_0^\infty P(s,\boldsymbol{k}_i,\boldsymbol{k}_f)\exp\left(-\frac{2\tau}{\tau_0\ell^*}s\right)ds, \tag{3.1}$$

where ℓ^* and $\tau_0=(D_p k^2)^{-1}$ denote a transport mean free path-length and an order of the single scattering relaxation time in a homodyne autocorrelation function, respectively, in which D_p indicates a diffusion constant. In Eq. (3.1), $P(s,\boldsymbol{k}_i,\boldsymbol{k}_f)$ denotes the path-length distribution function and is defined by [78]

$$P(s,\boldsymbol{k}_i,\boldsymbol{k}_f)=\frac{I(s,\boldsymbol{k}_i,\boldsymbol{k}_f)}{\int_0^\infty I(s,\boldsymbol{k}_i,\boldsymbol{k}_f)ds}. \tag{3.2}$$

where $I(s,\boldsymbol{k}_i,\boldsymbol{k}_f)$ is the fraction of photons which are incident to the medium with a wave vector $\boldsymbol{k}_i$, travel along the path s, and leave from the medium with a wave vector $\boldsymbol{k}_f$. At this stage, the derivation of the autocorrelation function is reduced to that of the path-length distribution function $P(s,\boldsymbol{k}_i,\boldsymbol{k}_f)$ given by Eq. (3.2).

The fraction of the photons backscattered multiply from the medium is given by

$$I(\boldsymbol{k}_i,\boldsymbol{k}_f,s)=\int\int_0^\infty P(\boldsymbol{r},\boldsymbol{r}',t)\left[1+\cos(\boldsymbol{k}_i+\boldsymbol{k}_f)\cdot(\boldsymbol{r}-\boldsymbol{r}')\right]d\boldsymbol{r}_{\parallel}, \tag{3.3}$$

where $\boldsymbol{r}'$ and $\boldsymbol{r}$ denote the position vectors where the photon is incident to and leaves from the medium, respectively, and $\boldsymbol{r}_{\parallel}=\boldsymbol{r}-\boldsymbol{r}'$ is the projection of their difference to the boundary plane. In addition, t is the time for the photon to propagate from the incidence to the exit and, therefore, $s=ct$ is the path-length, c being the velocity of light in the medium. In the integrand of Eq. (3.3), the cosine term indicates the effect of constructive interference between the scattered wave and its time-reversed counterpart and the first term 1 comes from the contribution of incoherent components propagating along the different paths. $P(\boldsymbol{r},\boldsymbol{r}',t)$ denotes a Green function at the location $\boldsymbol{r}$ at a time t when a unit pulse is incident to the medium at a location $\boldsymbol{r}'$ at a time $t=0$. Since the propagation of light in the medium is approximated by a diffusion process, $P(\boldsymbol{r},\boldsymbol{r}',t)$ is given as a solution of the time-dependent diffusion equation:

$$\left(D\nabla_r^2+\frac{\partial}{\partial t}\right)P(\boldsymbol{r},\boldsymbol{r}',t)=\delta(\boldsymbol{r}-\boldsymbol{r}')\delta(t), \tag{3.4}$$

where $D = \ell^* c / 3$. It is actually obtained by the method of images as

$$P(\boldsymbol{r},\boldsymbol{r}',t) = P(\boldsymbol{r},\boldsymbol{r}',s)$$
$$= \left(\frac{3}{4\pi s\ell^*}\right)^{\frac{3}{2}} \left\{1 - \exp\left[-\frac{3(z_0 + C)^2}{s\ell^*}\right]\right\} \exp\left(-\frac{3r_{\|}^2}{4s\ell^*}\right) \tag{3.5}$$

In Eq. (3.5), z_0 is the distance along the z axis from the boundary plane to the virtual diffusive light source placed inside the medium and C is called an extrapolation length which is defined by the boundary condition at $z = 0$ and is given by

$$C = \frac{2\ell^*(1+R)}{3(1-R)}, \tag{3.6}$$

R being the reflection coefficient at the boundary surface.

By substituting Eq. (3.2) into Eq. (3.1) together with Eqs. (3.3) and (3.5) and by considering the limits of the small delayed time and the small backscattering angle, the normalized autocorrelation function of multiply-backscattered light fluctuations is obtained on the amplitude basis by

$$\gamma(\tau,\theta) = \frac{\Gamma_A(\tau,\theta)}{\Gamma_A(0,\theta)} \approx \frac{\exp\left(-A\sqrt{6\tau/\tau_0}\right) + \exp\left[-A\sqrt{6\tau/\tau_0 + \left(k\ell^*\theta\right)^2}\right]}{1 + \exp\left[-Ak\ell^*\theta\right]}, \tag{3.7}$$

where θ denotes the backscattering angle between the incident and exit wave vectors of $-\boldsymbol{k}_i$ and $\boldsymbol{k}_f$, and $A = (z_0 + C)/\ell^*$. Since the relaxation time is an important parameter in studying the temporal properties of random waves scattered from the disordered medium, the relaxation time of Eq. (3.7) is defined by

$$\tau_r(\theta) = \int_0^\infty \gamma(\tau,\theta)d\tau = \frac{\tau_0}{3A^2} \cdot \frac{1 + \left(1 + k\ell^* A\theta\right)\exp\left(-k\ell^* A\theta\right)}{1 + \exp\left(-k\ell^* A\theta\right)}, \tag{3.8}$$

where $|\boldsymbol{k}_i| = |\boldsymbol{k}_f| = k$ has been assumed in the above derivation.

It may be worthwhile to make clear the relation between the normalized autocorrelation functions given by Eq. (3.7) and obtained in the past work. In the limit of $\theta \to \infty$ and in the direction of retroreflection $\theta = 0$, Eq. (3.7) is reduced to the normalized autocorrelation function:

$$\gamma(\tau) = \exp\left(-A\sqrt{6\tau/\tau_0}\right). \tag{3.9}$$

which was derived without considering the interference effect [75]. Especially, it should be pointed out that, regardless of whether the theoretical derivation includes the coherent interference effect or not, the normalized autocorrelation function in the direction of retroreflection coincides exactly with that obtained in the past work.

3.3 Experimental setup

Figure 3.1 shows an experimental setup by which the intensity distribution and the normalized autocorrelation function of time-varying intensity fluctuations of light backscattered multiply from a dense disordered medium are measured. The linearly-polarized light emitted from a He-Ne laser with the wavelength of 0.633μm illuminates an aqueous suspension of polystyrene latex beads. In the solution, the refractive indices of the water as a solvent and the latex bead as a solute are 1.33 and 1.59, respectively. As samples, the four solutions with the volume fraction of 10% were prepared with the particles of diameters a=0.09, 0.30, 0.46 and 0.60 μm listed in Table 3.1. In Table 3.1,

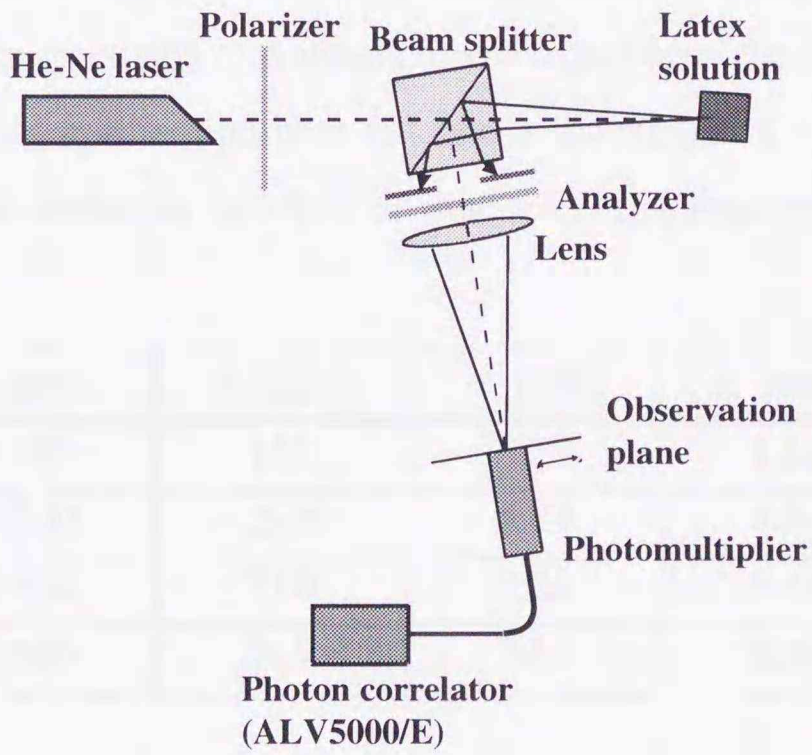

Fig. 3.1 Schematic diagram of the experimental setup for measuring the intensity distribution of the enhanced backscattering and the normalized autocorrelation function of time-varying intensity fluctuations of light scattered multiply from a dense disordered medium.

the transport mean free path-lengths ℓ^* calculated from the Mie theory, the elastic mean free path-lengths ℓ, and the order τ_0 of the relaxation time obtained from the homodyne amplitude autocorrelation function of the single scattering are presented. The sample is contained in a 10×10 mm^2 standard spectrometer glass cell. The thickness of the cell and the beam diameter of 3 mm are much larger than the elastic mean free path-length of the solution as shown in Table 3.1. The backscattered light from the sample forms an angular intensity distribution in the focal plane of a lens with the focal length of $f = 200$ mm. To pass only the light backscattered from the inside of the medium, a circular aperture placed in front of the lens blocks the lights reflected from the outer surface of the glass cell and the inner surface of the beam splitter by rotating slightly the glass cell and beam splitter around their centers.

The copolarized intensity is detected by a photomultiplier with the pinhole of 50 μm through an analyzer whose axis is parallel with that of a polarizer. The photomultiplier is set on a movable stage which is driven by a stepping motor with the accuracy of 0.1 μm in the observation plane. The angular accuracy in the observation plane is determined by the size of the pinhole attached to the photomultiplier because the diameter of the pinhole and the minimum stepped distance of the stage correspond to the angular accuracies of 0.25 mrad and 0.5 mrad, respectively. A photocurrent signal from the photomultiplier is firstly amplified by a pulse amplifier and next fed into a discriminator. Both the intensity and the normalized autocorrelation function of time-varying intensity fluctuations at a given

a [μm]	ℓ^* [μm]	ℓ [μm]	τ_0 [msec]
0.090	133	125	1.21
0.300	25.8	8.94	4.02
0.460	23.0	4.80	6.16
0.600	24.9	3.60	8.04

Table 3.1 Transport mean free path-lengths ℓ^* calculated from the Mie scattering theory, the elastic mean free path-lengths ℓ, and the order τ_0 of the relaxation time obtained from the homodyne amplitude autocorrelation function of the single scattering the for four different particles of diameters $a = 0.09$, 0.30, 0.46 and 0.60 μm.

position of the observation plane are simultaneously measured by a photon correlator (ALV5000/E) under control of a microcomputer. By changing the illuminating position over the sample and by repeating the measurements, fifteen intensity distributions and autocorrelation functions are measured from which the ensemble-averaged intensity distribution and the autocorrelation function are obtained. Finally, the normalized autocorrelation function of light fluctuations on the intensity basis is transformed to that on the amplitude basis by calculating numerically its square root under the assumption that the amplitude variation obeys the Gaussian statistics.

To confirm experimentally the analytical solution of the normalized autocorrelation function of multiply scattered light given by Eq. (3.7), we compare the relaxation times calculated from Eq. (3.8) with the experimental results. For estimating the relaxation time from the experimental data, a sort of averaging operation is really required because of a very subtle variation in the angular dependence of the autocorrelation function. Therefore, we examined two methods of the averaging operation. One is an integration method in which the normalized autocorrelation function obtained experimentally is directly integrated with respect to the delayed time from zero to infinity. This method gives the true relaxation time if the autocorrelation function decreases steeply to zero. In experiments, however, the normalized autocorrelation function usually takes a long tail for a long range of the delayed time and, therefore, the time interval of the integration had to be selected for every autocorrelation function. The other is a fitting method in which the experimental data are approximated to a model function by means of a fitting algorithm based on the least squared method. Since an accuracy of estimations depends on the selection of the model function, we adopted the normalized autocorrelation function of Eq. (3.9) which is redefined as

$$\gamma(\tau) = \exp\left(-B\sqrt{\tau}\right) \tag{3.10}$$

by setting $B = A\sqrt{6/\tau_0}$. The integration of Eq. (3.10) from zero to infinity gives the relaxation time as $\tau_r = 2/B^2$. The autocorrelation function obtained experimentally was approximated to Eq. (3.10) by means of the Levenberg-Marquard method [109], thus the relaxation time being determined. This method gave a relatively good approximation without the influence of finite data on the autocorrelation function. As a result of

repeated comparisons between two methods, we finally adopted the latter fitting method in this study. The variations of the relaxation times obtained experimentally as a function of the backscattering angle were compared with the numerical results obtained from the analytical solution of Eq. (3.8), in which all the parameters were estimated theoretically from the Mie scattering theory.

3.4 Results and discussion

We investigate the dependence of the intensity enhancement and the normalized autocorrelation function on the backscattering angle by comparing the experimental results with the theoretical ones for 10% solutions with the particles of four different diameters listed in Table 3.1. As a common notation of the figures, the four different marks of ●, ○, ▲ and △ in experimental results and the four different curves of solid, broken, dotted and chain lines in theoretical results correspond to the four different particles of diameters, 0.09, 0.30, 0.46 and 0.60 μm, respectively.

Fig. 3.2 (a) shows the normalized autocorrelation functions of backscattered light fluctuations on the amplitude basis which were experimentally and theoretically obtained at the backscattering angle of $\theta = 3.0$ mrad. The solid line denotes the autocorrelation functions which were approximated to the model function of Eq. (3.10) by using the nonlinear fitting based on the Levenberg-Marquard method. On the other hand, Fig. 3.2 (b) shows the theoretical autocorrelation functions which were calculated numerically from

$$\gamma(\tau,\theta) \approx \frac{\exp\left(-5\sqrt{6\tau/\tau_0}/3\right)+\exp\left[-5\sqrt{6\tau/\tau_0+\left(k\ell^*\theta\right)^2}/3\right]}{1+\exp\left[-5k\ell^*\theta/3\right]} \quad , \tag{3.11}$$

where the approximations of $z_0 \approx \ell^*$ and $C \approx 2\ell^*/3$ have been taken for the refractive indices of the water and the latex beads used in experiments. In Figs. 3.2 (a) and (b), the vertical and horizontal axes stand for the normalized autocorrelation function in a logarithmic scale and the square root of the delayed time, respectively.

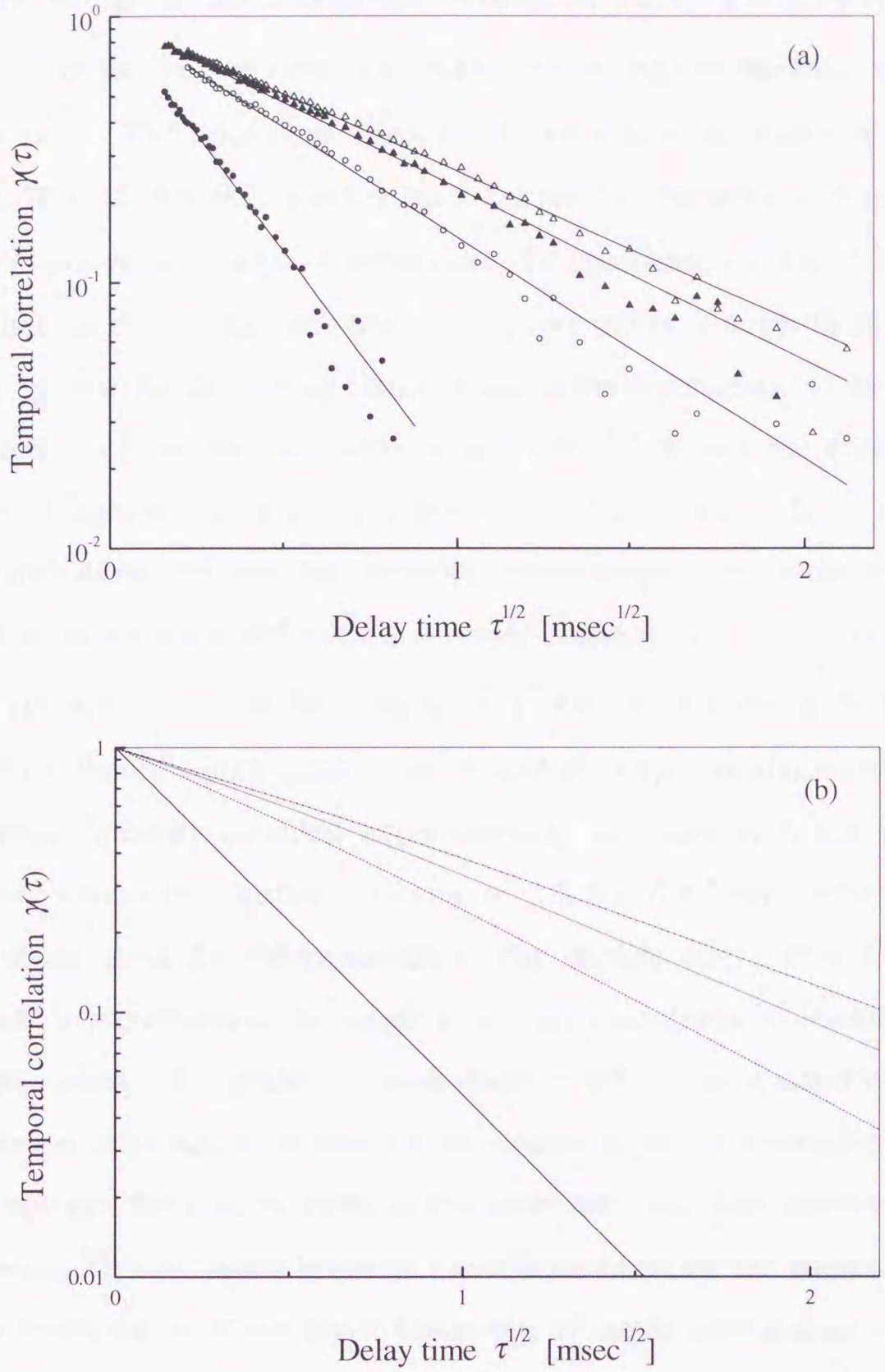

Fig. 3.2 Normalized autocorrelation functions of the multiply-scattered light fluctuations on the amplitude basis obtained in (a) the experiments using the experimental setup of Fig. 3.1 and (b) the theory calculated from Eq. (3.11). The vertical and horizontal axes stand for the correlation function in a logarithmic scale and the square root of the delayed time, respectively. The four different marks of ●, ○, ▲ and △ in the experimental results and the four different lines (solid, broken, dotted and chain lines) in the theoretical results correspond to the results obtained for the particles of diameters 0.09, 0.30, 0.46 and 0.60 μm, respectively.

As seen from the figures, the autocorrelation function decreases linearly with an increase in the square root of the delayed time $\sqrt{\tau}$ and its decreasing rate increases with a decrease of the particle size. The relaxation times of the experimental results were quantitatively estimated to be 0.15, 0.5, 0.75 and 0.9 msec for the four particles of diameters 0.09, 0.30, 0.46 and 0.60 μm, respectively. Furthermore, the comparison of Fig. 3.2 (a) with Fig. 3.2 (b) shows that the decreasing rate obtained in experiments is larger than that in the theory though they agree in the decreasing behavior and in the dependence on the particle size.

As a function of the backscattering angle, Fig. 3.3 shows the copolarized intensity distributions of light scattered multiply from dense disordered media. The backscattered intensity distributions indicate the intensity enhancement due to the interference effect between the scattered wave and its time-reversed counterpart. As shown in the figure, the peak width spreads roughly in the order of λ/ℓ^* with an increase of the particle size. In this respect, the theory agrees approximately with the experimental results. On the other hand, the peak intensity obtained experimentally increases with the particle size and approximately takes the constant intensity of 1.8 for the large particle size while the theoretical result takes 2.0 independently of the particle size. This discrepancy comes from the fact: in experiments, the single scattering contributes to forming the incoherent intensity component and degrades the peak intensity while it is assumed in the theory based on the diffusion approximation that all the scattered waves (including even the single scattering) possess the time-reversed counterpart and that they interferes constructively with each other. This influence becomes more remarkable for the particles of smaller size because the contribution of the single scattering increases with a decrease of the particle size [99].

Fig. 3.4 shows the relaxation times of the normalized autocorrelation functions for the copolarized backscattered light fluctuations on the amplitude basis as a function of the backscattering angle. In the temporal behavior of the multiply backscattered light under the interference effect between the scattered wave and its time-reversed counterpart, the relaxation time has one dip in the exact direction of retroreflection, increases up to two peaks at both sides of it, and decreases gradually from the peaks to the relaxation time of the incoherent light fluctuations with an increase of the backscattering angle.

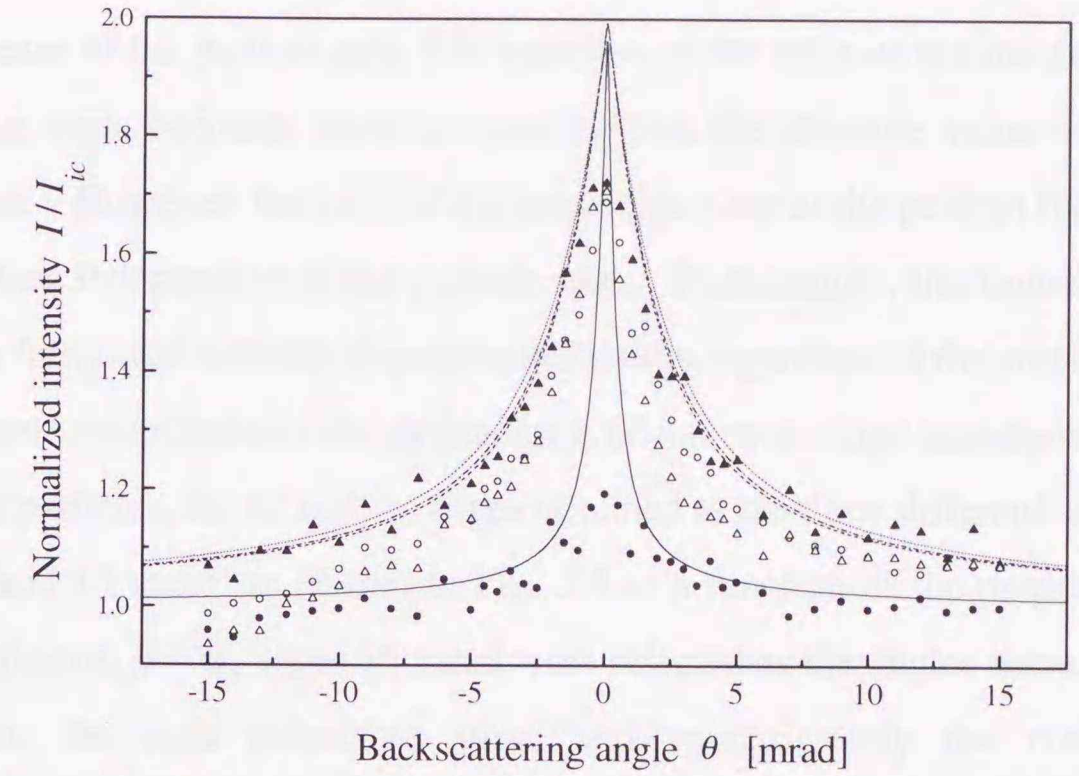

Fig. 3.3 Experimental and theoretical angular dependences of the intensity distributions produced by the enhanced backscatterings from 10% solutions of the latex beads. The vertical axis denotes the intensity normalized by the incoherent intensity component I_{ic}. The four different marks of ●, ○, ▲ and △ in the experimental results and the four different lines (solid, broken, dotted and chain lines) in the theoretical results correspond to the results obtained for the particles of diameters 0.09, 0.30, 0.46 and 0.60 μm, respectively.

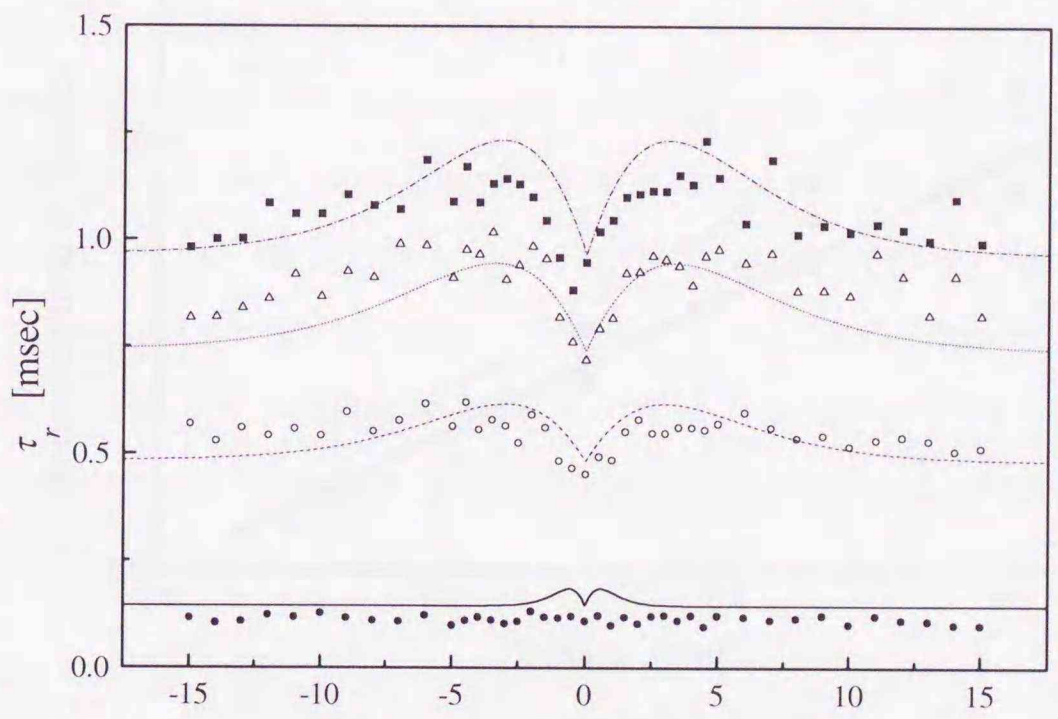

Fig. 3.4 Angular dependence of the relaxation time in the normalized autocorrelation functions under the influence of the constructive interference between the scattered wave and its time-reversed counterpart. The four different marks of ●, ○, ▲ and △ in the experimental results and the four different lines (solid, broken, dotted and chain lines) in the theoretical results correspond to the results obtained for the particles of diameters 0.09, 0.30, 0.46 and 0.60 μm, respectively.

With an increase of the particle size, this variation of the relaxation time depending on the backscattering angle becomes more outstanding and the absolute value of the relaxation time increases. However, the ratio of the relaxation time at the peak to that at the bottom keeps a constant independent of the particle size. Furthermore, the figure shows that the theory agrees fairly well with the experimental results regardless of the small discrepancy.

To investigate quantitatively the dependence of the normalized autocorrelation function on the size of particles, the relaxation times obtained at the three different scattering angles of $\theta = 0$, 3 and 15 mrad are plotted in Fig. 3.5 as a function of the particle size. These scattering angles of $\theta = 0$, 3 and 15 mrad were selected as the angles corresponding to the retroreflection, the peak relaxation time, and approximately the case of $\theta \to \infty$, respectively. In the figure, the three different marks of ■, ● and ○ obtained experimentally and the three different lines (solid, broken and dotted lines) calculated from Eq. (3.11) correspond to the results obtained at the three different scattering angles of

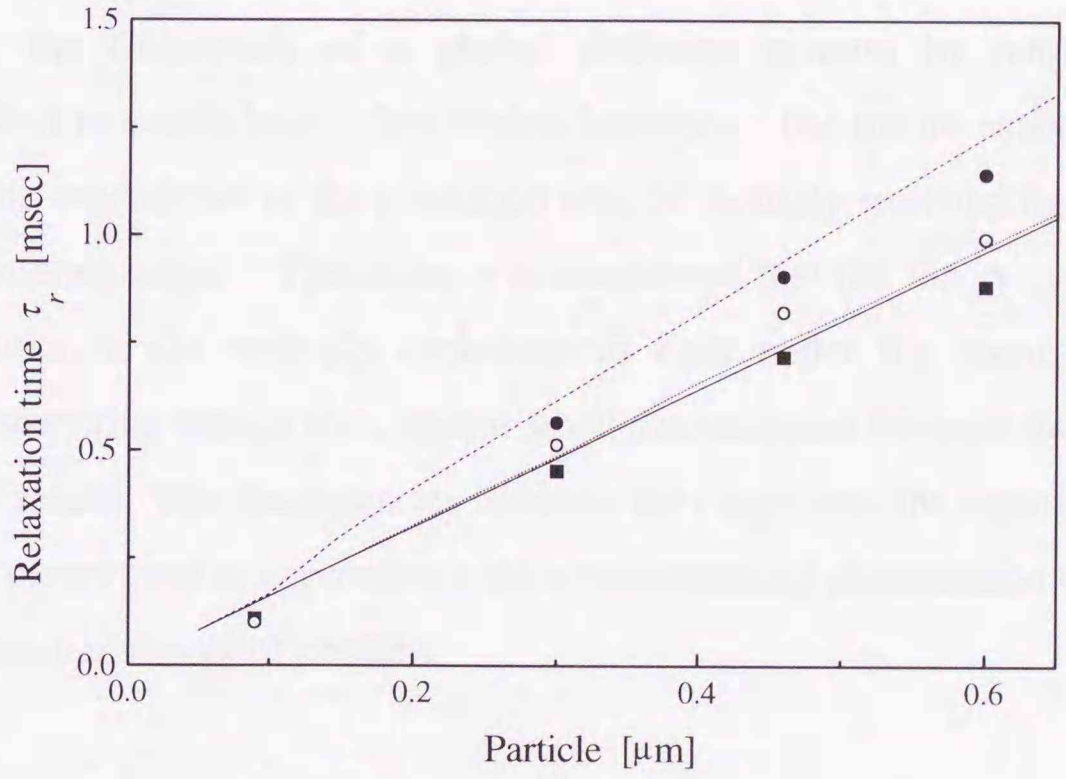

Fig. 3.5 Relaxation times of the normalized autocorrelation functions obtained at the scattering angles of $\theta = 0$, 3 and 15 mrad as a function of the particle diameter. The three different marks of ■, ○ and ● in the experimental results and the three different lines (solid, dotted and broken lines) in the theoretical results correspond to the results obtained for the backscattering angles of 0, 15 and 3 mrad, respectively.

$\theta = 0$, 3 and 5 mrad, respectively. As shown in Fig. 3.5, the relaxation time of the autocorrelation function increases in direct proportion to the particle diameter. The autocorrelation functions at $\theta = 0$ and 15 mrad are reduced to Eq. (3.9) and take the minimum relaxation time though the small discrepancy exists between the data obtained for $\theta = 0$ and 15 mrad. On the other hand, the relaxation times take a maximum approximately at $\theta = 3$ mrad for all particle sizes and the peak time increases linearly with the particle size.

3.5 Conclusions

This chapter has been concerned with the temporal correlation behavior of time-varying light fluctuations of light backscattered multiply from a dense disordered medium. The investigations were conducted with relation to the spatial properties of the backscattering enhancement produced from the interference effect between the scattered wave and its time-reversed counterpart. The temporal autocorrelation function was theoretically derived under the framework of a photon diffusion process by renormalizing the interference effect to a path-length distribution function. The theory enabled us to study the characteristic dependence of the relaxation time of multiply-scattered light fluctuations on the backscattering angle. Therefore, it is considered that the theory can describe the temporal behavior of the multiply backscattered light under the phenomenon of the enhanced backscattering though there appear small discrepancies between the experimental and theoretical results. The discrepancies between the theory and the experiments may be inherent in the theory used to approximate the wave scattering phenomenon on the basis of the diffusive transport theory of photons.

Chapter 4

Angular Polarization Properties of Spatio-Temporal Properties

4.1 Introduction

Temporal statistics of the time-varying light intensity scattered multiply from a disordered dense medium have been an interesting research subject in metrology using the dynamic light scattering. The studies on the temporal features of the dynamic multiply scattered light have been conducted under the framework of a diffusion approximation and developed to Diffuse Wave Spectroscopy (DWS) [73-75,101].

As another side view for the properties of the multiply scattered light, the coherent backscattering of light gives rise to an intensity enhancement [93,96-100,102,103], which results from a constructive interference between the scattered lights propagating along the time-forward and -reversed paths. It can be expected that the coherent backscattering affects its temporal feature depending on the polarization and the particle size. Qu and Dainty [76] experimentally showed different angular dependences of the relaxation time for the copolarized and cross-polarized intensities of the multiply backscattered light. Iwai and Dainty [77] experimentally connected an angular behavior of the relaxation time for the copolarized intensity with that of the path-length distribution function. Ishii et al. [104] investigated theoretically and experimentally such influences on the temporal autocorrelation function of the multiply backscattered light by means of the diffusive transport theory of photons.

In this chapter, we investigate the dependence of angular polarization features of the temporal autocorrelation function of the multiply backscattered light on the size of particles smaller than the wavelength of light. An approximation to the diffusive transport theory of photons breaks down because the low-order scattering is dominant for such a particle size. In addition, the polarization properties of the angular natures of the relaxation time

result from the coherent interference between the waves along the time-forward and -reversed paths. Therefore, we investigate wave-optically temporal autocorrelation functions of the multiply backscattered light by means of the Monte-Carlo simulations based on the Rayleigh-Debye scattering theory, which enables us to discuss the dependence of temporal properties not only on the polarization but also on the size of scattering particles. As a result, we demonstrate numerically and experimentally the angular dependence of the temporal autocorrelation functions of copolarized and cross-polarized components of the multiply backscattered light. Furthermore, the angular polarization behaviors of the time-varying light backscattered multiply from the dense random medium are interpreted clearly by revealing the contributions of the coherent components to the copolarized and cross-polarized intensity variations depending on the scattering angle, the scattering order, and the particle size. The quantitative comparisons between the simulated and the experimental results give a measure of the validity on the present simulation algorithm to simulate the phenomena of the time-varying coherent backscattering enhancement of light.

4.2 Numerical simulations

The simulations are based on the practical experiments shown in Fig. 4.1. The linearly-polarized laser light enters a disordered dense medium, undergoes successive scattering events by many particles, leaves from the medium in the backward direction, and forms an intensity pattern in the far field. Due to the Brownian motion of particles, an intensity varies in time and is detected by changing the detecting position in the direction parallel with the incident polarization of light. The copolarized and cross-polarized intensity variations of the light are observed through an analyzer which is set to be parallel with and normal to the direction of the incident polarization, respectively.

The temporal properties of the time-varying light scattered multiply in the direction of the backscattering angle θ from the disordered medium are described by a temporal autocorrelation function in a statistical sense. With the assumption that the displacements of all particles produced by Brownian motions obey the zero-mean Gaussian statistics, an

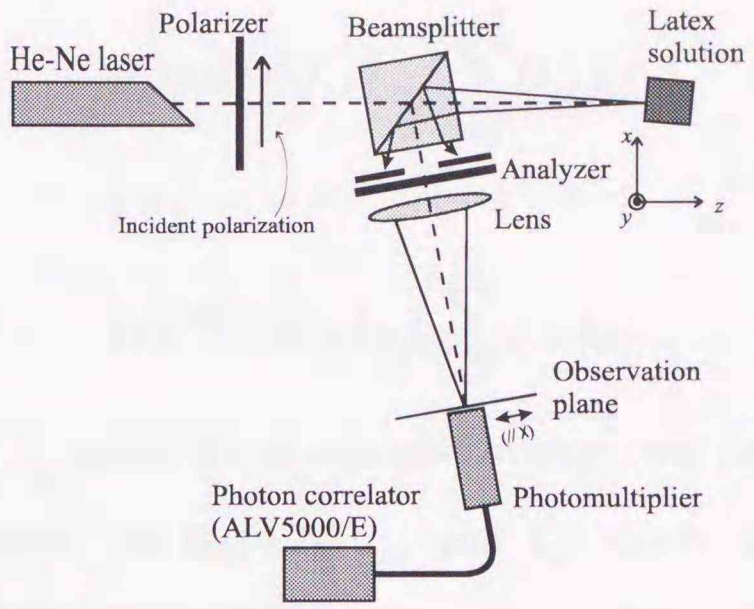

Fig. 4.1 Experimental setup assumed for the Monte Carlo simulations and used for practical measurements of the normalized autocorrelation function of the time-varying intensity variation backscattered multiply from disordered dense media. In experiments, 10 vol% aqueous suspensions of the polystyrene latex beads were used as disordered media. The photomultiplier is set on a movable stage which is driven by a stepping motor. The normalized autocorrelation function on the intensity basis obtained in experiments is transformed to that on the amplitude basis by calculating numerically its square root under the assumption that the amplitude variation obeys Gaussian statistics.

ensemble average with respect to the displacements yields a normalized autocorrelation function as

$$\gamma(\tau,\theta)=\sum_{n=1}^{\infty}p(n,\theta)\left\langle \exp\left(-\frac{4\tau}{\tau_0}\sum_{m=1}^{n}\sin^2\frac{\theta_m}{2}\right)\right\rangle_{\theta_m}, \tag{4.1}$$

where θ_m is the scattering angle at the m-th scattering event and $\langle\cdots\rangle_{\theta_m}$ means an ensemble average over the distribution of the scattering angle. $\tau_0=\left(Dk_i^2\right)^{-1}$ is an order of the single scattering relaxation time in a homodyne autocorrelation function, D and k_i standing for a diffusion coefficient of the particles and a wave number of the incident light, respectively. In addition, $p(n,\theta)$ denotes a fraction of the total intensity left in the direction of the backscattering angle θ after a sequence of n scattering events. By taking the depolarization effect into consideration, $p_X(n,\theta)$ and $p_Y(n,\theta)$ for the copolarized and cross-polarized components are defined by

$$p_X(n,\theta) = \langle I_{nX} \rangle_{ex} \Big/ \sum_{n=1}^{\infty} \langle I_{nX} \rangle_{ex} \tag{4.2a}$$

and

$$p_Y(n,\theta) = \langle I_{nY} \rangle_{ex} \Big/ \sum_{n=2}^{\infty} \langle I_{nY} \rangle_{ex}, \tag{4.2b}$$

respectively, where $\langle \cdots \rangle_{ex}$ stands for an ensemble average over the distribution of the exit position from the medium. In Eq.(4.2), I_{nX} and I_{nY} denote the n-th scattering order intensity components in the copolarized and cross-polarized intensity variations detected by scanning in the direction parallel to the incident polarization and are given by

$$I_{nX} = \begin{cases} p(1) \Big/ \left[p(1) + 2\sum_{n=2}^{\infty} p(n) F_{nX} \right] & n = 1 \\ 2p(n)F_{nX}(1+\cos\Phi_n) \Big/ \left[p(1) + 2\sum_{n=2}^{\infty} p(n) F_{nX} \right] & n \neq 1 \end{cases} \tag{4.3a}$$

and

$$I_{nY} = p(n)F_{nY}(1+\Gamma_n \cos\Phi_n) \Big/ \sum_{n=2}^{\infty} p(n)F_{nY} \qquad n \neq 1, \tag{4.3b}$$

respectively. In the equations, the subscripts X and Y stand for the directions of the axes of the analyzer and correspond to the detections of copolarized and cross-polarized intensities, respectively. $p(n)$ and $\Phi_{nX} = k\theta_n(X_n - X_1)$ denote a fraction of the total intensity left in the backward direction after a sequence of n scattering events and a phase difference at the exit position of $X = X_n$ along the X axis, respectively. Γ_n denotes the correlation between the waves depolarized from the X polarization to the Y polarization and vice versa. F_{nX} and F_{nY} are the ratios of the copolarized and cross-polarized components to the total of the scattered intensity components with the n-th scattering order.

In the simulations, 10^6 scattering angles θ_n and intensities, I_{nX} and I_{nY}, for a given scattering order n were obtained, from which the ensemble-averaged $\left\langle \exp\left(-4\tau/\tau_0 \sum_{m=1}^{n} \sin^2 \theta_m/2 \right) \right\rangle_{\theta_m}$ and the copolarized and cross-polarized intensity variations, $\langle I_{nX} \rangle_{ex}$ and $\langle I_{nY} \rangle_{ex}$, were obtained. By substituting $\langle I_{nX} \rangle_{ex}$ and $\langle I_{nY} \rangle_{ex}$ to

Eq. (4.1) together with Eq. (4.2), the normalized autocorrelation functions are finally evaluated for the copolarized and cross-polarized components of the time-varying light amplitude backscattered multiply from the disordered dense medium. It should finally be noted that the autocorrelation function given by Eq. (4.1) contains exactly the waves with the low scattering order from the single scattering. This is an important advantage of using the Monte Carlo simulations to analyze the dependence of the multiple light scattering phenomena on the size of particles smaller than the wavelength of light.

4.3 Results and discussion

Figures 4.2 and 4.3 show the normalized autocorrelation functions of the copolarized and cross-polarized backscattered lights on the amplitude basis obtained at the backscattering angle of $\theta = 3$ mrad. The simulations were conducted for the particles with seven different diameters listed in Table 4.1, in which the corresponding mean free path-length ℓ and an order of the single scattering relaxation time τ_0 are shown. In the experimental results, the solid lines were obtained by the nonlinear fitting [109] of experimental data to the normalized autocorrelation function of

$$\gamma(\tau) = \exp\left(-A\sqrt{\tau}\right) \tag{4.4}$$

which was derived under a diffusion approximation [75].

Particle diameter [nm]	ℓ [μm]	τ_0 [msec]
100	91.9	0.167
200	18.3	0.335
300	9.73	0.502
400	6.56	0.670
460	5.38	0.768
500	4.80	0.837
600	3.83	1.004

Table 4.1 Mean free path-lengths ℓ and orders of the single scattering relaxation time τ_0 for 10 vol% aqueous suspensions of the polystyrene latex beads with seven different diameters of 100, 200, 300, 400, 460, 500 and 600 nm which were assumed in simulations.

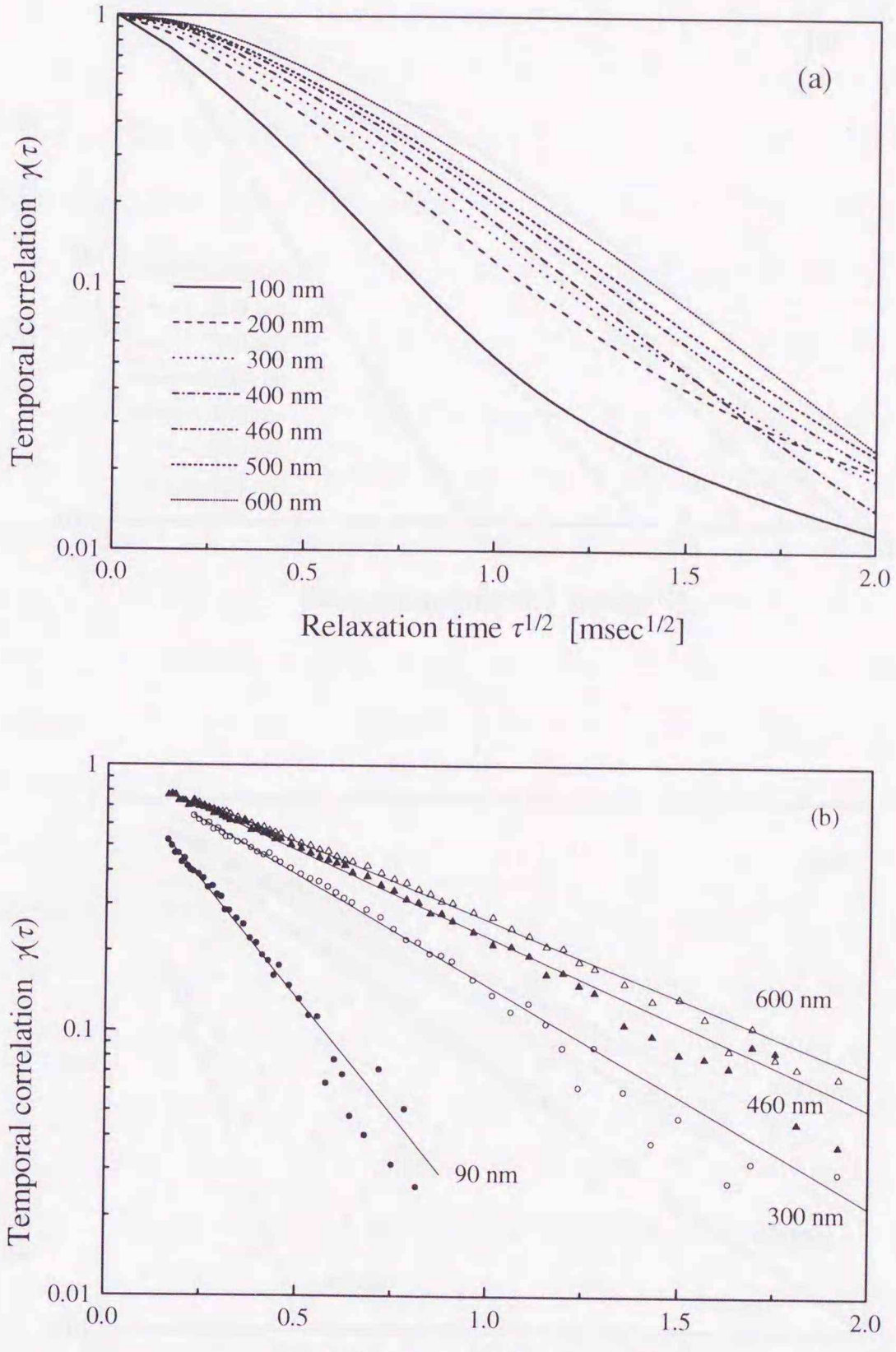

Fig. 4.2 Normalized temporal autocorrelation functions of the copolarized backscattering lights on the amplitude basis obtained at the backscattering angle of $\theta = 3$ mrad. (a) and (b) correspond to the results obtained in simulations and experiments, respectively. The vertical and horizontal axes stand for the normalized autocorrelation functions in a logarithmic scale, $\log[\gamma(\tau)]$, and the square root of the delayed time, $\sqrt{\tau}$, respectively.

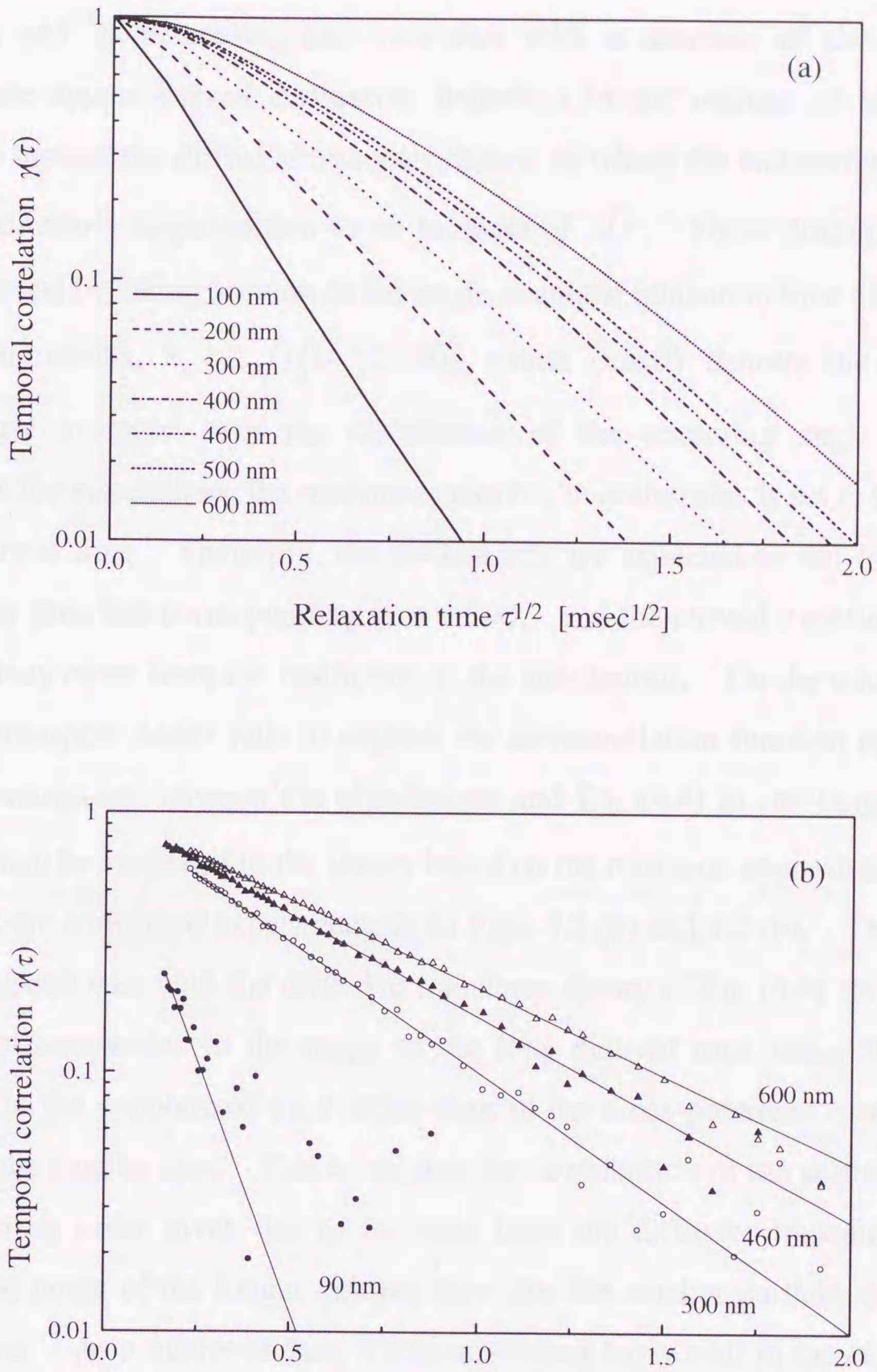

Fig. 4.3 Normalized temporal autocorrelation functions of the cross-polarized backscattering lights on the amplitude basis obtained at the backscattering angle of $\theta = 3$ mrad. (a) and (b) correspond to the results obtained in simulations and experiments, respectively. The vertical and horizontal axes stand for the normalized autocorrelation functions in a logarithmic scale, $\log[\gamma(\tau)]$, and the square root of the delayed time, $\sqrt{\tau}$, respectively.

The normalized autocorrelation function decreases monotonically with an increase of the delayed time and its decreasing rate increases with a decrease of the particle size. However, there appear curved decreasing behaviors in the regions of short and long delayed times against the diffusive transport theory, in which the autocorrelation function decreases rectilinearly in proportion to an increase of $\sqrt{\tau}$. These discrepancies can be clearly understood by taking account of the angle-averaged relaxation time after a sequence of n scattering events, $\tau_n \approx \tau_0 / n\left(1-\langle\cos\theta\rangle\right)$, where $\langle\cos\theta\rangle$ denotes the cosine of the scattering angle averaged over the distribution of the scattering angle for a single scattering. In the simulations, the maximum number of scatterings is set to be 300 to save the computational time. Therefore, the simulations are expected to fail for the delayed time τ shorter than that corresponding to $n = 300$, and the curved variation in the short delayed time may come from the restriction in the simulations. On the other hand, since the diffusive transport theory fails to express the autocorrelation function in the range of $\tau > \tau_0$, the discrepancy between the simulations and Eq. (4.4) in the range of the long delayed time may be attributed to the theory based on the diffusion approximation. These considerations are confirmed experimentally in Figs. 4.2 (b) and 4.3 (b). The comparison of the experimental data with the diffusive transform theory of Eq. (4.4) shows that there appear larger discrepancies in the range of the long delayed time rather than the short delayed time, in the copolarized case rather than in the cross-polarized case, and for the particles with the smaller size. This is because the contribution of the scattered light with the low scattering order gives rise to an error from the diffusive transport theory and increases in the range of the longer delayed time, for the smaller particle size and in the copolarized case. As a matter of fact, it was confirmed fairly well in the experiment that the temporal autocorrelation function decays in proportion to $-\sqrt{\tau}$ at the delayed time smaller than a few microsecond in agreement with the diffusive transport theory [105].

To compare quantitatively the angular polarization behaviors of the autocorrelation function of the multiply backscattered light, the relaxation time is defined by

$$\tau_r = \int_0^\infty \gamma(\tau) d\tau = 2/A^2 , \tag{4.5}$$

where Eq. (4.4) was used in the derivation. In the experiments, the relaxation time is estimated by substituting the parameter A obtained in the nonlinear fitting of experimental data to Eq. (4.4) while, in the simulations, it is obtained by integrating directly the obtained autocorrelation function following the definition of Eq. (4.5). Figs. 4.4 and 4.5 show the relaxation times of the normalized autocorrelation functions for the copolarized and cross-polarized components as a function of the backscattering angle, respectively. As seen from these figures, the angular dependence of the relaxation time for the copolarized light shows twin peaks at both sides of the direction of retroreflection but for the cross-polarized light a single peak in that direction. Such a temporal behavior was firstly observed by Qu and Dainty [76] and gave the phenomenological explanation on the basis that the longer path-length produces the shorter relaxation time. The figures also show that the angular dependence becomes more outstanding and a value of the relaxation time increases consistently with the larger particle size. As a result from the detailed numerical simulations, both the ratio of the relaxation time at the peak to that at the dip for the copolarized component and the ratio of the relaxation time at the peak to that at the large backscattering angle for the cross-polarized component take constant values for the large particle size, which agree with the results from the diffusive transport theory of photons [104]. By decreasing the size of particles, the ratio for the copolarized component decreases due to an increase in the contributions of the low-order scattered light. As a result, the dip and peak of the relaxation time disappear in experimental data. Furthermore, the width between the peaks for the copolarized component and the width of the peak for the cross-polarized component are inversely proportional to the transport mean free path-length.

The above space-time feature of the autocorrelation function is a peculiar property in the time-varying light backscattered multiply from the Brownian dynamics of the particles suspended in a disordered dense medium. Figs. 4.6 and 4.7 show the contributions of the coherent component in the copolarized and cross-polarized light variations for the particle sizes of 100 nm and 300 nm, respectively.

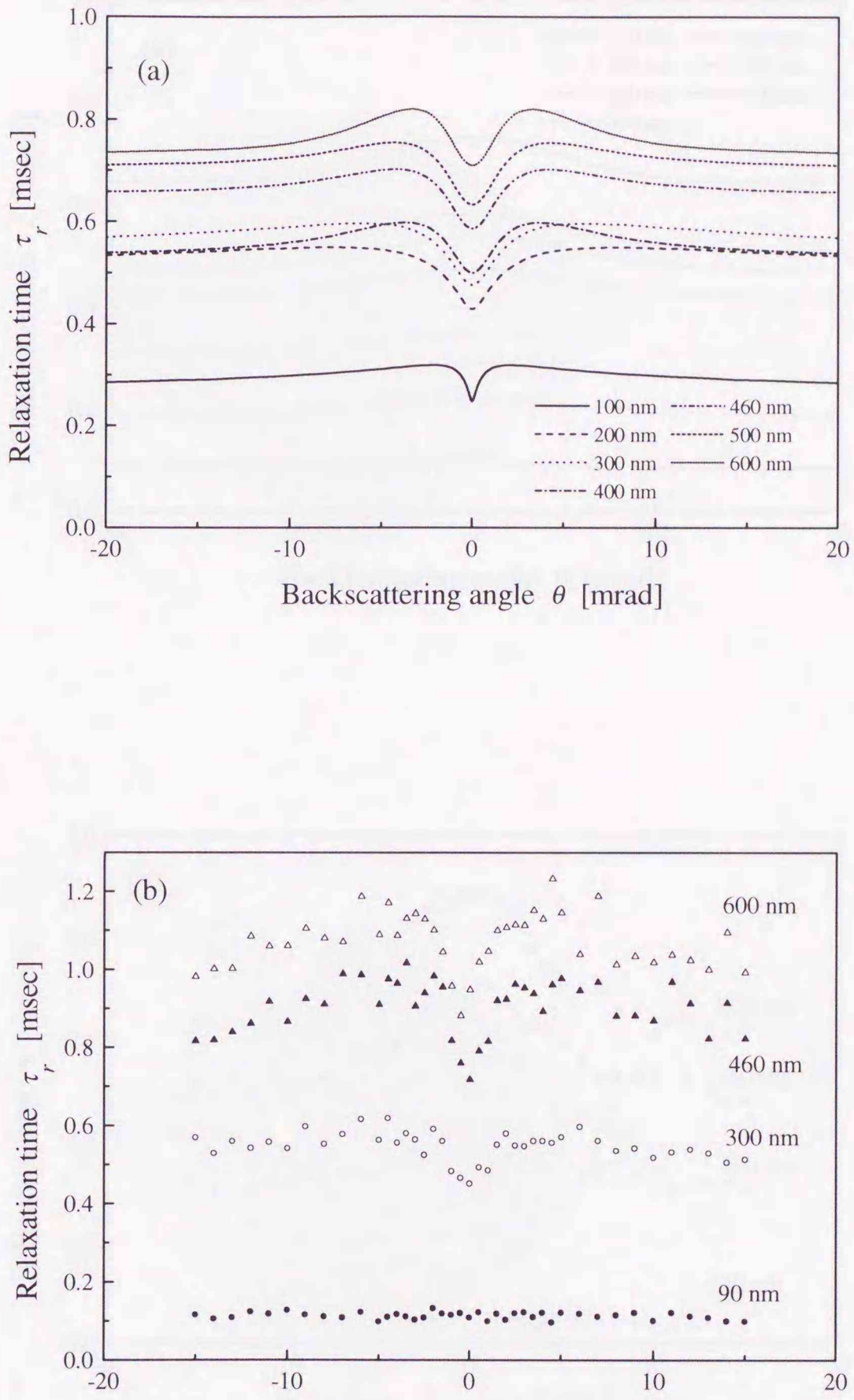

Fig. 4.4 Relaxation time of the normalized temporal autocorrelation function of the copolarized light on the amplitude basis as a function of the backscattering angle. (a) and (b) correspond to the results obtained in simulations and experiments, respectively.

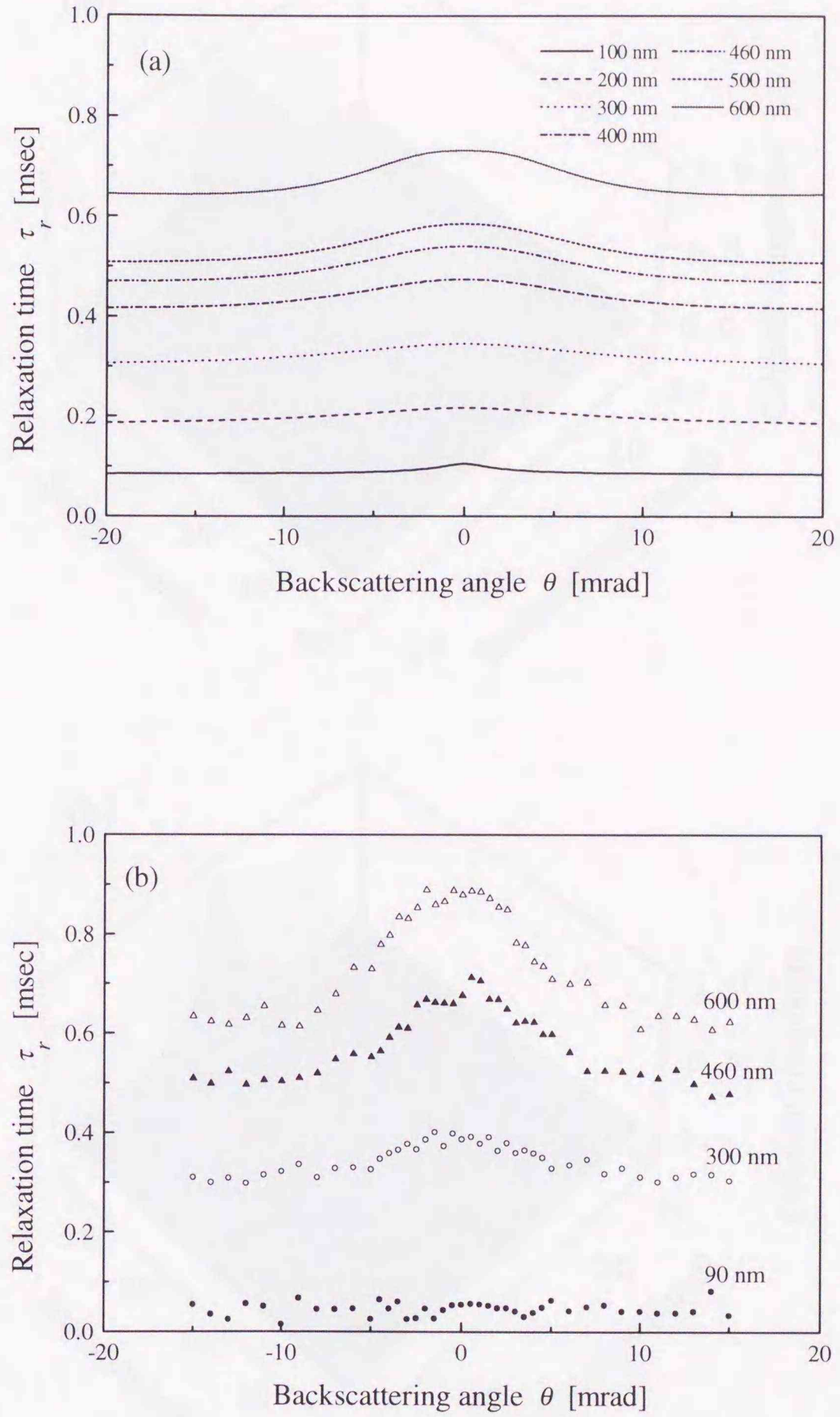

Fig. 4.5 Relaxation time of the normalized temporal autocorrelation function of the cross-polarized light on the amplitude basis as a function of the backscattering angle, respectively. (a) and (b) correspond to the results obtained in simulations and experiments, respectively.

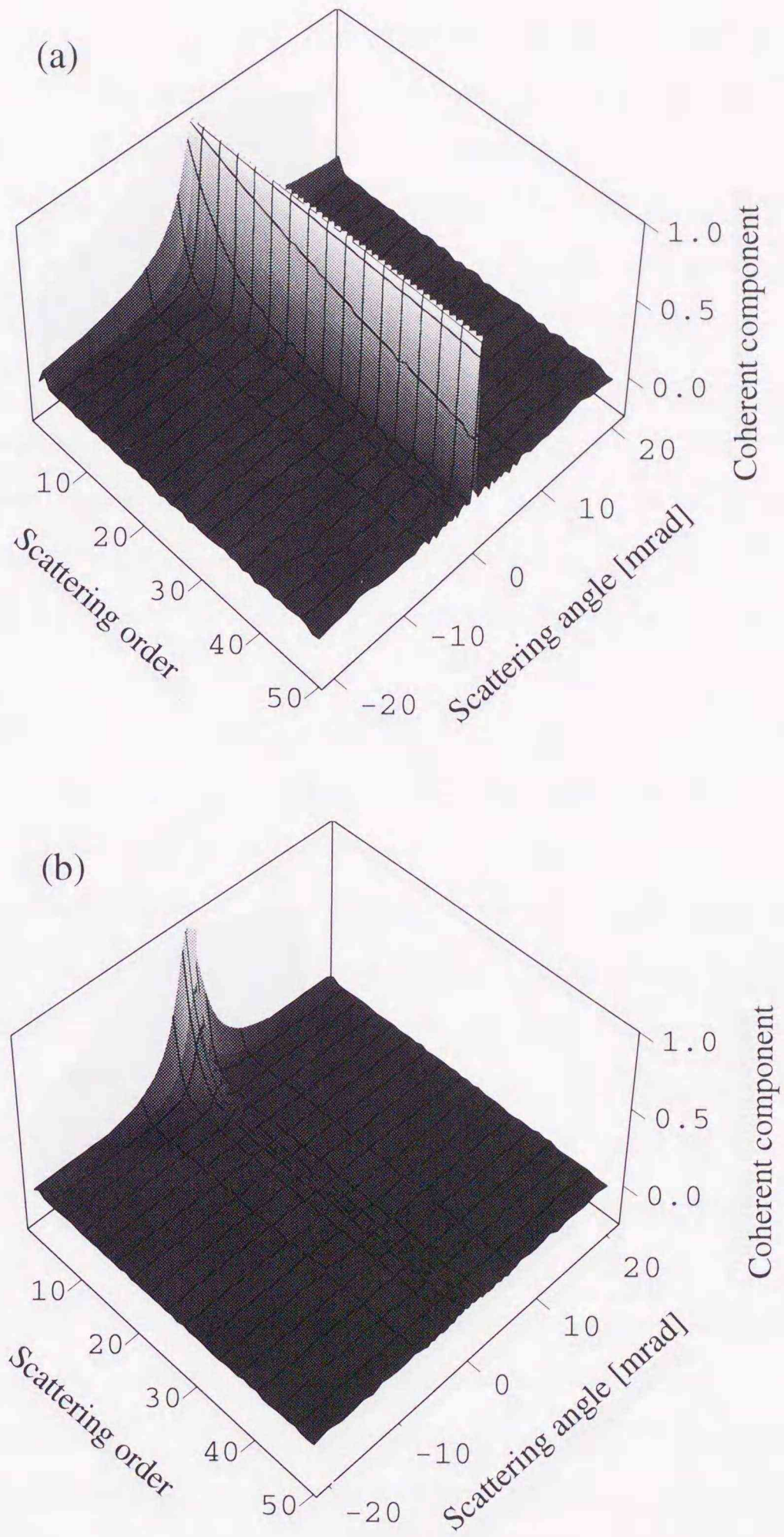

Fig. 4.6 Coherent components of the scattered light obtained for the particle diameter of 100 nm in simulations as a function of the backscattered angle and the scattered order. (a) and (b) correspond to the results for copolarized and cross-polarized intensity variations, respectively.

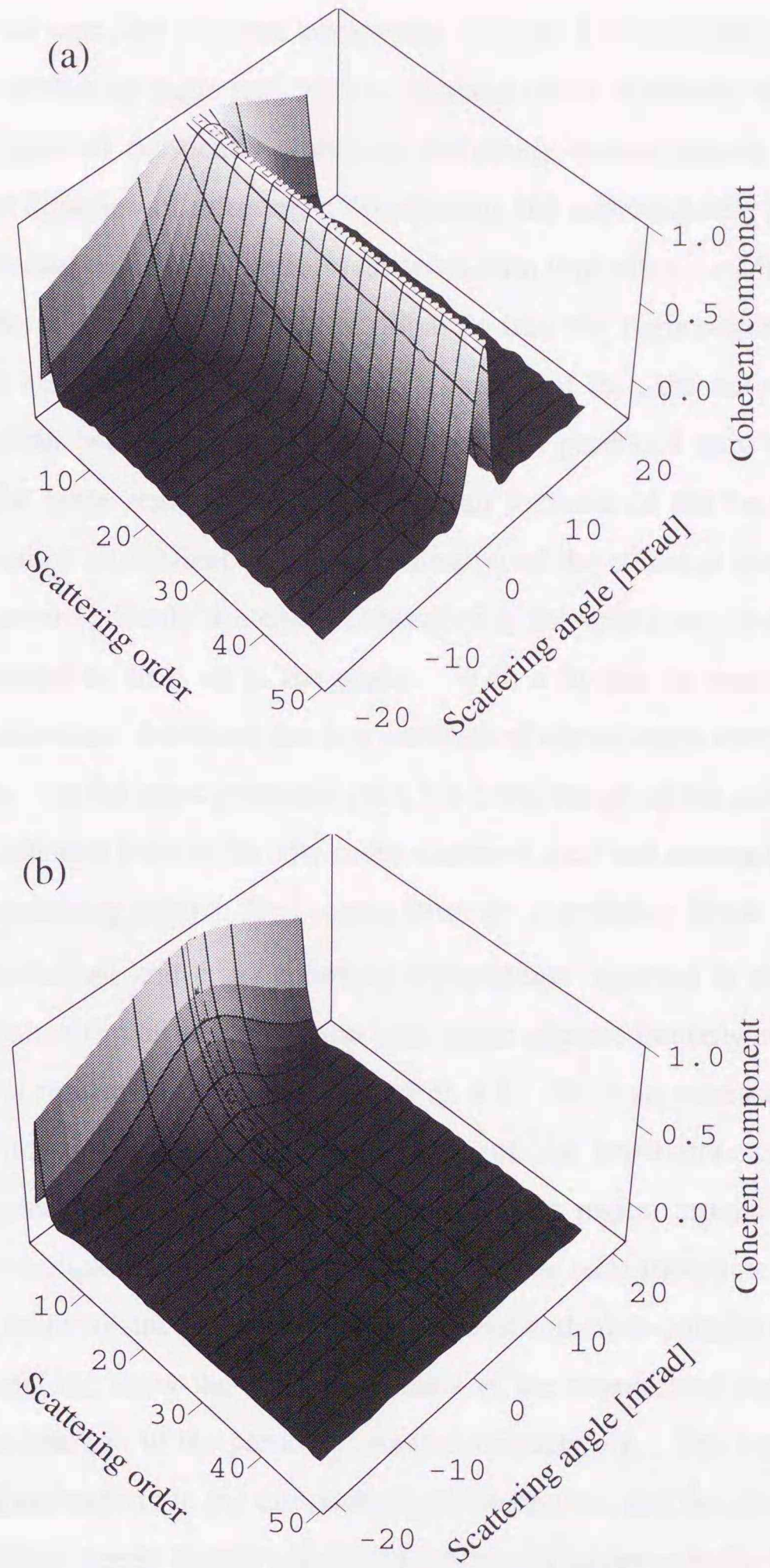

Fig. 4.7 Coherent components of the scattered light obtained for the particle diameter of 300 nm in simulations as a function of the backscattered angle and the scattered order. (a) and (b) correspond to the results for copolarized and cross-polarized intensity variations, respectively.

In the copolarized case, the coherent component with the low scattering order contributes widely over the scattering angle and, with an increase of the scattering order, the coherent component is localized drastically within an extremely narrow region of the scattering angle around the direction of retroreflection retaining the approximately perfect coherence over all the scattering orders. Therefore, the relaxation time takes a minimum in the exact direction of retroreflection, following the principle that the higher-order scattering light gives rise to the shorter relaxation time. As a matter of fact, the relaxation time at the exact retroreflection becomes slightly smaller than that produced only by the incoherent component at the large scattering angle. With an increase of the backscattering angle from the direction of retroreflection, the contribution of the coherent component with the high scattering order suddenly decreases, consequently the relaxation time increasing from the minimum relaxation time up to the peaks. With a further increase of the scattering angle, the relaxation time decreases due to a decrease of the coherent component in the low scattering orders. In the cross-polarized case, the contribution of the coherent component is not perfectly coherent even in the low-order scattered light and decreases greatly with an increase in the scattering order. This comes from the correlation factor Γ_n in Eq. (4.3b) between the copolarized and cross-polarized components occurred in the n-th scattering event. As a result, a dip of the correlation time never appears but only a peak is observed in the direction of retroreflection as shown in Fig. 4.5. With an increase of the particle size from 100 nm to 300 nm, the contribution of the low-order scattering coherent component decreases and is localized within a broader region around the direction of retroreflection, consequently the spatial dependence of the relaxation time on the scattering angle becoming more enhanced in both the copolarized and cross-polarized components.

Figs. 4.8 (a) and (b) show the relaxation times of the copolarized and cross-polarized components as a function of the particle diameter, respectively. The scattering angles of 0, 3 and 15 mrad correspond to the direction of retroreflection, and the directions where the relaxation time takes a peak for the copolarized light and where only the incoherent lights contribute to the intensity distribution. In the region of the large scattering angle, the relaxation time is proportional to the particle size via a diffusion constant because the temporal autocorrelation function of the time-varying scattered light coincides with that obtained theoretically from the diffusive transport of photons.

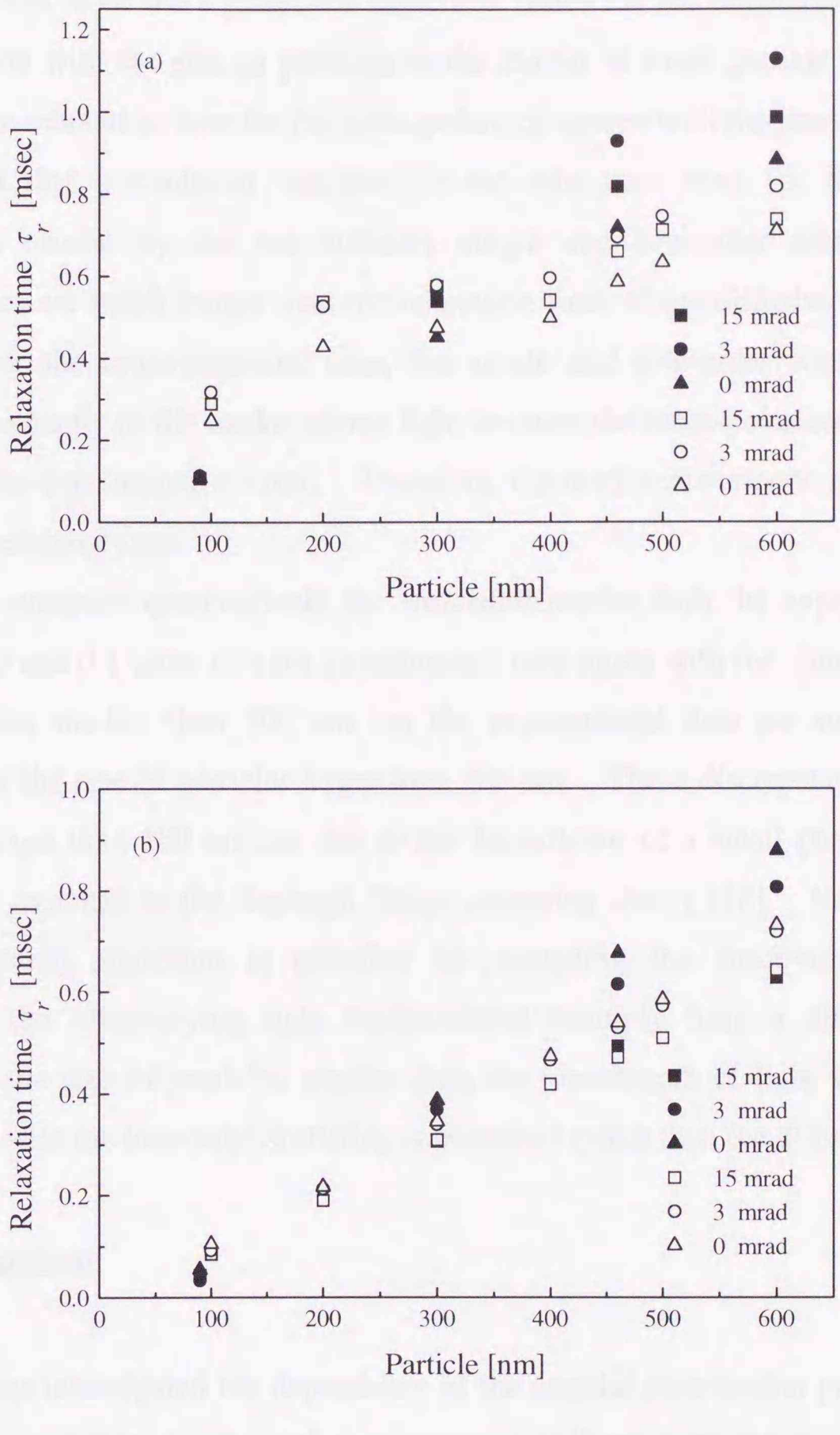

Fig. 4.8 Relaxation times of (a) copolarized and (b) cross-polarized lights as a function of the particle diameter. Three different marks of the square, the circle and the triangle correspond to the data obtained at three different scattering angles of $\theta = 0$, 3 and 15 mrad, respectively, in which the black and the white denote the results obtained in simulations and experiments, respectively.

However, as seen from the figures, the relaxation times for the copolarized case do not increase linearly with the size of particles in the region of small particle sizes though a variation of the relaxation time for the cross-polarized agrees with the prediction. It may be considered that a nonlinear variation of the relaxation time for the copolarized component is caused by the non-diffusive single and low-order scatterings whose relaxation times are much longer than the relaxation time of the diffusive light. On the other hand, for the cross-polarized case, the single and low-order scatterings do not contribute dominantly to the backscattered light because the cross-polarized component is generated by the depolarization [106]. Therefore, the nonlinear variation does not appear for the cross-polarized case.

Finally, we compare quantitatively the simulated results with the experimental ones. Figures 4.8 (a) and (b) show that the experimental data agree with the simulations for the size of particles smaller than 300 nm but the experimental data are smaller than the simulations for the size of particles larger than 300 nm. These discrepancies for the size of particles larger than 300 nm are due to the breakdown of a small phase shift of the scattered light assumed in the Rayleigh-Debye scattering theory [18]. Nevertheless, the present simulation algorithm is effective for analyzing the space-time polarization properties of the time-varying light backscattered multiply from a disordered dense medium with the size of particles smaller than the wavelength of light where the non-diffusive light with the low-order scattering is dominant rather than the diffusive one.

4.4 Conclusions

This chapter has investigated the dependence of the angular polarization properties of the temporal autocorrelation function of the time-varying light scattered multiply from the Brownian dynamics of scattering particles, on the size of particles smaller than the wavelength of light. Since the low-order scattering is dominant for such a particle size, an approximation in the diffusive transport theory of photons breaks down to express the phenomena of multiple backscatterings. Therefore, we have investigated temporal autocorrelation functions by means of the Monte-Carlo simulations based on the Rayleigh-Debye scattering theory. The simulations demonstrated successfully the polarization

properties of a variation in the relaxation time as a function of the scattering angle obtained experimentally by Qu and Dainty [76]. In addition, we demonstrated the dependence of the angular polarization properties of the relaxation time on the size of scattering particles by means of the simulations and confirmed experimentally the simulated results. Especially, the simulations revealed that the angular polarization behaviors can be clearly interpreted by displaying the dependence of the contribution of the coherent component to the copolarized and cross-polarized intensity variations depending on the scattering angle, the scattering order, and the particle size. Finally, the quantitative comparisons between the simulated and the experimental data gave a criterion in the validity of the present simulation algorithm based on the Rayleigh-Debye scattering theory with respect to the relation between the size of particles and the wavelength of light.

Chapter 5

Free Path-Length Distribution Function in Fractal Aggregates of Particles

5.1 Introduction

The light scattering techniques have been a powerful way of studying fractal structures of particle aggregates [33,100,110-115]. The dimension of a tenuous fractal medium with $1<D<3$ has been measured successfully by means of a small-angle-scattering method [33,110-112] and a second-order-scattering method [113]. For a dense fractal medium, a copolarized intensity peak of the enhanced-backscattering light was investigated experimentally because the light can hardly transmit through such a dense medium [114,115]. The theory of light scattering phenomena from the dense fractal medium has not yet been established though the theoretical analysis was conceptually given for a percolation system [100]. An experimental study for the dense fractal medium is usually quite difficult because the control of the fractal dimension requires much skill and experience. Therefore, the usefulness of Monte Carlo simulations increases in the study on the multiple scattering of light from the fractal aggregate of particles.

Monte Carlo simulations have been a powerful tool for analyzing phenomelogically and quantitatively the propagation properties of light scattered multiply from a dense random medium [99,103,116-118]. In simulations, the free path-length distribution function (FPDF) is a key function, which is a probability density function of the distance between the successive particles and specifies the spatial structure of a scattering medium. It is well known that the scattering particles are distributed negative-exponentially in the three-dimensional space of a homogeneously random medium and that an averaged distance is given by a mean free path-length ℓ.

In this chapter, we derive theoretically a FPDF of the fractal aggregate of particles and an effective mean free path-length ℓ_D is introduced as a measure of randomness from the analogy of the homogeneously random medium. The derived FPDF is examined

numerically by generating the particles distributed in the three dimensional space and estimating the dimension using the radius-gyration method. As an example of the application of the FPDF, the Monte Carlo simulations are conducted for a copolarized intensity peak of the light backscattered multiply from the fractal aggregates of particles to compare with the experimental result obtained by Dogariu et al [114]. The resultant intensity peak has an order of λ/ℓ_D in angular width and decreases in accordance with θ^{2-D} as a function of the scattering angle. These properties are corresponding to those of homogenous random media with D=3, which have an order of the angular width λ/ℓ and decrease in accordance with θ^{-1}. As a result, the validity and applicability of the model in the fractal structure and the derived FPDF are confirmed from the numerical results.

5.2 Properties of aggregates of particles

Colloidal particles are classified as lyophobic or lyophilic. Lyophobic particles have little affinity for the solvent and their stability is governed only by their charges, whereas lyphilic particles have a strong affinity for the solvent and the stability of these systems is governed by their charge and solvation properties. Thereby, lyophobic particles may aggregate by addition of a small amount of electrolyte though lyophilic scarcely aggregate. Examples of lyophobic colloids are dispersed paint and gold and sliver iodide sols. The colloidal suspension of polystyrene latex particles in deionized water, that we use in our experiments, also belongs to lyophobic colloids and the particles disperses stably in the suspension because of their high charge density. Fig. 5.1 (a) shows a picture of particles in the colloidal suspension, which was taken by an optical microscope after enough dilution by deionized water. However, the particles aggregates and generates clusters by addition of electrolyte, as shown in Fig. 5.1 (b).

The dispersion and aggregation of colloidal particles have quantitatively been explained in the Derjaguin-Landau-Verwey-Overbeek (DLVO) theory. According to the DLVO theory, Repulsion due to electric double layer and an attractive force due to London-van der Waals interaction are exerted between the particles in the colloidal suspension. The total potential energy $V(s)$ between two particles in colloidal suspension is obtained by the sum of the repulsive electric potential energy $V_R(s)$ and the London-van der Waals potential energy $V_A(s)$:

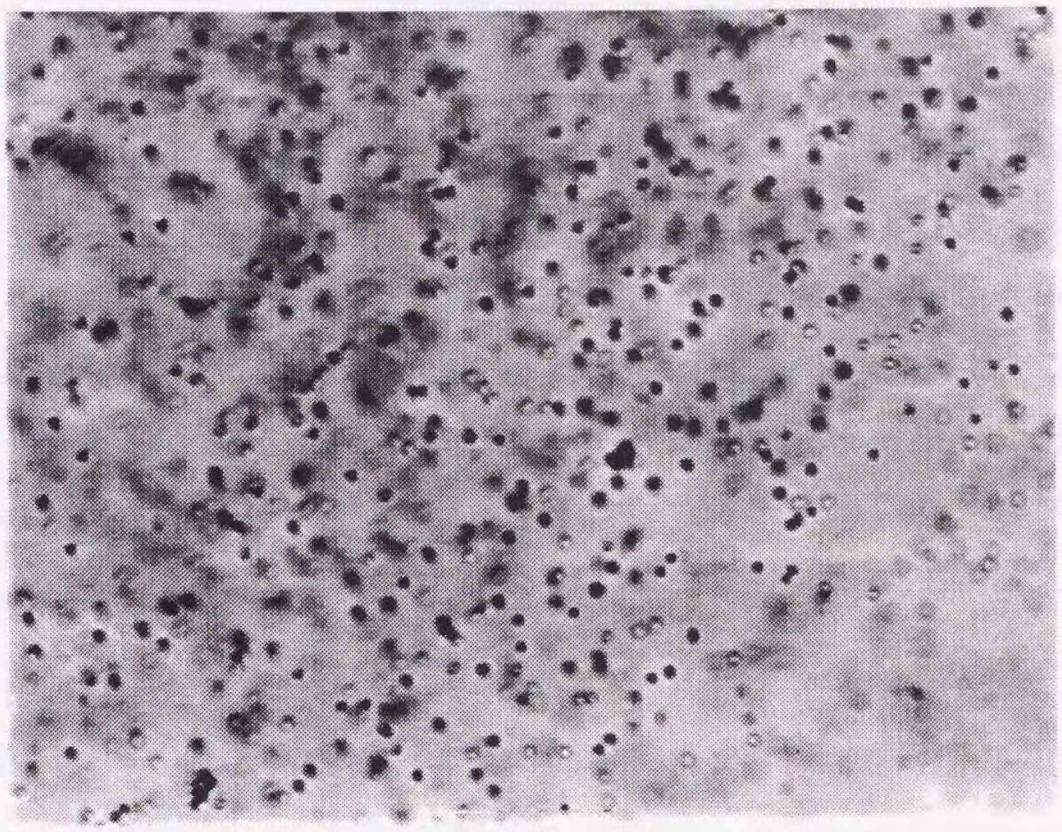

(a)

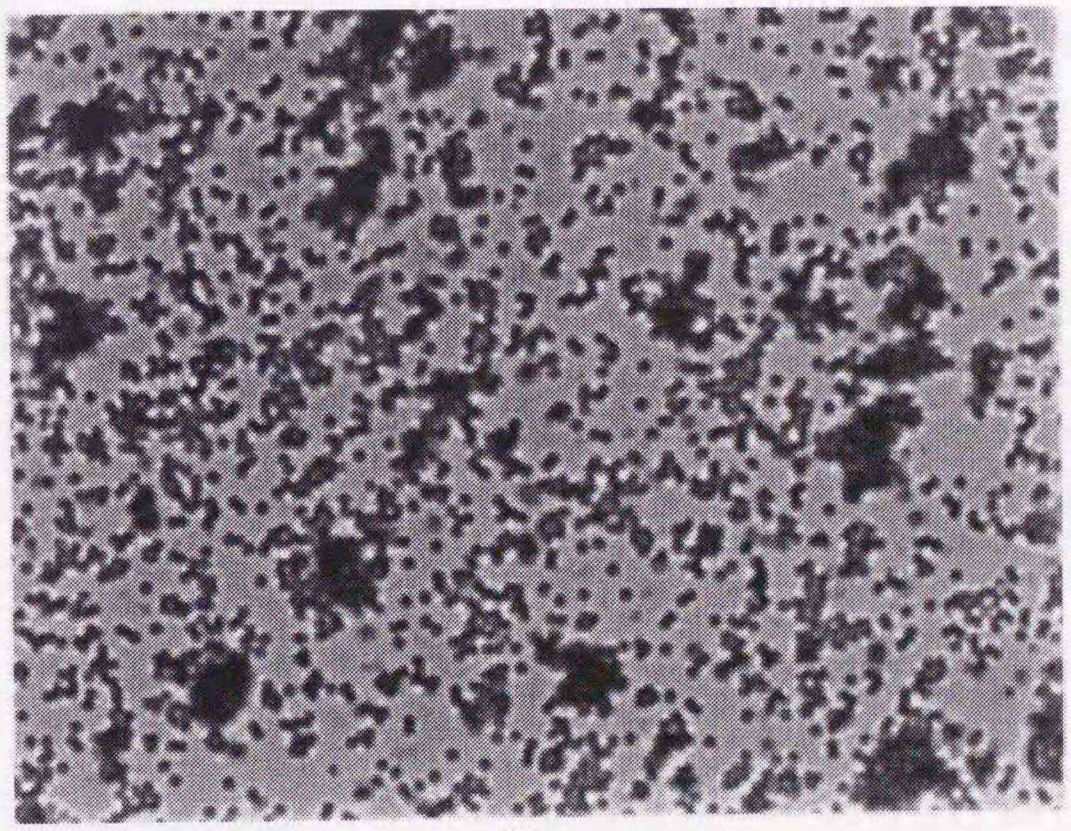

(b)

Fig. 5.1 Distributions of particles in the colloidal suspension (a) without and (b) with aggregation, which were taken by a CCD camera mounted on an optical microscope. Particles disperse homogeneously in 3D space and form clusters as shown in (a) and (b), respectively.

$$V(s)=V_R(s)+V_A(s), \tag{5.1}$$

where s stands for the separation distance between two particles.

First, let us consider the electric interaction between two particles in colloidal suspension. The particles generate electric double layer because the surface of a particle is charged with electricity and attracts counter ions around it. In this case, the electric potential of a particle is not expressed by the simple Coulomb interaction but by the Poisson-Boltzmann equation. The repulsion arises from an increase of concentration of counter ions between two particles as they approach to each other and is characterized by the Debye-Huckel screening length $1/\kappa$ defined as

$$\kappa^2=\frac{4\pi e^2}{\varepsilon k_B T}\sum n_i Z_i^2, \tag{5.2}$$

where ε is the dielectric constant of solvent, e is the elementary electric charge, k_B is the Boltzmann constant, T is the absolute temperature, and Z_i and n_i are charge and the number density of i-th species ions, respectively. For two identical sphere with radius $a >> 1/\kappa$ and Stern potential V_s, the potential energy V_R of electric repulsion is given by Debye-Huckel approximation as

$$V_R(s)=2\pi\varepsilon a V_s^2 \ln[1+\exp(-\kappa s)]. \tag{5.3}$$

The attractive force is caused by the fact that an instantaneous asymmetry in electron distribution in the valence shell in a molecule induces a synchronized asymmetry in electron distribution in a neighboring molecule and the free energy of them decreases. This interaction is referred to as London-van der Waals interaction and its potential energy is expressed as

$$V_A(s)=-\frac{A}{12}\left[\frac{4a^2}{s^2+4as}+\frac{4a^2}{s^2+4as+4a^2}+2\ln\left(\frac{s^2+4as}{s^2+4as+4a^2}\right)\right], \tag{5.4}$$

where A is the Hamaker constant.

Figure 5.2 shows the potential energy between two particles in colloidal suspension. As seen in Fig. 5.2, a potential barrier exists in the region $V_R > V_A$, by which particles disperses stably in the suspension. As the concentration of electrolysis in suspension increases, the repulsion decreases and, therefore, the potential barrier becomes lower. Particles aggregates and generates clusters when the potential barrier is lower than the

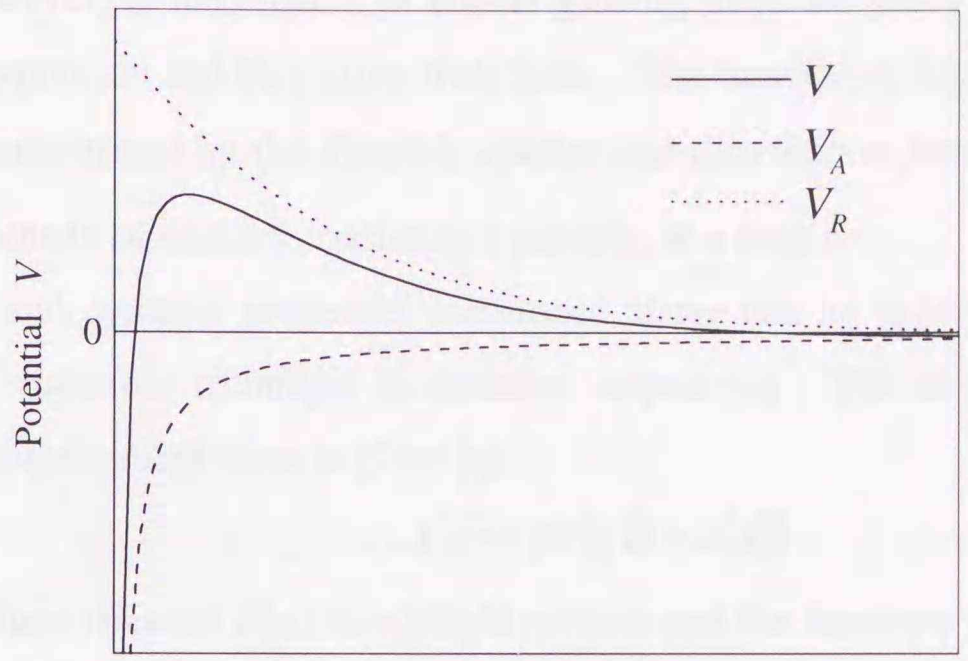

Fig. 5.2 Potential energy of a particle in colloidal suspension. The solid, broken, and dotted lines denote the total potential energy, repulsive potential energy due to the electric interaction, and attractive potential energy due to the London-van der Waals interaction.

thermal energy of a particle. For the case that the particles move due to Brownian motion and particles stick due to their collision, the aggregation process is referred as to *Diffision-limited aggregation* (DLA).

The statistical properties of structures of clusters are characterized by the *cluster dimension D*. The number of particles with radius a in a sphere with radius R in the 3-D space is given by

$$N(R) = \rho\left(\frac{R}{a}\right)^D , \tag{5.5}$$

where the density ρ stands for how the particles are packed. The cluster dimension presents only the number-radius relation and no information about the shape of the cluster, the density of suspension, and kinetics of particles. The cluster is called fractal cluster and the dimension is referred to as the *cluster fractal dimension* of *fractal diemsnion* when the cluster dimension is noninteger though it is always equal to or smaller than Euclidean dimension 3 of the space.

Fractal dimension provides information about the static and geometric properties of a cluster. However, in the process of cluster growth, there are many clusters with various size in the suspension and they grow with time. The time dependent properties of cluster growth is characterized by the *dynamic cluster-size distribution function* $n_s(t)$, which is the number density of clusters consisting s particles at a time t.

The static and dynamic properties mentioned above can be experimentally determined by the light scattering technique in tenuous suspension. The scattered intensity from particles in tenuous suspension is given by

$$I(q) = \rho P(q)[1 + S(q)] \tag{5.6}$$

in terms of phase function $P(q)$ of a single particle and the structure factor $S(q)$, where q and ρ is a magnitude of scattering vector and average number density in the system. The structure factor is the Fourier transform of the density-density correlation function $c(r)$ and expressed as

$$S(q) = 4\pi \int_0^\infty c(r) r^2 \frac{\sin qr}{qr} dr \,. \tag{5.7}$$

For the fractal aggregates with average radius R_0 in the 3-D space, the density-density correlation function is given by

$$c(r) \propto r^{D-3} f(r/R_0), \tag{5.8}$$

where $f(x)$ denotes the cutoff function and is $f(x) \cong \text{const}$ for $x << 1$ and $f(x) << 1$ for $x >> 1$. Substituting Eq. (5.8) into (5.7) and changing the variable of integration $r = z/q$, the structure factor for a fractal aggregate is obtained as

$$S(q) \propto q^{-D} \int_0^\infty z^{D-2} f\left(\frac{z}{qR_0}\right) \sin z \, dz \,. \tag{5.9}$$

This expression is expected to be valid in the range $qR_0 >> 1$ and $qa << 1$. Since $f(x)$ is approximately constant up to large values of z, the integral in Eq. (5.9) only weakly depend on q. Moreover, the phase function $P(q)$ is also approximately constant for $qa << 1$. Therefore, the scattered intensity from a fractal aggregate can be given by

$$I(q) \cong S(q) \propto q^{-D} \tag{5.10}$$

for $1/R_0 << q << 1/a$ and can be used to estimate the fractal dimension of fractal aggregates.

On the other hand, according the DLS theory, the first cumulant of the temporal autocorrelation function of the scattered light is given by

$$K_1 = \frac{1}{I(q,0)} \int s^2 n_s(t) S_s(q) (D_s q^2 + A) ds , \tag{5.11}$$

where D_s and A are the transnational and the rotational diffusion coefficients of clusters of mass s and $I(q,0)$ is the time averaged total scattered intensity. The structure factor of an s-cluster depends on the fractal dimension D in the form $S(q) \propto s^{-1} q^{-D}$ for $qR_0 >> 1$. For fractal aggregates, the dominant contribution to the decay of the temporal autocorrelation function comes from the translation term in which the diffusion coefficient of the cluster can be estimated $D_s \propto R_s^{-1} \propto s^{-1/D}$, where the radius of gyration of an s-cluster is given by $s = s_0 R_s^D$. In this approximation, the first cumulant becomes a moment of the cluster-size distribution function:

$$K_1 \propto \int s^{1-1/D} n_s(t) ds . \tag{5.12}$$

Therefore, the mean cluster size can be estimated by the first cumulant of the temporal autocorrelation function.

The estimations of fractal dimension and the mean cluster size are assumed that the scattered light emerges from the medium after one scattering event and, therefore, can apply to the tenuous colloidal suspension. However, measurements for properties of fractal aggregates in dense suspension have not been established.

5.3 Free path-length distribution function

The FPDF $p(r)$ is defined as a product of the probability that the light can propagate a distance r without encountering any scattering particles and the probability that the light can be scattered at a location r in the medium, and is expressed by

$$p(r)dr = \left[1 - \int_0^r p(r')dr'\right] \times \left[C_{sca} \rho(r) dr\right]. \tag{5.13}$$

In this equation, C_{sca} and $\rho(r)$ denote the scattering cross section of a particle and the number density of particles at the location r, respectively.

In order to obtain the number density of particles, a fractal structure is modeled by a cluster fractal aggregate of particles. The number of particles with the radius a included in a sphere with the radius r is given by [30]

$$N_D(r) = K\left(\frac{r}{a}\right)^D \tag{5.14}$$

where D and K denote a dimension and a volume fraction of the fractal medium, respectively. To compare the fractal aggregates having various dimensions with a homogenous random medium, the constant K is defined as

$$K = {N_3(R)}\Big/{(R/a)^D}, \tag{5.15}$$

which corresponds to a given fraction of the homogeneously random medium. In Eq. (5.15), $R=20\ell$ is the radius of an imaginary sphere which is assumed to be centered at the particle of interest to define the volume fraction of the fractal medium and $N_3(R)$ denotes the number of particles in the imaginary sphere in the homogenous random medium. The number density of particles over a given surface of the sphere with the radius r is obtained from the first derivative of the number of particles and is written, by using Eq. (5.14), as

$$\rho(r) = \frac{1}{4\pi r^2}\frac{d}{dr}N_D(r) = \frac{KD}{4\pi a^3}\left(\frac{r}{a}\right)^{D-3}. \tag{5.16}$$

Substitution of Eq. (5.16) into Eq.(5.13) yields the FPDF of

$$p(r) = \frac{(D-2)}{\ell_D}\left(\frac{r}{\ell_D}\right)^{D-3}\exp\left[-\left(\frac{r}{\ell_D}\right)^{D-2}\right] \tag{5.17}$$

for the fractal aggregate of particles with the dimension of $2.0<D\leq 3.0$. In the derivation of Eq. (5.17), the effective mean free path-length is introduced by

$$\ell_D = a \times \sqrt[D-2]{\frac{4(D-2)}{KDQ_{sca}}} \tag{5.18}$$

as a new measure of randomness in the fractal aggregate from the analogy of the mean free path-length for the homogeneously random medium with the dimension of $D=3$. In Eq. (5.18), $Q_{sca} = C_{sca}/\pi a^2$ denotes a scattering efficiency. In fact, Eqs. (5.17) and (5.18)

can be reduced to $p(r) = \exp(-r/\ell)/\ell$ and $\ell = 1/\rho C_{sca}$, respectively, for D=3.0, which agree with the well-known FPDF and the mean free path-length for the homogeneously random medium. It should be noticed that the procedure in deriving the FPDF from Eq. (5.13) to Eq. (5.17) is quite so general that we could obtain the FPDF for the fractal medium with $D \leq 2$. For $1 < D \leq 2$, we should start to consider Eq. (5.14) as the number of disks with the radius a included in the imaginary circle with the radius r in a plane. We now concern with the characteristics of the coherent backscattering light from the fractal aggregate of particles in the three-dimensional space. Thus, the FPDF for the fractal aggregate given by Eq. (5.17) with the dimension of $2 < D \leq 3$ is used in following simulations.

The FPDFs given by Eq. (5.17) for the dimensions of D=2.5, 2.8 and 3.0 are plotted in Fig. 5.3. As shown in the figure, the probabilities in the regions of $r < \ell_D$ and $r >> \ell_D$ increase with the growth in the aggregate of particles. This means that the particles are distributed densely around a given particle and scarcely exist in the area far away from the particle of interest. Figures 5.4 (a) and (b) show the distributions of particles for the homogeneously random medium with D=3.0 and the fractal medium with D=2.5, respectively. These figures were obtained from the random walk following Eq. (5.17) as the probability density function of the distance between the successive particles. The difference between the particle distributions for D=2.5 and 3.0 is demonstrated clearly in the figure. Namely, the dense and sparse regions of particles coexist for D=2.5 while the particles are distributed homogeneously and randomly for D=3.0. Furthermore, we confirm quantitatively the dimensions of the media, shown in Figs. 5.4 (a) and (b), by using a radius-of-gyration method. Figure 5.5 shows the logarithmic plot of the particle number in a sphere as a function of the radius r given also in a logarithmic scale. In this figure, the solid straight lines with the slopes of 2.5 and 3.0 are plotted for reference. As seen from the figure, the generated distributions of particles shown in Fig. 5.4 have the dimensions just as we designed. Consequently, it becomes obvious that the FPDF given by Eq. (5.17) well describes the fractal aggregate of particles.

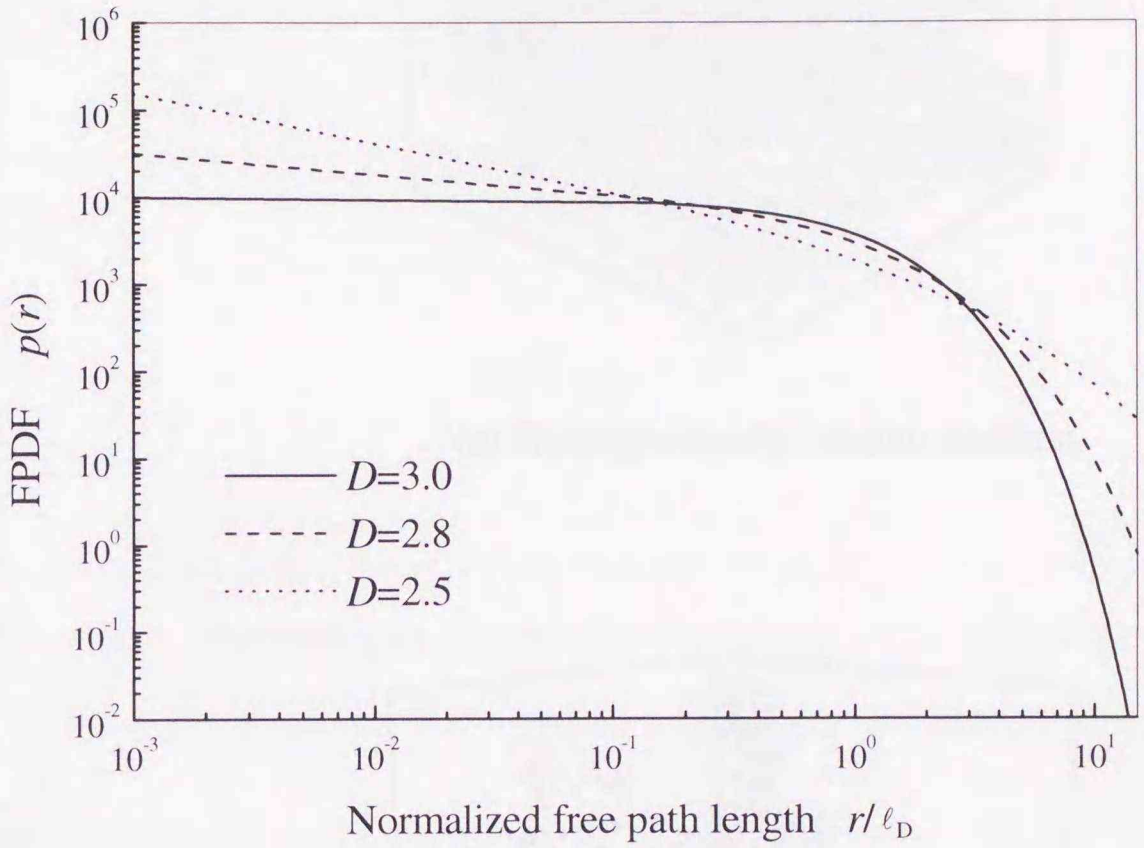

Fig. 5.3 FPDFs for the fractal aggregates of particles with the dimensions of D=2.5 and 2.8 and the homogeneously random medium with D=3.0. The horizontal and vertical axes are plotted in the logarithmic scale and the horizontal axis is normalized by the effective mean free path-length ℓ_D.

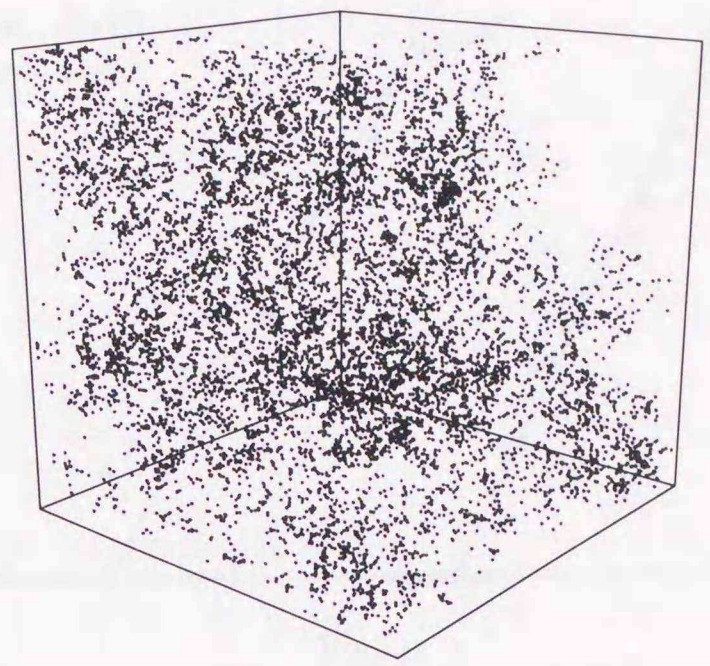

(a) Homogeneously random medium

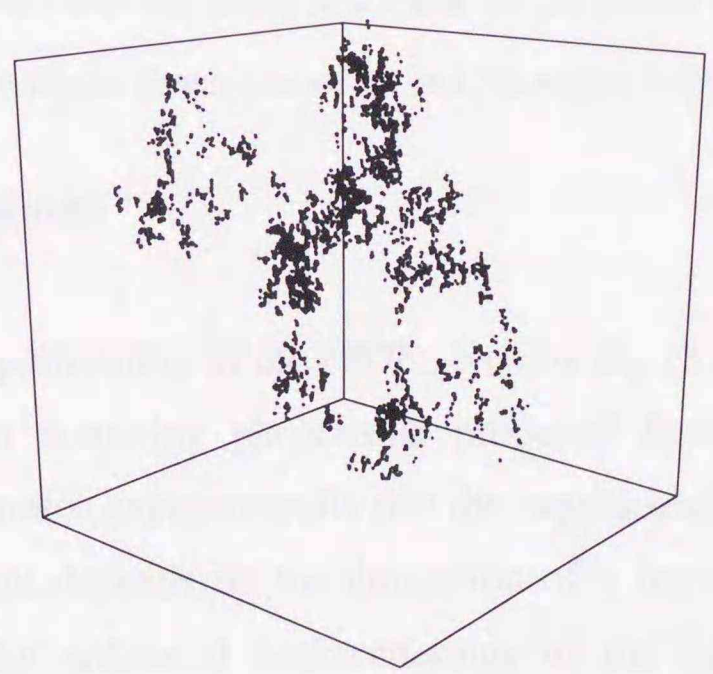

(b) Fractal medium

Fig. 5.4 Particle distributions for (a) the homogeneously random medium with D=3.0 and (b) the fractal medium with D=2.5. They are plotted from the results obtained by a random walk whose free path-length obeys Eq. (5.17).

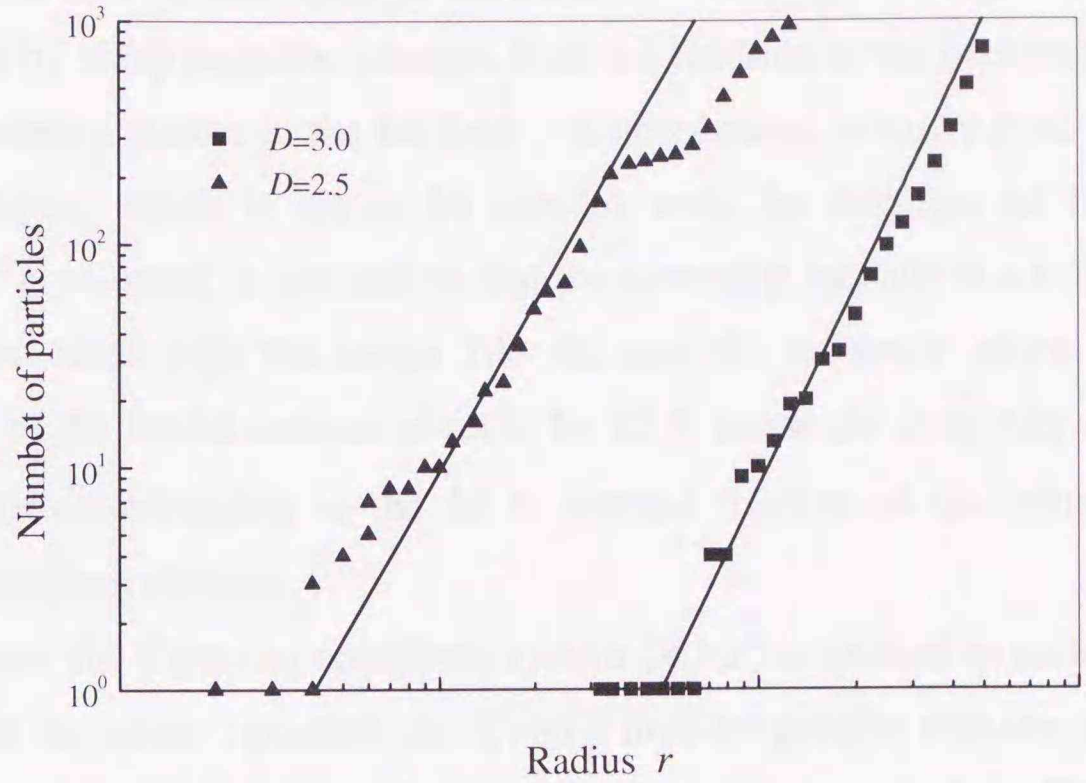

Fig. 5.5 Logarithmic plot of the particle number in a sphere as a function of the radius r given also in the logarithmic scale. The solid lines with the slopes of 2.5 and 3.0 are plotted for reference. ▲ and ■ denote the results for the media with the dimensions of 2.5 and 3.0, respectively.

5.4 Numerical simulations

At this stage, we show the applicability of the FPDF given by Eq. (5.17) together with Eq. (5.18) to analyze the light scattering phenomena produced from the fractal media. Dogariu et al. [114] demonstrated experimentally that the copolarized intensity peak of the enhanced backscattering light depends on the dimension of a fractal aggregate. Thus, Monte Carlo simulations for enhanced backscatterings of the light from the fractal aggregates with various dimensions are conducted as an example of the applicability of the FPDF.

Monte Carlo simulations trace numerically all scattering events and the propagation of light [99]. A trajectory of the photon scattering is simulated by generating the random numbers of the distance between the successive particles and the scattering angles at the events following the FPDF given by Eq. (5.17) and the Rayleigh-Debye scattering phase

function [108], respectively. The linearly polarized light with the wavelength λ=633 nm is incident into the semi-infinite space of the medium. The light undergoes successively scattering events by many particles, emerges from the medium in the backward direction, and forms an intensity pattern in the far field. A copolarized intensity peak is observed through an analyzer which is set to be parallel with the direction of the incident polarization. It is assumed in simulations that the scattering medium is a solution of the polystyrene latex beads with the radius 100 nm and the refractive index 1.59. The volume fraction of the fractal medium is set to be 10 % inside the imaginary sphere with the radius of 20ℓ corresponding to the 10 % volume fraction of the solution for the homogeneously random medium.

In simulations, the Cartesian coordinate system (X,Y,Z) is defined in such a way that its origin is set at the incident position, the X and Z axes are parallel with the directions of the incident polarization and the propagation of light, respectively, and the X and Y axes are included in the boundary plane between the scattering medium and the air. The copolarized intensity distribution detected by scanning in the Y direction is given by [99]

$$\langle I_X \rangle_{ex} = \sum_{n=1}^{\infty} \langle I_{nX} \rangle_{ex} , \tag{5.19}$$

where $\langle \cdots \rangle_{ex}$ stands for an ensemble average over the distribution of the positions at which the light emerges from the medium, and the subscript X denotes the direction of the axis of an analyzer. I_{nX} denotes the n-th order scattering intensity component in the copolarized intensity variation and is given by [99]

$$I_{nX} = \begin{cases} p(1) \Big/ \left[p(1) + 2\sum_{n=2}^{\infty} p(n) F_{nX} \right] & n = 1 \\ 2\,p(n) F_{nX} \left(1 + \cos \Phi_n\right) \Big/ \left[p(1) + 2\sum_{n=2}^{\infty} p(n) F_{nX} \right] & n \neq 1 \end{cases} , \tag{5.20}$$

where $p(n)$ and $\Phi_n = 2\pi\theta_n(Y_n - Y_1)/\lambda$ denote a fraction of the total intensity emerging in the backward direction after a sequence of n scattering events and a phase difference at the emerging position of $Y = Y_n$ along the Y axis, respectively. F_{nX} is the ratio of the copolarized component to the total scattered intensity with the n-th order scattering.

5.5 Results and discussion

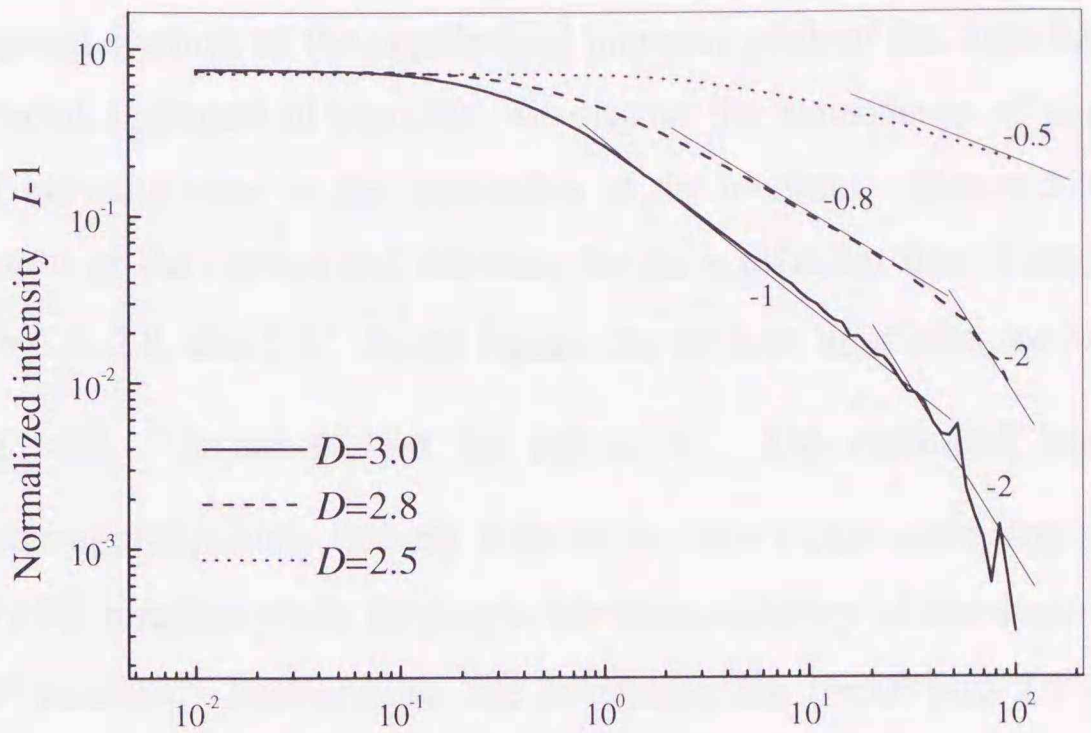

Fig. 5.6 Copolarized angular intensity peak produced in the far field for three dimensions of D=2.5, 2.8 and 3.0, which are scanned along the Y direction perpendicular to the incident polarization. The vertical and horizontal axes denote the logarithms of the coherent intensity $I-1$ and the backscattering angle θ, respectively. In the figure, the lines with the slopes of –0.5, –0.8, –1, and –2 are plotted for reference.

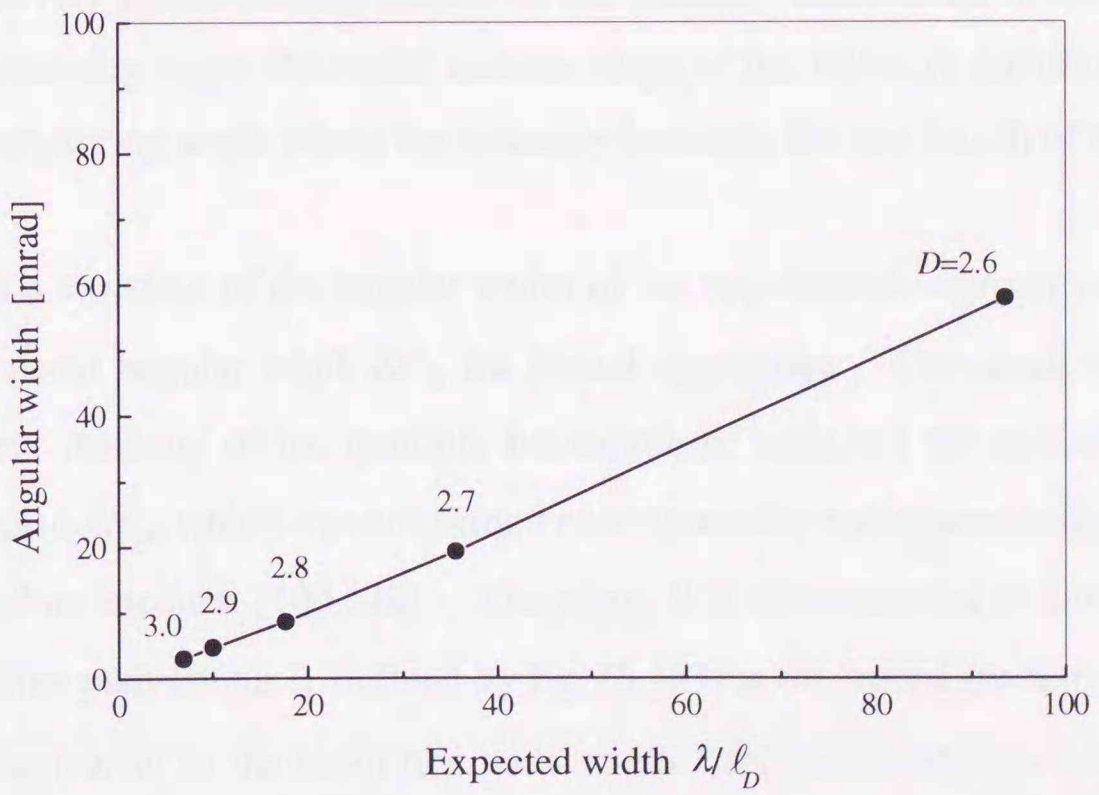

Fig. 5.7 Angular widths of the copolarized intensity peak of the multiply backscattered light as a function of the expected width λ/ℓ_D for the five different aggregates of particles with the dimensions of D=2.6, 2.7, 2.8, 2.9 and 3.0.

To investigate spatial features of the copolarized intensity peak of the light backscattered multiply from fractal aggregate of particles, we discuss the dependence of angular width and the slope of intensity cone on the dimension of the medium. Figure 5.6 shows the angular distributions of the copolarized intensity for three different fractal media with the dimensions of D=2.5, 2.8, and 3.0. In the figure, the straight lines with the slopes of -0.5, -0.8, -1, and -2 are plotted for reference. The enhanced backscattering intensities decrease approximately linearly with an increase of the scattering angle in the region of $10^0<\theta<10^1$ mradian while they coincide independently of the dimension in the region of $\theta<10^0$ mradian. Furthermore, the intensities for D=3.0 and 2.8 decrease in accordance with θ^{-2} in the region of $\theta>10^1$ mradian independently of the dimension but the intensity for D=2.5 spreads too widely to have the line with the slope of -2. Especially, the θ^{-1} and the θ^{-2} dependence of the intensity distribution produced from the homogeneously random medium was derived theoretically by Schmeltzer et al. [119] and confirmed experimentally by Rosenbluh et al. [120]. With the growth in the aggregate of particles, the width of the intensity distribution increases but its slope decreases. To investigate quantitatively the decreasing feature of the intensity distribution in the middle range of the backscattering angle, the width and the slope of the intensity distribution are defined at the backscattering angle where the intensity becomes the one fourth of the peak intensity.

Figure 5.7 shows a variation of the angular width of the copolarized intensity peak as a function of the expected angular width λ/ℓ_D for fractal aggregates. The result indicates that the enhancement intensity of the multiply backscattered light has the angular width directly proportional to λ/ℓ_D, which was confirmed experimentally and theoretically for the homogeneously random medium [100,120]. Therefore, it is demonstrated definitely that the effective mean free path-length ℓ_D defined by Eq. (5.18) for the fractal medium has the physical meaning equivalent to the mean free path-length ℓ for the homogeneous random medium.

Figure 5.8 shows a variation of the slope of the copolarized intensity peak as a function of the dimension of fractal aggregates. It is understood clearly that the slope of the

copolarized intensity peak is directly proportional to the dimension of the medium along the line of $2-D$, thus the intensity decreasing in accordance with θ^{2-D}. The theoretical [108] and experimental [119] results for the homogeneously random medium with D=3 confirmed the $1/\theta$ decreasing dependence of the enhancement intensity at $\theta \approx \lambda/\ell$.

It should be finally noticed that there is the discrepancy between the θ^{2-D} dependence shown in Fig. 5.8 and the θ^{1-D} dependence given experimentally by Dogariu et al [114]. This may be attributed to the difference between the cluster model based on the cluster fractal aggregate of particles and the soft sediment of the cluster-cluster aggregation of particles. They estimated experimentally the dimension of D=1.49 for the soft sediment of the aggregations of the uniformly sized polymethylmethacrylate by means of the conventional box-counting method, while the present Monte Carlo simulation is based on the assumption of the cluster model which cannot describe the fractal structure with the dimension of D<2.

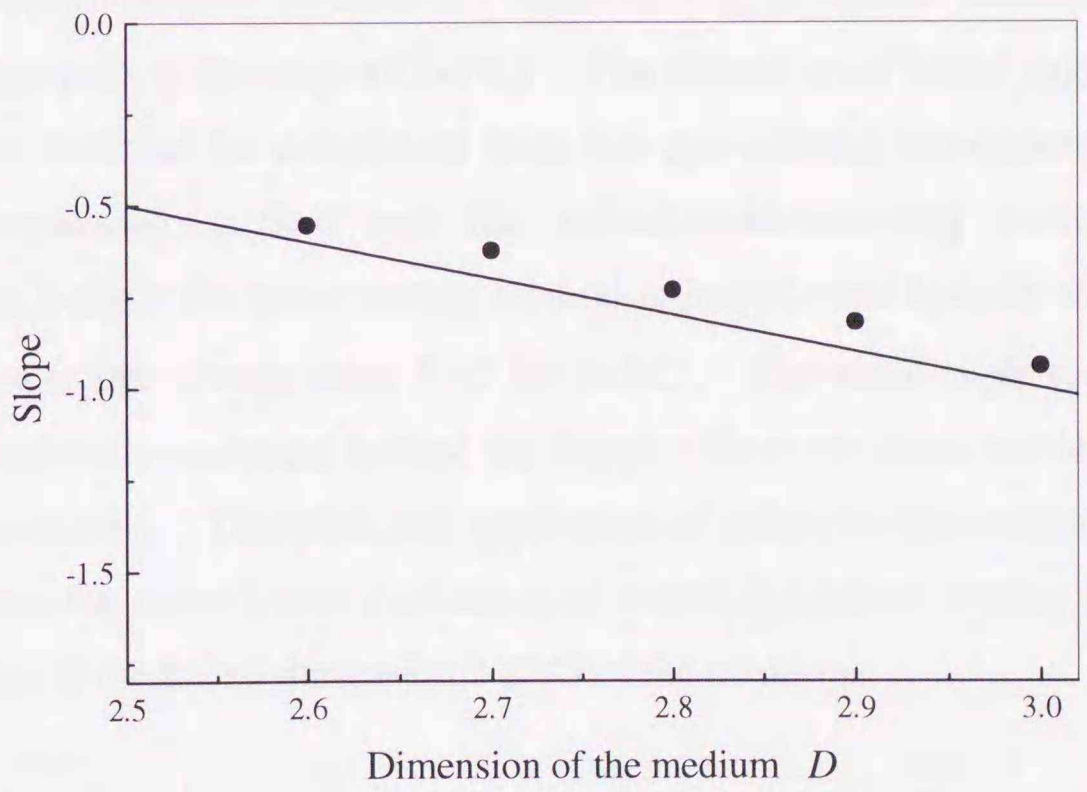

Fig. 5.8 Slope of the copolarized intensity peak of the light backscattered multiply from five different aggregates of particles with the dimensions of D=2.6, 2.7, 2.8, 2.9 and 3.0. The slopes are fitted to the angular intensity distribution in the region around the angle at which the intensity reduces to the one fourth of the peak intensity. In the figure, the solid line denotes the line following $2-D$.

5.6 Conclusion

A free path-length distribution function (FPDF) of the multiply backscattered light has been theoretically derived for the fractal aggregate of particles and the effective mean free path-length has been introduced as a measure of the randomness from the analogy of the homogeneously random medium. The validity of the FPDF was confirmed by demonstrating the agreement between the dimensions designed in particle distributions generated by a random walk on the basis of the derived FPDF and estimated by a radius-gyration method. The FPDF is applied to Monte Carlo simulations for the light backscattered multiply from the fractal aggregate of particles to demonstrate its applicability. In conclusion, the angular width with an order of λ/ℓ_D and the θ^{2-D} dependence of the enhanced backscattering have been demonstrated successfully by means of Monte Carlo simulations on the basis of the FPDF derived theoretically.

From the viewpoint of metrology, the results obtained in this chapter demonstrate clearly the applicability of the enhanced backscattering of light to measure the dimension of fractal aggregates in the range of $2<D\leq3$. The dimension of fractal aggregates with the dimension of $D<2$ can be determined from the conventional box-counting method, the small-angle-scattering method and the second-order-scattering method. For the dimension of $2<D\leq3$, the box-counting method is inapplicable because the dimension of the projection image always takes $D=2$ for $2<D\leq3$. The small-angle-scattering method and the second-order-scattering method are inapplicable to the dense media where the light is hardly transmitted. Therefore, the application of enhanced backscattering of the light produced from the dense fractal medium is an interesting subject worthy to be studied in measurements of the fractal dimension $2<D\leq3$ of the medium.

Chapter 6

Coherent Backscattering of Light from Fractal Aggregates of Particles

6.1 Introduction

There has been much interest in the enhanced backscattering of light from a dense disordered medium, which is produced from a constructive interference between the multiply scattered waves propagating on time-forward and -reversed paths. For a homogeneously random medium, the width of an intensity peak is of the order λ/ℓ [95,121] and the intensity decreases in accordance with $1/\theta$ and $1/\theta^2$ depending on θ [119,120], where λ, ℓ and θ denote the wavelength of the illuminating light, the elastic mean free path-length and the backscattering angle, respectively. Investigation of the enhanced backscattering of light from a fractal medium has been an attractive research problem from both phenomenological and metrological viewpoints. The dimension of tenuous fractal media with $1<D<3$ has been measured successfully by means of a small-angle-scattering method [33,110-112] and a second-order-scattering method [113]. For a dense fractal medium, Dogariu et al. [114] demonstrated experimentally that the intensity peak decreases in accordance with $1/\theta^{1-D}$ and $1/\theta^2$, where D denotes the fractal dimension of the medium.

Due to the difficulty in experimentally controlling the dimension of scattering media, no systematic study has yet been done on the spatio-time statistics of light scattered multiply from the fractal aggregates. In addition, the past studies have been limited to the copolarized intensity enhancement. In preceding chapter, we obtained an analytical form of the free path-length distribution in fractal aggregates of particles [122]. This enables us to conduct numerical simulations of the multiple scattering phenomena in fractal aggregates from the aspect of wave optics. In this chapter, we investigate the polarization properties of angular intensity distributions produced by the coherent multiple backscatterings of light from the fractal aggregates of particles with absorption. We

reveal the dependences of the enhanced backscattering light on the dimension of fractal media and the absorption of their solvents. The formation of the enhanced backscattering intensity distribution from the fractal medium is discussed by taking account of the relation between the intensity distributions in the farfield and in the boundary planes. Consequently, the applicability of the enhanced backscattering light to estimation of the dimension of media is shown from a metrological point of view.

6.2 Simulations

Monte Carlo simulations are conducted as a three-dimensional random walk by tracing all events and paths of the light scatterings inside a fractal aggregate of particles on the basis of the algorithm used by Iwai et al. [99] Suppose that a medium exists in the space of $Z>0$ in an absolute coordinate system (X, Y, Z) and that the plane light polarized linearly along the X direction is incident onto the medium perpendicularly to its boundary plane. The light undergoes successive scattering events by many particles, emerges from the medium in the backward direction, and forms an intensity pattern in the far-field plane. Copolarized and cross-polarized intensity patterns are observed through an analyzer, which is be parallel with and normal to the direction of the incident polarization.

The propagation and scattering of light are simulated using a free path-length distribution function and a Rayleigh-Debye scattering phase function, respectively. A distance vector $r_m = |\vec{r}_m|$ between the successive scattering events is determined as a random number following the free path-length distribution $p(r_m)$ for the fractal aggregate of particles. The free path-length distribution function for a fractal medium with the dimension D in the range of $2.0 < D \leq 3.0$ is given by [122]

$$p(r_m) = \frac{(D-2)}{\ell_D}\left(\frac{r_m}{\ell_D}\right)^{D-3} \exp\left[-\left(\frac{r_m}{\ell_D}\right)^{D-2}\right], \tag{6.1}$$

where ℓ_D is an effective mean free path-length for the fractal aggregate and is defined by

$$\ell_D = a \times \left[\frac{4(D-2)}{KDQ_{sca}}\right]^{1/D-2}. \tag{6.2}$$

In Eq. (6.2), a, Q_{sca} and K denote the radius of particles, the efficiency for scattering, and the constant related to a volume fraction of the fractal medium, respectively. The zenith

angle θ_m and the azimuth angle ϕ_m of the scattered direction at the m-th scattering event obey the probability density functions which are given by the phase function of the Rayleigh-Debye scattering from spherical particles [99,122].

In simulations, the size of particles in the medium is assumed to be 100 nm. The volume fraction of the medium needs to be specified as a parameter in the performance of simulations though the volume fraction cannot be defined intrinsically for the fractal medium distributed in an infinite space. Nevertheless, the volume fraction of the fractal medium is defined in such a way that, if the volume fraction of the particles distributed inside an imaginary sphere with the radius of $R = 20\ell$ is 10%, it corresponds to the 10% homogeneously random medium. In this case, the constant K in Eq. (6.2) is given by $K=N_3(R)/(R/a)^D$, in which $N_3(R)$ denotes the number of particles included inside the sphere with the radius R for the homogeneously random medium. It is further assumed that the solvent suspending the particles is absorbent independently of the scattering event with the absorption coefficient μ_a, thus the scattered light decreases negative-exponentially with an increase of the path-length, i.e. $\exp(-\mu_a s)$.

The copolarized and cross-polarized intensity distributions are calculated by

$$\langle I_X \rangle_{ex} = \sum_{n=1}^{\infty} \langle I_{nX} \rangle_{ex} \quad \text{and} \quad \langle I_Y \rangle_{ex} = \sum_{n=1}^{\infty} \langle I_{nY} \rangle_{ex}, \tag{6.3}$$

respectively, where $\langle \cdots \rangle_{ex}$ stands for an ensemble average over the distribution of the emerging position from the medium. In the equations, the subscripts X and Y stand for the directions of the axes of the analyzer that correspond to the observations of copolarized and cross-polarized intensity distributions. I_{nX} and I_{nY} denote the n-th order scattering intensity components for copolarized and cross-polarized intensity distributions and are given by [99]

$$I_{nX} = \begin{cases} p(1)\mathrm{M}_a(1) \Big/ \left[p(1)\mathrm{M}_a(1) + 2\sum_{n=2}^{\infty} p(n)\mathrm{M}_a(n)F_{nX} \right] & n = 1 \\ 2p(n)\mathrm{M}_a(n)F_{nX}(1+\cos\Phi_n) \Big/ \left[p(1)\mathrm{M}_a(1) + 2\sum_{n=2}^{\infty} p(n)\mathrm{M}_a(n)F_{nX} \right] & n \neq 1 \end{cases} \tag{6.4a}$$

and

$$I_{nY} = p(n)\mathrm{M}_a(n)F_{nY}(1+\Gamma_n\cos\Phi_n) \Big/ \sum_{n=2}^{\infty} p(n)\mathrm{M}_a(n)F_{nY} \qquad n \neq 1, \tag{6.4b}$$

respectively. $p(n)$ and $\Phi_n = k\theta_n(Y_n - Y_1)$ denote a fraction of the total intensity emerging in the backward direction after a sequence of n scattering events and a phase difference at the emerging position of $Y = Y_n$ along the Y axis, respectively. Γ_n denotes a correlation between the waves propagating along the time-forward and -reversed paths. F_{nX} and F_{nY} are the ratios of copolarized and cross-polarized components to the total backscattered intensity with the n-th scattering order. $\mathrm{M}_a(n) = \langle p_n(s)\exp(-\mu_a s)\rangle$ is a decay of the n-th order scattering light due to absorption, in which $p_n(s)$ is a path-length distribution of the n-th order scattering light.

6.3 Results and discussion

Figures 6.1 and 6.2 show the angular intensity distributions of the enhanced backscattering light for three dimensions, D=3.0, 2.8, and 2.5, with the unabsorbent solvent and for five absorbent solvents, μ_a=0, $1/10\ell_D$, $1/5\ell_D$, $1/3\ell_D$, and $1/\ell_D$ with the dimension D=2.8, respectively. In the figures, (a) and (b) correspond to copolarized and cross-polarized intensity components. The intensity peak appears in the angular intensity distribution due to the enhanced backscattering, and its width broadens for both copolarized and cross-polarized intensity components with a growth of the particle aggregation and an increase of the absorption. This behavior is due to the fact that only the light emerging around the incident position contributes to formation of the broader intensity peak in the far-field plane because the effective mean free path-length becomes shorter with a decrease of the dimensions and the light emerging from a point far from the incident position is absorbed more strongly as absorption increases. The peak intensity decreases for the copolarized light, while it increases for the cross-polarized light with a growth of the particle aggregation and an increase of absorption. The dependence of the peak intensity on the dimension and the absorption is caused by an increase of the incoherent contribution for the copolarized intensity and by the correlation Γ for the cross-polarized intensity due to an increase of the contributions in single and low-order scatterings with a growth of the particle aggregation and an increase of the absorption. It is interesting in the case of $\mu_a > 1/3\ell_D$ that the cross-polarized light produces a higher intensity peak than the copolarized light.

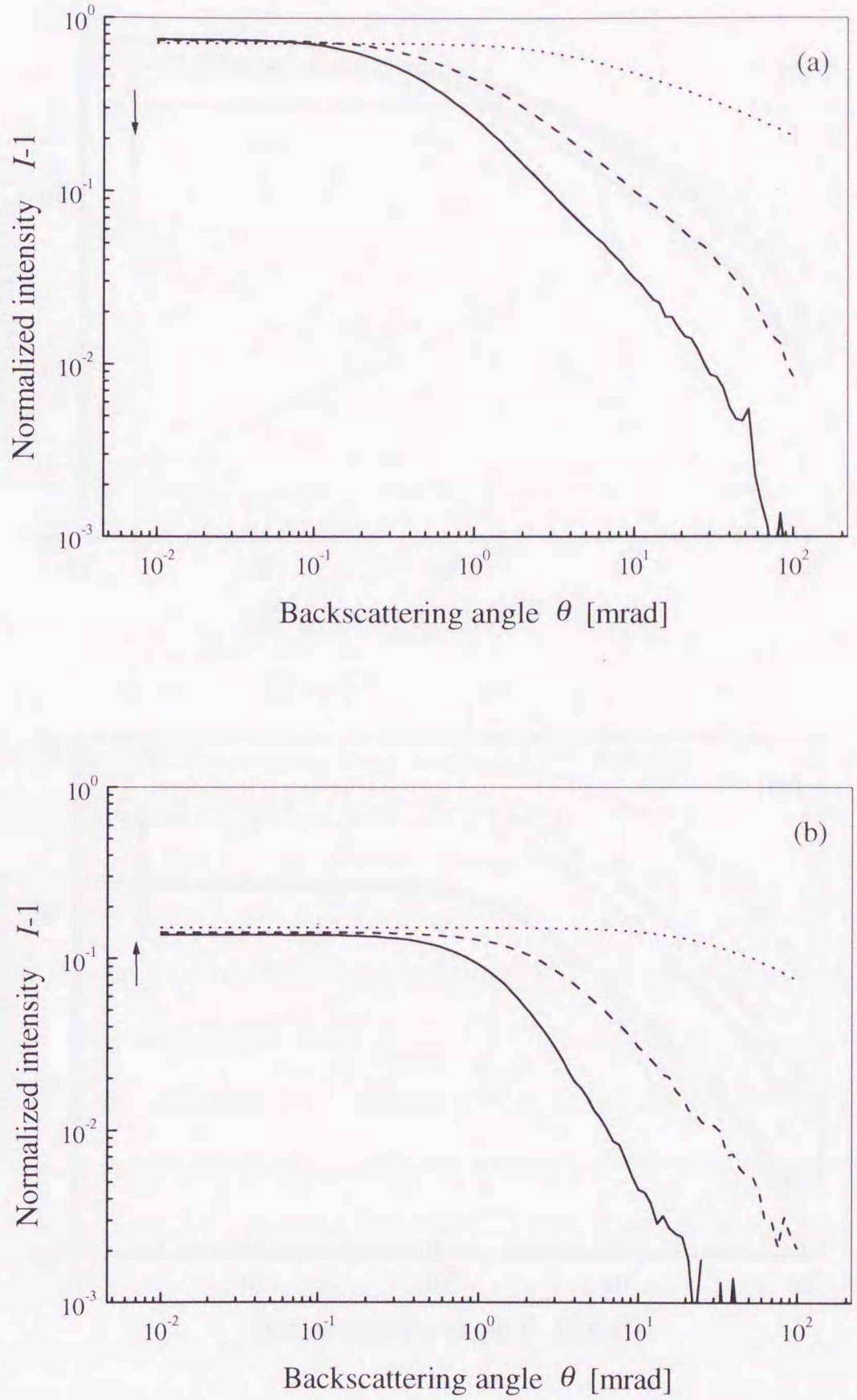

Fig. 6.1 Logarithmic plots of (a) copolarized and (b) cross-polarized angular intensity distributions of enhanced backscatterings from the fractal media with three different dimensions of D=3.0(———), 2.8(------), and 2.5(·····) as a function of the backscattering angle θ in a logarithmic scale. The arrow shows the direction of intensity variation growing in the aggregation of particles.

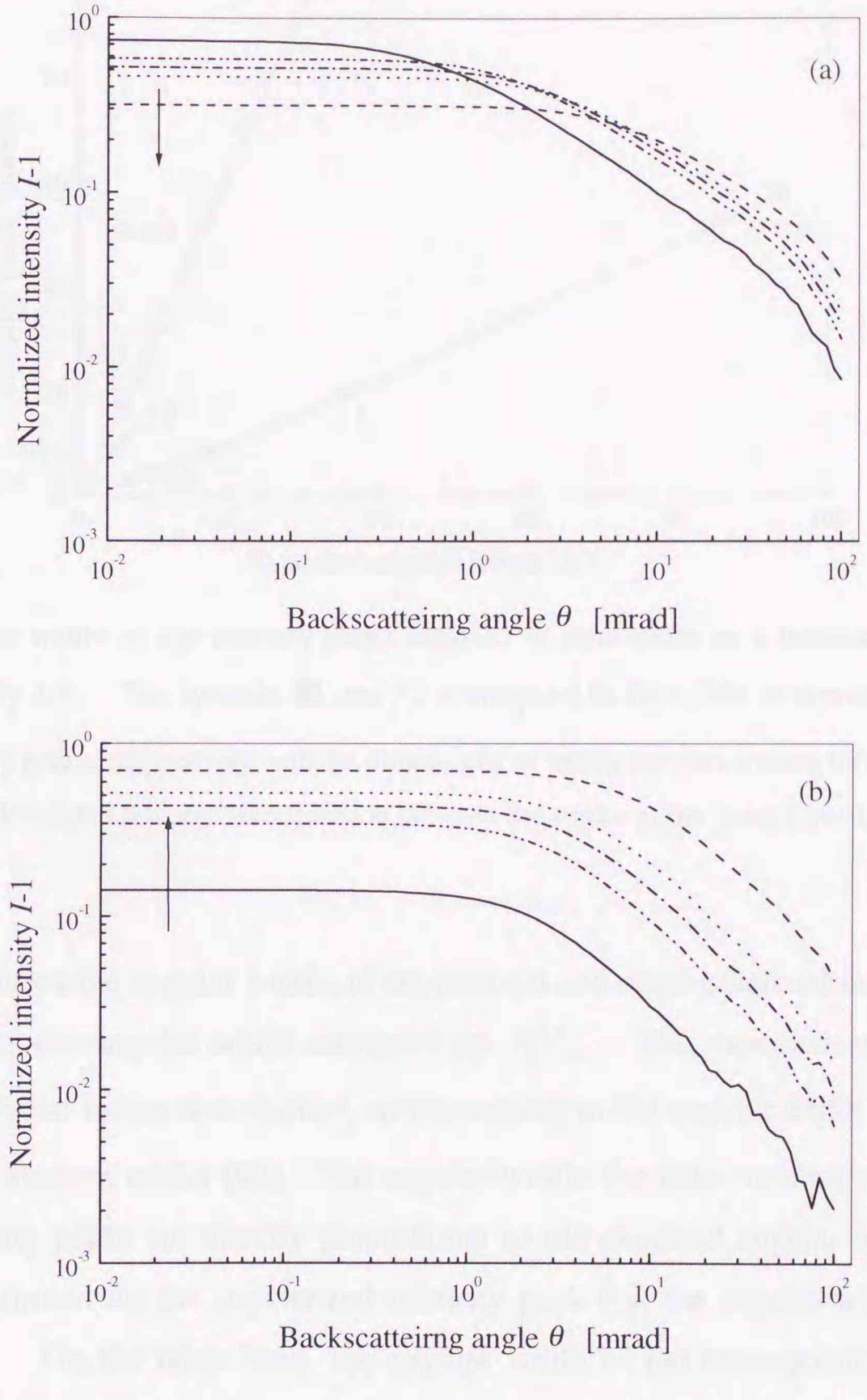

Fig. 6.2 Logarithmic plots of (a) copolarized and (b) cross-polarized angular intensity distributions of enhanced backscatterings from the absorbent fractal media with five different absorption coefficients of $\mu_a=1/\ell_D$(———), $1/3\ell_D$(- - - - - -), $1/5\ell_D$(·····), $1/10\ell_D$(—·—·—·), and 0(—··—··—) for the fractal dimension D=2.8 as a function of the backscattering angle θ in a logarithmic scale. The arrow shows the direction of intensity variation increasing the absorption.

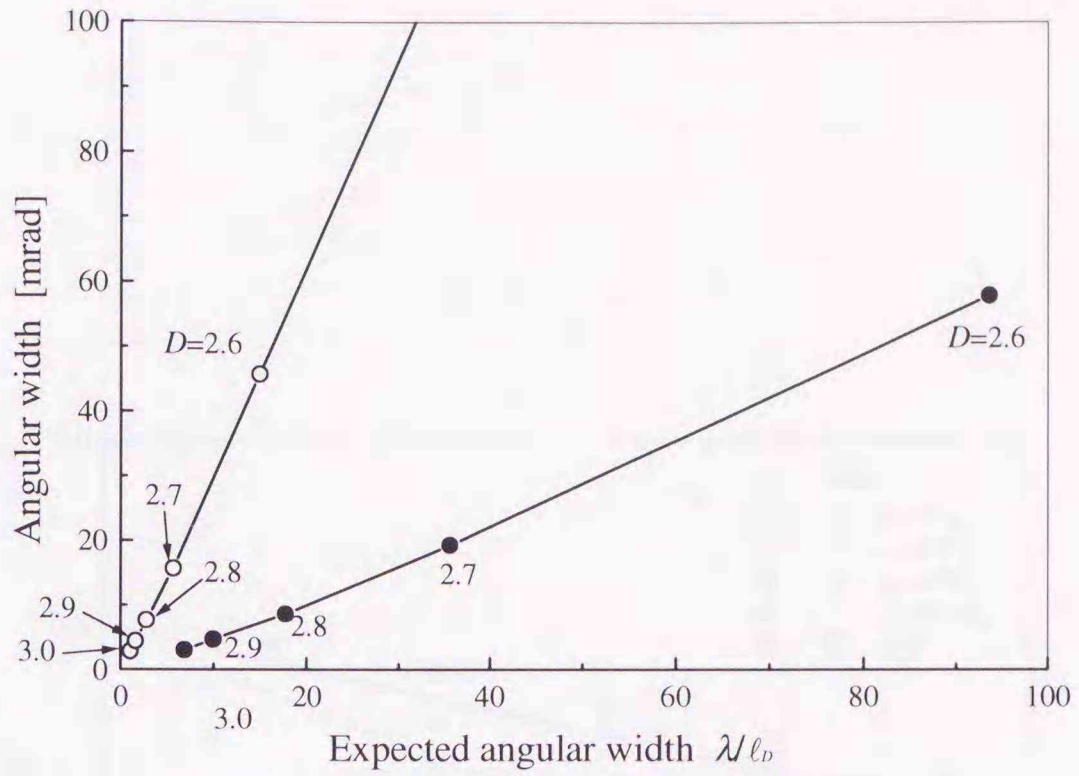

Fig. 6.3 Angular widths of the intensity peaks obtained in simulations as a function of the angular width estimated by λ/ℓ_D. The symbols ● and ○ correspond to the widths of copolarized and cross-polarized intensity peaks, respectively, and the dimensions of media are also written for reference. The angular width is defined as the angular separation between the angles at the quarter intensity of the peak.

Figures 6.3 shows the angular widths of copolarized and cross-polarized intensity peaks as a function of the angular width estimated by λ/ℓ_D. The expected angular width λ/ℓ_D for the fractal media was defined, corresponding to the angular width λ/ℓ for the homogeneously random media [99]. The angular widths for both copolarized and cross-polarized intensity peaks are directly proportional to the expected angular widths. It is particularly confirmed for the copolarized intensity peak that the angular width is of the order of λ/ℓ_D. On the other hand, the angular width of the cross-polarized intensity peak is much wider than that of the copolarized intensity peak because the high-order scattered components that produce a narrow intensity peak do not contribute to the formation of the cross-polarized intensity peak due to the correlation factor Γ. The effective mean free path-length ℓ_D defined by Eq. (6.2) for the fractal medium thus has a physical meaning equivalent to the mean free path-length ℓ in the homogeneously random medium only for the copolarized light.

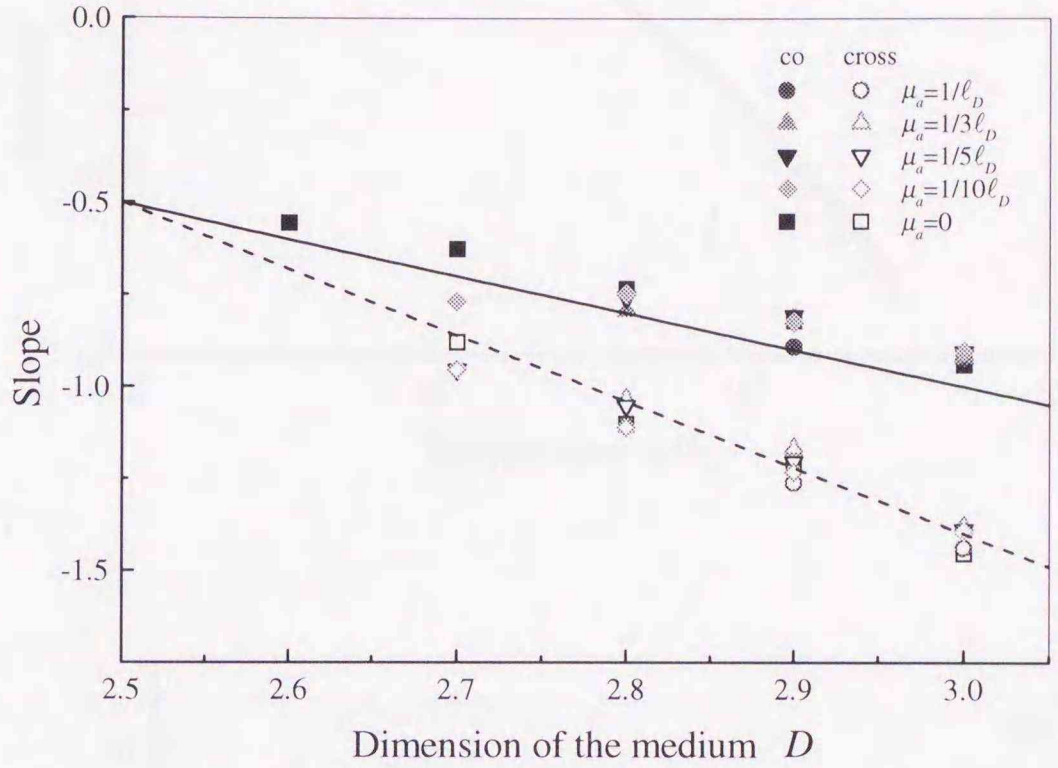

Fig. 6.4 Angular widths of the intensity peaks obtained in simulations as a function of the angular width estimated by λ/ℓ_D. The symbols ● and ○ correspond to the widths of copolarized and cross-polarized intensity peaks, respectively, and the dimensions of media are also written for reference. The angular width is defined as the angular separation between the angles at the quarter intensity of the peak.

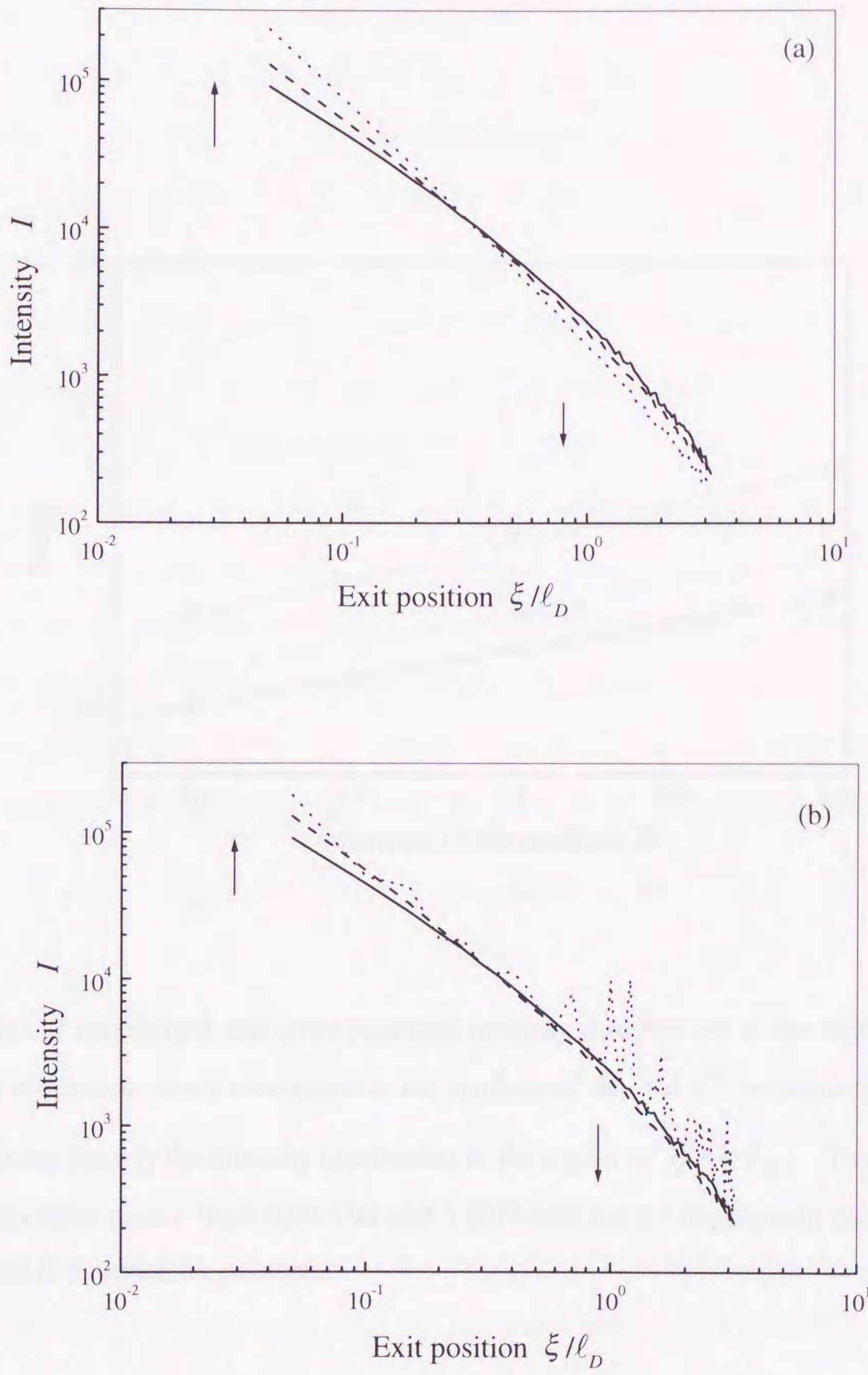

Fig. 6.5 Logarithmic plots of (a) copolarized and (b) cross-polarized intensity distributions produced in the boundary plane for a point source incidence for the fractal media with three different dimensions of D=3.0(———), 2.8(------), and 2.5(·····) as a function of the normalized emerging position ξ/ℓ_D in a logarithmic scale. The arrows show the directions of intensity variation growing in the aggregation of particles.

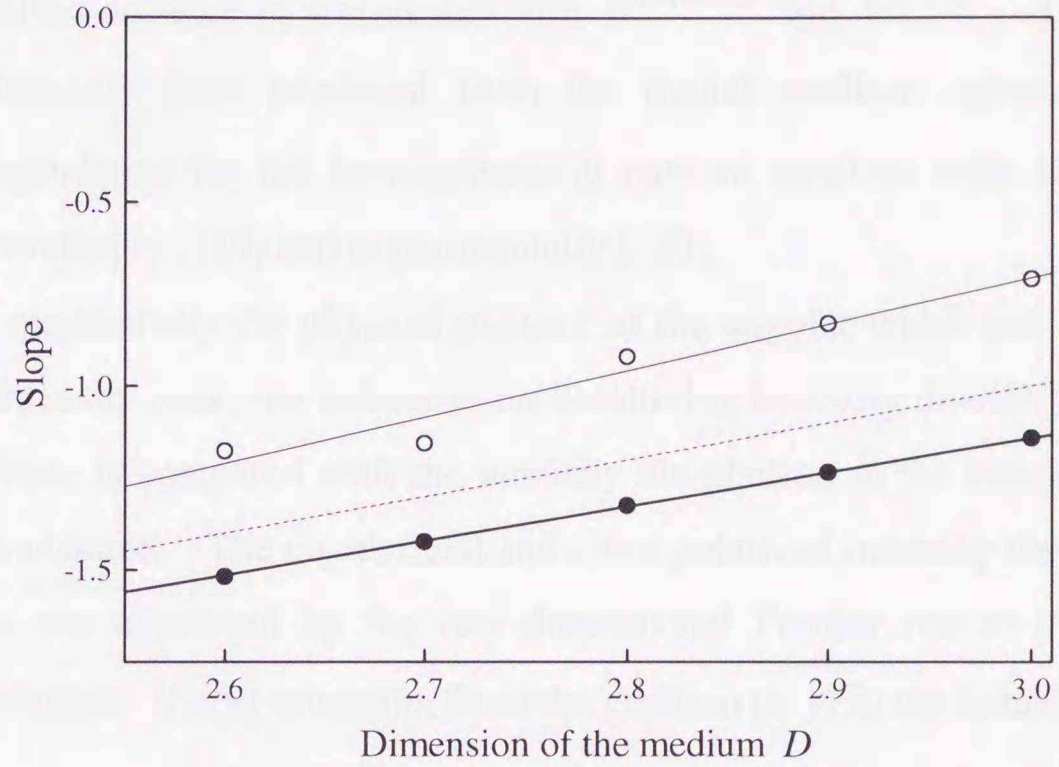

Fig. 6.6 Slopes of copolarized and cross-polarized intensity distributions in the boundary plane as a function of the dimension, which correspond to the symbols of ● and ○, respectively. The slope is estimated by fitting linearly the intensity distribution in the region of $\xi << \ell_D$. The thick solid, thin solid and broken lines denote the $0.93D$-3.94 and $1.07D$-3.98 for the copolarized and cross-polarized components, and D-4 plotted for reference.

Figure 6.4 shows the slopes of the intensity decay in (a) copolarized and (b) cross-polarized intensity peaks as a function of the dimension for five different absorption coefficients of μ_a=0, $1/10\ell_D$, $1/5\ell_D$, $1/3\ell_D$, and $1/\ell_D$. The slope of the enhanced backscattering light is shown to be directly proportional to the dimension of the medium and independent of absorption. In addition, the slopes of the copolarized and cross-polarized intensity distributions vary, following the lines of $2.16\text{-}1.03D$ and $4-1.8D$, and thus the intensities decrease in accordance with $\theta^{2.16-1.03D}$ and $\theta^{4-1.8D}$. The result for the copolarized intensity peak produced from the fractal medium agrees with the $1/\theta$ decreasing dependence for the homogeneously random medium with D=3, which was confirmed theoretically [119] and experimentally [120].

To specify qualitatively the physical pictures of the angular width and the slope of the decay in the intensity peak, the enhanced backscattering intensity distribution produced in the far-field plane is compared with the intensity distribution in the boundary plane for a point source incidence. The copolarized and cross-polarized intensity distributions in the far-field plane are expressed by the two dimensional Fourier cosine transform of the intensity distribution $I(x, y)$ emerging from the position (x, y) in the boundary plane:

$$I_X(k_x, k_y) = \iint I(x, y)\cos(k_x x + k_y y)dxdy \tag{6.5a}$$

and

$$I_Y(k_x, k_y) = \iint I(x, y)\Gamma\cos(k_x x + k_y y)dxdy, \tag{6.5b}$$

respectively. In the equations, k_x and k_y denote x- and y-components of a wave vector of the backscattered light, respectively. The correlation Γ between the lights propagating along the time-forward and -reversed paths contributes dominantly to the cross-polarized intensity distribution, while it is unity for the copolarized intensity distribution in the same manner as Eq. (6.4).

Figures 6.5 (a) and (b) show copolarized and cross-polarized intensity distributions in the boundary plane for a point source incidence, respectively. The horizontal axis in the figure denotes the emerging position ξ normalized by the effective mean free path-length ℓ_D. The cross-polarized intensity distributions shown in Fig. 6.5 (b) show the irregular fluctuation in intensity. This comes from the lack of photons that come around to the

boundary plane for one million incident photons. The intensities in $\xi<\ell_D$ and $\xi>\ell_D$ increase and decrease with the growth of particle aggregation, respectively, whose variation in $\xi<\ell_D$ is larger in magnitude than that in $\xi>\ell_D$. The light distributions in $\xi<\ell_D$ and $\xi>\ell_D$ contribute approximately to the enhanced backscattering lights produced in the regions of $\theta>10^0$ mrad and $\theta<10^0$ mrad of the far-field plane, respectively. If the light propagates along a longer path than ℓ_D until emerging from the boundary plane, its direction after multiple scatterings is fully randomized, thus losing the memory of the dimension. This is the reason the multiple-backscattering enhancement takes an approximately constant intensity independent of the dimension in the region of $\theta<10^0$ as shown in Fig. 6.1. On the other hand, since most of the light backscattered in $\xi<<\ell_D$ propagates along the path much shorter than ℓ_D, the scattered light is not fully randomized in direction but still preserves the memory of the dimension. As a result, the intensity of the backscattered light in the region $\theta>>10^0$ of the boundary plane increases with the growth of the particle aggregation as shown in Fig. 6.1.

Figure 6.6 shows the slopes of copolarized and cross-polarized intensity distributions in the boundary plane as a function of the dimension. The slopes of the decay in both distributions are directly proportional to the dimension of the medium. Variations in the slopes for the copolarized and cross-polarized components approximately agree with the lines of $0.93D$-3.94 and $1.07D$-3.98, and the intensity distributions thus vary approximately with $\xi^{0.93D-3.94}$ and $\xi^{1.07D-3.98}$ in the region of $\xi<<\ell_D$, respectively. Especially, $\xi^{0.93D-3.94}$ for the copolarized intensity distribution is fairly well approximated to ξ^{D-4} with the accuracy of the numerical simulation. The intensity distribution proportional to ξ^{D-4} gives rise to the angular distribution proportional to θ^{2-D} because the intensity distribution around the incident point is related to the angular intensity distribution in the region of a large scattering angle by the two-dimensional Fourier transformation. Comparison between Figs. 6.4 and 6.6 shows that this relation is confirmed only for the copolarized intensity distribution, but not for the cross-polarized one. This conflict may be attributed to the correlation factor Γ between the lights propagating along the time-forward and -reversed paths in the formation of the cross-polarized intensity.

6.4 Conclusions

Using Monte Carlo simulations, we investigated the angular intensity distribution of the light backscattered multiply from the fractal aggregate of particles. The angular width and the slope of the intensity peak depend on the dimension of the medium, but the height of the intensity peak is approximately independent of the dimension. In contrast, the angular width and the height of the intensity peak depend strongly on the absorption of the solvent. The angular widths of copolarized and cross-polarized backscattering intensity enhancements are directly proportional to λ/ℓ_D. It is revealed that the effective mean free path-length ℓ_D has the same physical meaning as the mean free path-length ℓ for the homogeneously random medium since the angular width for the copolarized component is on the order of the angular width of λ/ℓ_D. Copolarized and cross-polarized components of the backscattering intensity enhancement decrease in accordance with $\theta^{2.16-1.03D}$ and $\theta^{4-1.8D}$ in the far-field plane and with $\xi^{0.93D-3.94}$ and $\xi^{1.07D-3.98}$ in the boundary plane between the scattering medium and the air, respectively. It is thus confirmed that the two-dimensional Fourier transform relation between the intensity distributions in the far-field and the boundary planes is approximately satisfied only for the copolarized component but not for cross-polarized one. This difference may be attributed to the correlation factor Γ between the lights propagating along the time-forward and -reversed paths in the formation of the cross-polarized intensity.

Finally, we should notice the applicability of the enhanced backscattering light to estimation of the dimension of the medium. The slope of the intensity decay of the intensity peak is directly proportional to the dimension of the medium but is independent of the absorption. Therefore, we can estimate the dimension of the medium uniquely by measuring the slope of the intensity decay without being affected by the absorption of the solvent.

Chapter 7

Coherent Backscattering of Light from Aggregated Particles in Absorbent Colloidal Suspensions

7.1 Introduction

The multiple backscattering of light from a dense disordered medium generates an intensity peak phenomenon in the far field. It comes from the constructive interference between the lights propagating along time-forward and -reversed paths. For the homogeneously disordered medium, the peak intensity distribution decreases as a function of the backscattering angle θ in accordance with θ^{-1} [119-120] and spreads over the range of an order λ/ℓ in backscattering angle [95,121], where ℓ denoting the mean free path-length of the medium. It is expected that the peak intensity distribution will change as the particles aggregate since the spatial properties of the particle distribution in the suspension may be contributed to formation of the intensity enhancement. Dogariu et al. found experimentally that the peak intensity distribution produced from fractal cluster sediments of PMMA decreases in accordance with θ^{1-D}, where D denoting fractal dimension of the medium [114]. Ishii et al. obtained numerically the empirical formulae of $\theta^{2.16\text{-}1.03D}$ and $\theta^{4\text{-}1.8D}$ for the decreasing variation of copolarized and cross-polarized peak intensity distributions from a cluster of particles, respectively [123,124].

In this chapter, the copolarized and cross-polarized peak intensity distributions produced from the absorbent colloidal suspensions of the polystyrene latex beads are investigated experimentally with the relation to the aggregation of particles. The dimension of the medium can be estimated by applying the decreasing slope to the empirical formulae obtained in the preceding chapter. Especially, the discrepancy between the dimensions estimated from the copolarized and cross-polarized peak intensity distributions is discussed with the relation to the spatial distribution of the particles in the suspension. The further experimental investigation is conducted on the dependence of the peak intensity variation

on the absorption. Finally, it is concluded that the analysis of the backscattering enhancement of light is available to the watching of the aggregation process in the absorbent colloidal suspension and enables us to estimate the fractal dimension of the medium without the degradation of the accuracy.

7.2 Experiments

Fig. 7.1 shows schematically the experimental setup to observe the 2-D intensity distributions of the backscattering enhancement from dense disordered media. The polarized plane wave emitted from an Ar^+ laser with the wavelength of λ=514.5 nm and the diameter of 6 mm illuminates the colloidal suspension in a glass cell through beamsplitter, which is used to observe the light scattered in the direction of retroreflection. The glass cell is inclined against the optical axis to eliminate the light reflected from its front surface. An aperture with the same size as the illuminating area is placed closely to

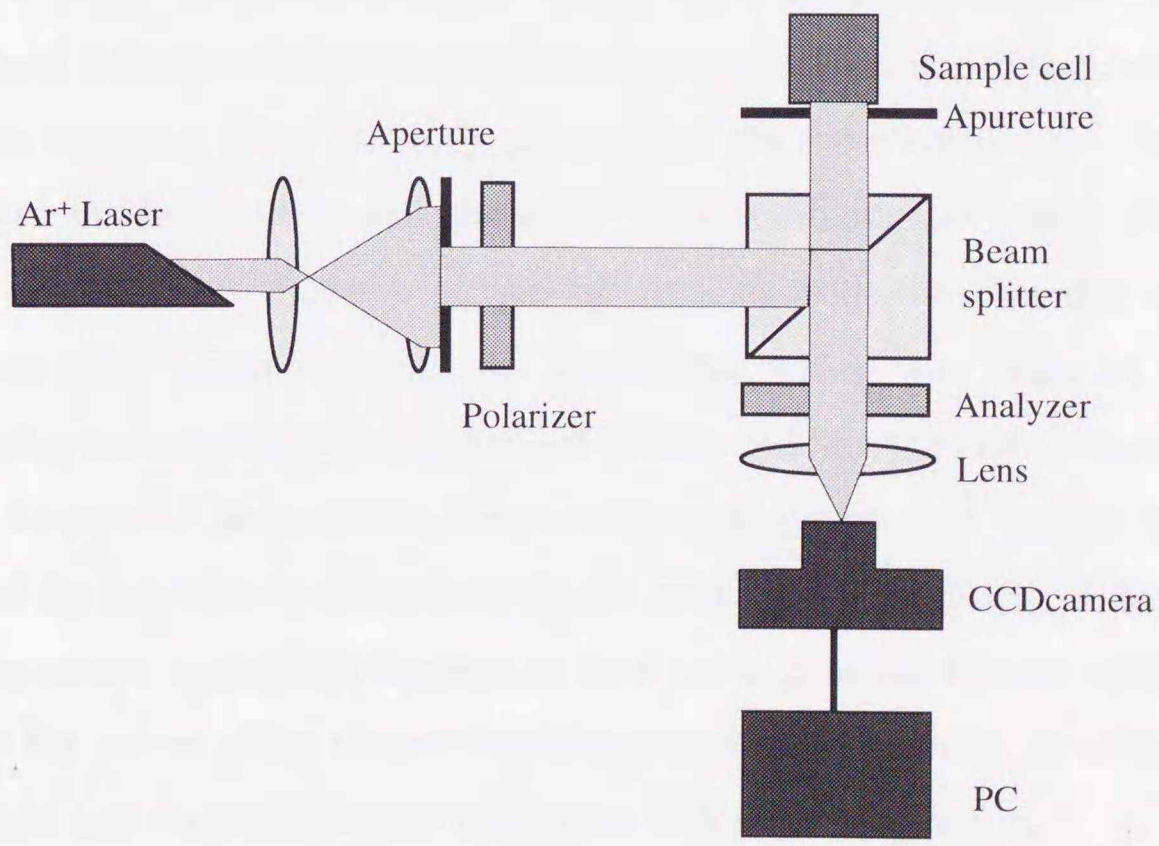

Fig. 7.1 Schematic diagram of an experimental setup for measuring the peak intensity distribution of the backscattering enhancement from a dense disordered medium.

the front surface of the cell to block out the light emerging from the outside of the illuminating area. The 2-D intensity distribution backscattered multiply from the colloidal suspension is detected by a CCD camera placed in the focal plane of the lens at a distance of 50 mm. The CCD camera has 768×512 pixels with the area 9μm×9μm a pixel so that the angular range and resolution in the observation are ±50 and 0.18 in mradian, respectively. The copolarized or cross-polarized intensity distributions was selected by setting the direction of analyzer placed in front of the lens to be parallel with or perpendicular to the direction of incident polarization. It should be noticed that the optical setup shown in Fig. 7.1 possessed inherently the angular dependence in the detected intensity distribution. To eliminate such the influence, the detected 2-D intensity distribution was divided by that produced from the glass cell illuminated on the backward wall.

In the experiments, the polystyrene latex spheres with diameters of 0.09 μm, 0.46 μm, and 1.0 μm manufactured by Sigma Chemical Co. were prepared as the three different colloidal suspensions with the volume fraction of 10%. Repulsion and an attractive force are exerted on the particles in the colloidal suspension, which are generated by the ions sticking on the surface of particle and the Van der Walls force, respectively. A potential barrier is formed at the boundary between the particle and solvent due to the electric double layer, thus the repulsion being generally greater than the attractive force. The particles keep a distance from each other and, therefore, disperse homogeneously in the colloidal suspension. Fig. 7.2 (a) shows a picture of particles with the diameter of 1.0 μm homogeneously dispersed in the colloidal suspension, which was taken by an optical microscope after enough dilution by deionized water. Adding the NaCl solution to such the colloidal suspension, the potential barrier become lower because the ions sticking on the surface of the particles is neutralized by the induced ions of NaCl. The diffusion-limited cluster-cluster aggregation happens as soon as the potential barrier vanishes. Fig. 7.2 (b) shows the picture of the cluster-cluster aggregations of particles, in which particles generate clusters and clusters distribute homogeneously in the suspension.

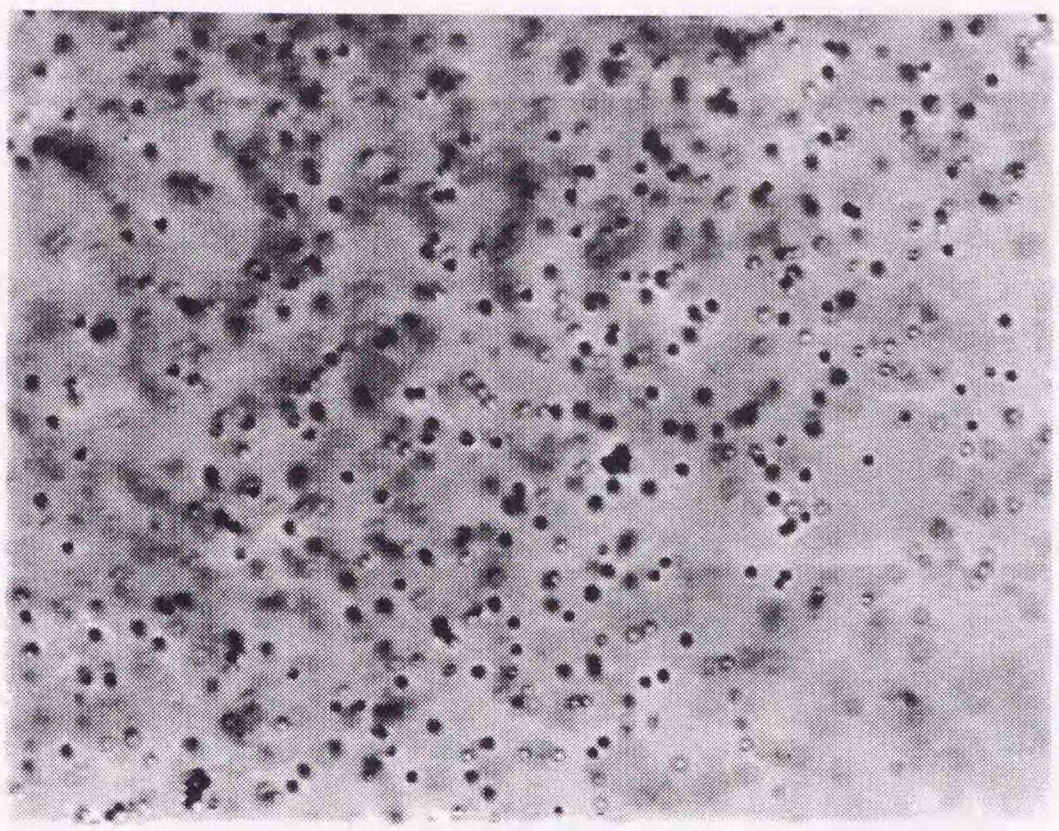

(a)

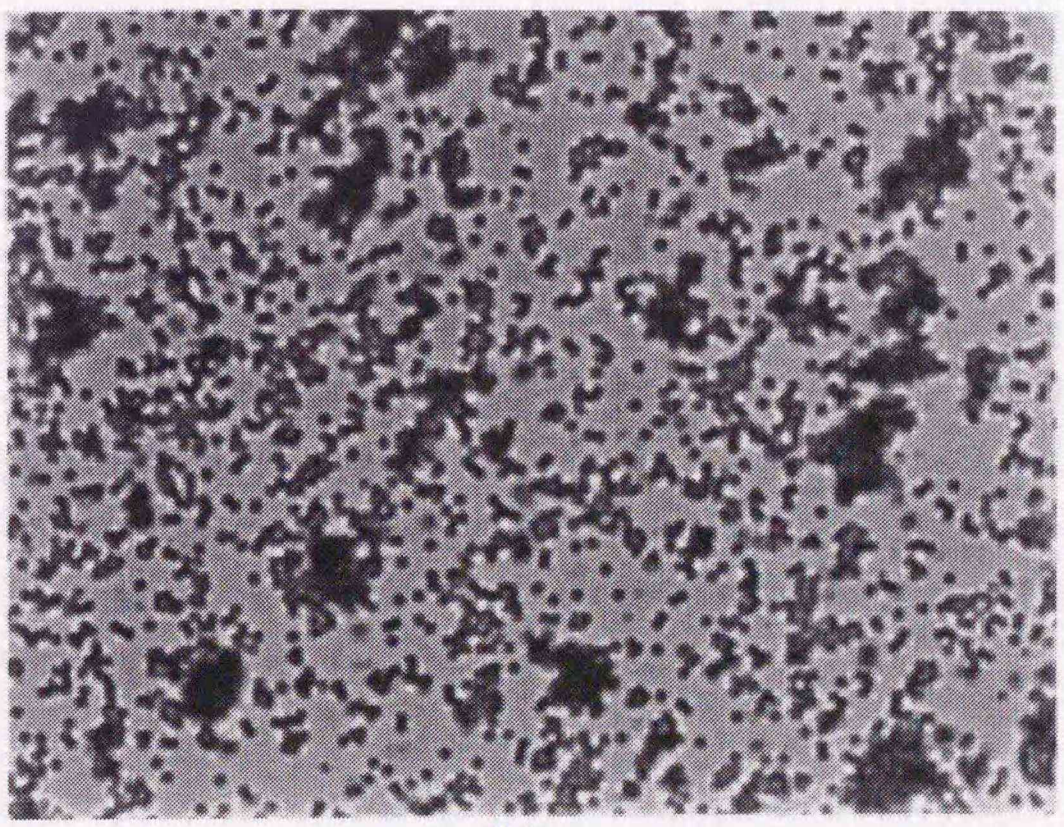

(b)

Fig. 7.2 Distributions of particles in the colloidal suspension (a) without and (b) with the NaCl solution, which were taken by a CCD camera mounted on an optical microscope. Particles disperse homogeneously in 3D space and form clusters as shown in (a) and (b), respectively.

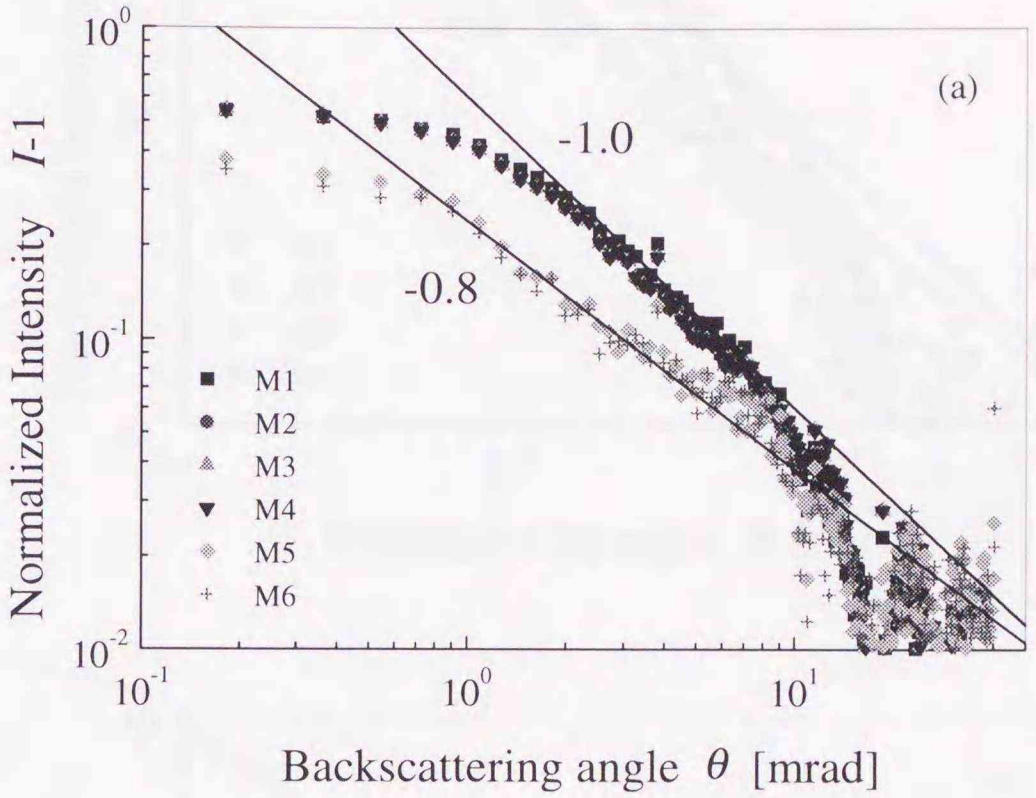

Fig. 7.3 Copolarized peak intensity distributions of backscattering enhancements produced from the colloidal suspensions of particles with the diameters of (a) 1.0 μm, (b) 0.46 μm, and (c) 0.09 μm. M1, M2, M3, M4, M5, and M6 correspond to the added amount of NaCl solutions of 0 ml (■), 0.25 ml (●), 0.5 ml (▲), 0.75 ml (▼), 1.00 ml (◆), and 1.25 ml (✚) to 3 ml colloidal suspension, respectively. The normalized intensity I–1 is plotted as a function of the backscattering angle θ in the logarithmic scale. The solid lines show the decreasing lines corresponding to the peak intensity variations and the attached numbers denote their slopes.

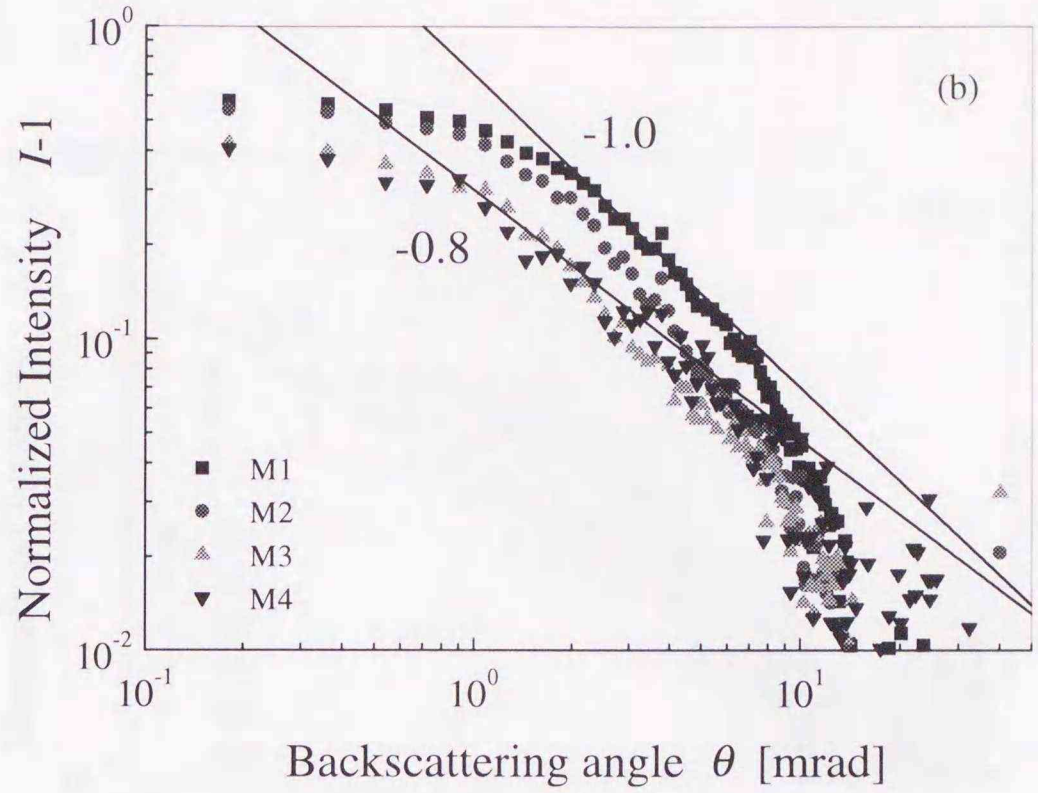
(b)
-1.0
-0.8
M1
M2
M3
M4
Normalized Intensity I-1
Backscattering angle θ [mrad]

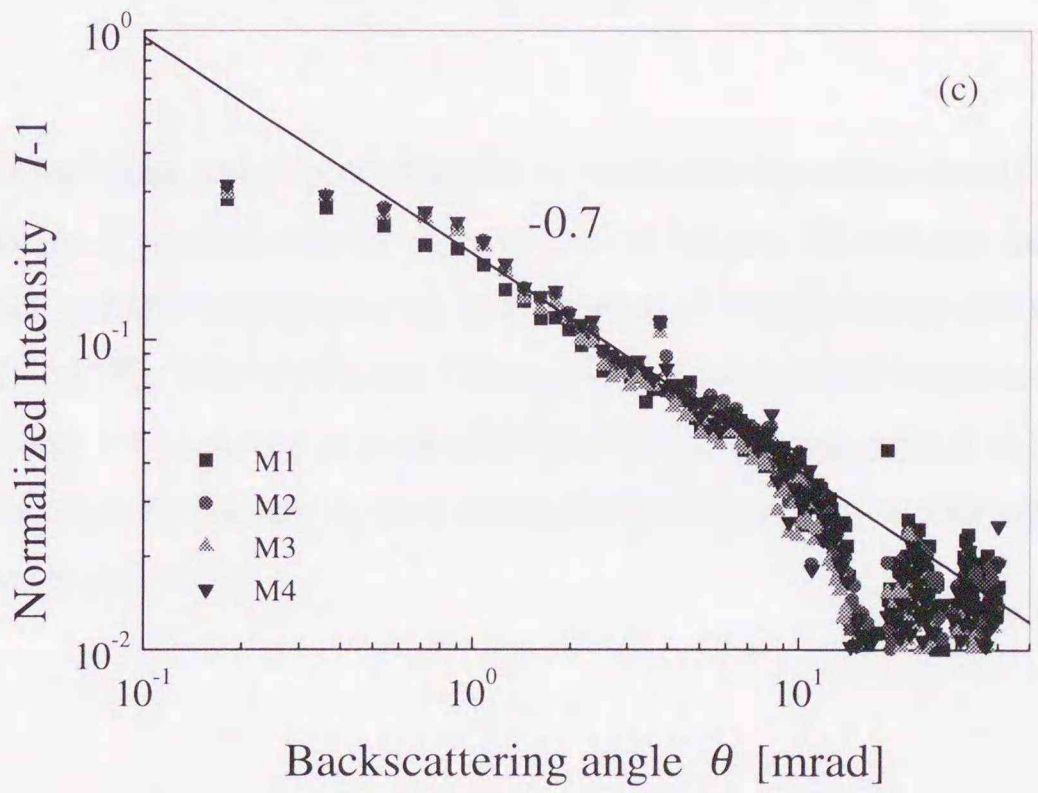
(c)
-0.7
M1
M2
M3
M4
Normalized Intensity I-1
Backscattering angle θ [mrad]

(continued)

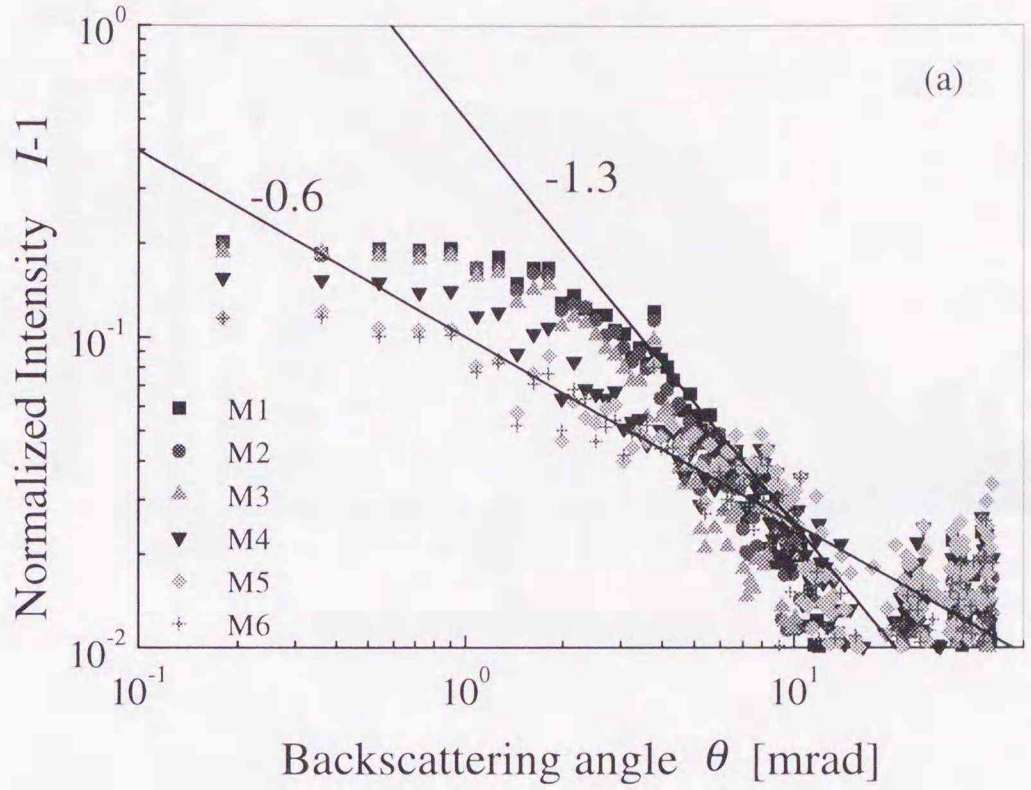

Fig. 7.4 Cross-polarized peak intensity distributions of backscattering enhancements produced from the colloidal suspensions of particles with the diameters of (a) 1.0 μm, (b) 0.46 μm, and (c) 0.09 μm. M1, M2, M3, M4, M5, and M6 correspond to the added amount of NaCl solutions of 0 ml (■), 0.25 ml (●), 0.5 ml (▲), 0.75 ml (▼), 1.00 ml (◆), and 1.25 ml (✚) to 3 ml colloidal suspension, respectively. The normalized intensity $I-1$ is plotted as a function of the backscattering angle θ in the logarithmic scale. The solid lines show the decreasing lines corresponding to the peak intensity variations and the attached numbers denote their slopes.

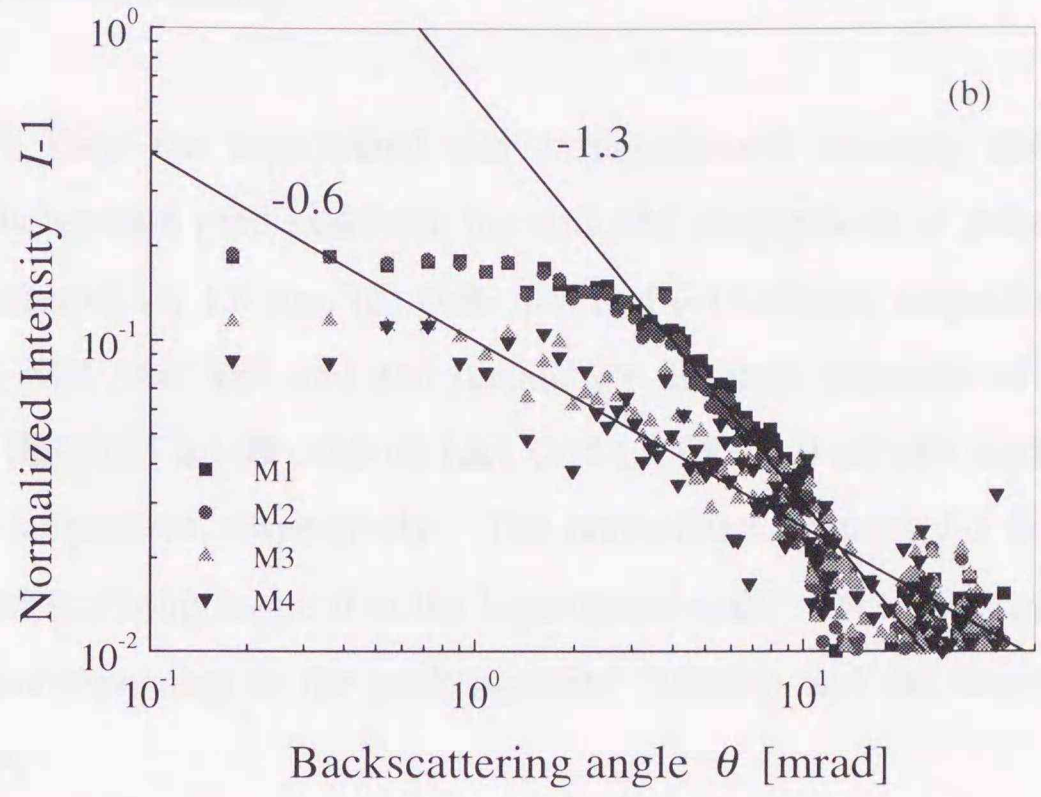
(b)
-1.3
-0.6
M1
M2
M3
M4
Normalized Intensity I-1
Backscattering angle θ [mrad]

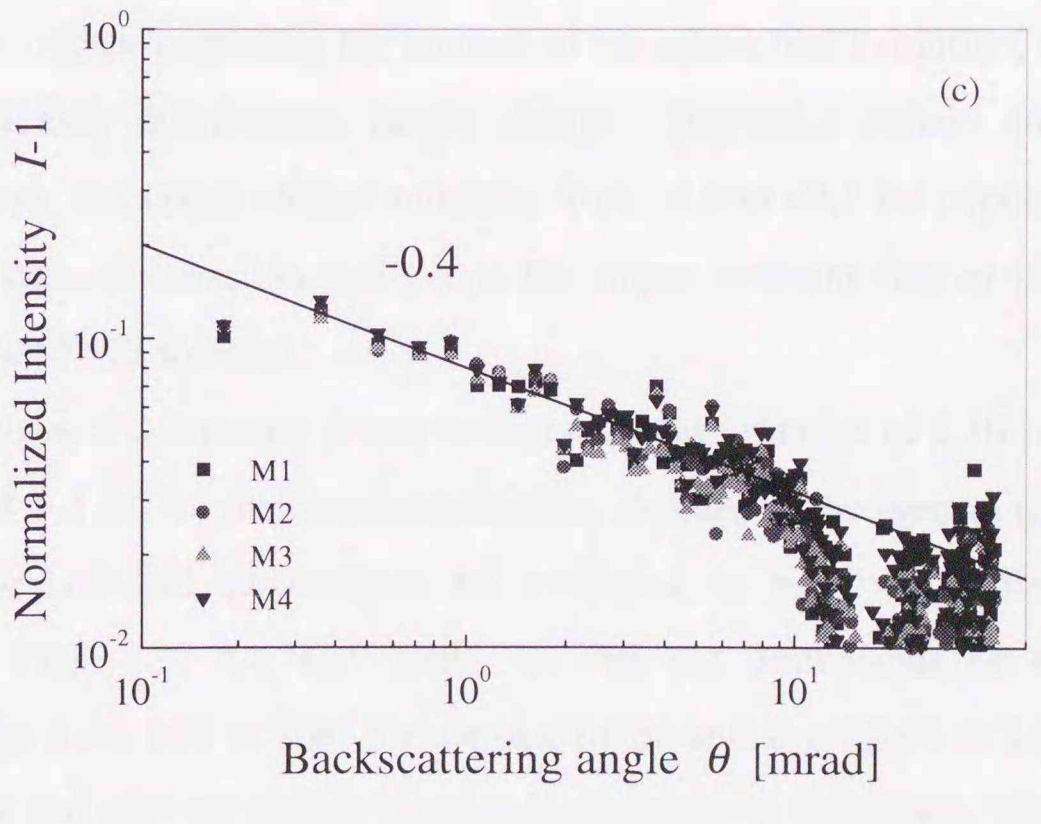
(c)
-0.4
M1
M2
M3
M4
Normalized Intensity I-1
Backscattering angle θ [mrad]

(continued)

7.3 Results and discussion

Figs. 7.3 and 7.4 show the copolarized and cross-polarized intensity distributions of backscattering enhancement produced from the colloidal suspensions of polystyrene latex beads with diameters of (a) 1.0 μm, (b) 0.46 μm, and (c) 0.09μm, respectively. In the figures, M1, M2, M3, M4, M5, and M6 denote six different amounts of added NaCl solutions of 0 ml (■), 0.25 ml (●), 0.5 ml (▲), 0.75 ml (▼), 1.0 ml (◆), and 1.25 ml (✚) to 3 ml colloidal suspension, respectively. The normalized intensity I-1 is plotted as a function of the backscattering angle θ in the logarithmic scale. The solid lines show the decreasing lines corresponding to the peak intensity variation and the attached numbers denote their slopes.

Figs. 7.3 and 7.4 show for (a) 1.0 μm and (b) 0.46 μm that the copolarized and cross-polarized peak intensity distributions produced from M1 decrease with the slopes of −1 and −1.3, respectively. Even increasing the amount of the added NaCl solution, the slopes of the decreasing intensity distributions hardly change. Beyond a certain amount of the added NaCl solution, the slopes change suddenly from −1.0 to −0.8 for copolarization and −1.3 to −0.6 for cross-polarization and keeps the slopes constant further increasing the amount of the added NaCl solution.

By apply the values of decreasing slopes to the empirical formulae of $2.16-1.03D$ for the copolarization and $4-1.8D$ for the cross-polarization obtained in the preceding chapter, the dimensions of the colloidal suspensions are estimated as listed in Table 7.1. It is understood from Figs. 7.3, 7.4, and Table 7.1 that the dimensions of the colloidal suspensions change from 3.07 to 2.87 for copolarization and from 2.94 to 2.56 for cross-polarization before and after the sudden changes in the intensity variations. Therefore, the results obtained for (a) 1.0 μm and (b) 0.46 μm show that: (i) The particles dispersed homogeneously in the 3-D space of the suspension at the beginning: (ii) The depression of the potential barrier due to the electric double layer induces the sudden aggregation of particles by adding the NaCl solution to the colloidal suspension: (iii) The resultant cluster-cluster aggregation hardly grows once the aggregation occurs. Therefore, the analysis of

the peak intensity distribution of the backscattering enhancement can be applied to watching the aggregation process of particles in the dense colloidal suspension.

Figs. 7.3 and 7.4 for (c) 0.09 μm shows the quite different behavior from others. The peak intensity distributions from particles with a diameter of 0.09μm never change and keep the values of sloops to be –0.7 for copolarization and –0.4 for cross-polarization even adding the NaCl solution. From Table 7.1, these values of slopes correspond to the dimensions of 2.78 and 2.44, respectively. This means that the particles with a diameter of 0.09 μm in the suspension aggregated before adding the NaCl solution because such the potential barrier for the small particles is low enough to aggregate.

The physical pictures of the discrepancy between the dimensions estimated from the copolarized and cross-polarized peak intensity distributions should be taken into consideration. The copolarized and cross-polarized peak intensity distributions in the far-field plane are expressed by the 2-D Fourier cosine transform of the intensity distribution $I(x, y)$ emerging from the position (x, y) in the boundary plane between the scattering medium and the air and are given by [123]

$$I_X(k_x, k_y) = \iint I(x, y)\cos(k_x x + k_y y)dxdy \tag{7.1}$$

and

$$I_Y(k_x, k_y) = \iint I(x, y)\Gamma\cos(k_x x + k_y y)dxdy, \tag{7.2}$$

respectively. In the equations, k_x and k_y denote for x- and y-components of a wave vector of the backscattered light, respectively. The correlation Γ between the lights propagating along the time-forward and -reversed paths contributes dominantly to the cross-polarized intensity distribution while it is unity for the copolarized intensity distribution. Whether the correlation factor Γ exists or not causes the discrepancy between the dimensions estimated from the copolarized and cross-polarized intensity distributions. Since the correlation Γ decreases monotonically at every scattering event along the path, only the light propagating inside a cluster close to the incident position forms the cross-polarized peak intensity distribution. On the other hand, the light propagating not only inside but also among the clusters forms dominantly the copolarized

peak intensity distribution. Therefore, the copolarized and cross-polarized peak intensity distributions are affected by the dimensions among the clusters and inside the cluster, respectively. By considering the facts that the dimension inside the cluster is always smaller than 3 and the clusters distribute homogeneously in 3D space of the suspension, the dimension estimated from the copolarized peak intensity distribution is always larger than that from the cross-polarized one.

At the next step, the influence of the absorption in the colloidal suspension to the decreasing behavior of the peak intensity distribution is investigated experimentally. The black ink is added as the absorbent to the colloidal suspension of particles with the diameter of 1.0 μm. Figs. 7.5 and 7.6 show the copolarized and cross-polarized peak intensity distributions of the backscattering enhancement produced (a) before and (b) after the aggregation of particles. In the figures, M1, M2, M3, M4 and, M5 denote six different amounts of the added black ink, 0 μl (■), 10 μl (●), 30μl (▲), 50 μl (▼), and 100 μl (◆), respectively. The solid lines show the decreasing lines corresponding to the peak intensity variations and the attached numbers denote their slopes. It is shown in the figures that both the width and peak intensity of the backscattering enhancement increase consistently with the amount of the added black ink. This comes from the fact that the light propagating along the shorter path contributes dominantly to the formation of the peak intensity distribution as the absorption increases. Especially, the peak intensity for the cross-polarized intensity distribution increases outstandingly from 0.1 to 0.6. On the other hand, the slope of the decreasing peak intensity distribution hardly changes by the increase of the absorption. Therefore, this result shows that the monitoring of aggregation process and the estimation of the dimension for dense colloidal suspension can be performed using enhanced backscattering of light without the degradation of accuracy by the absorption. In addition, the cross-polarized backscattering enhancement becomes worthy to use in the methodology for absorbent colloidal suspension.

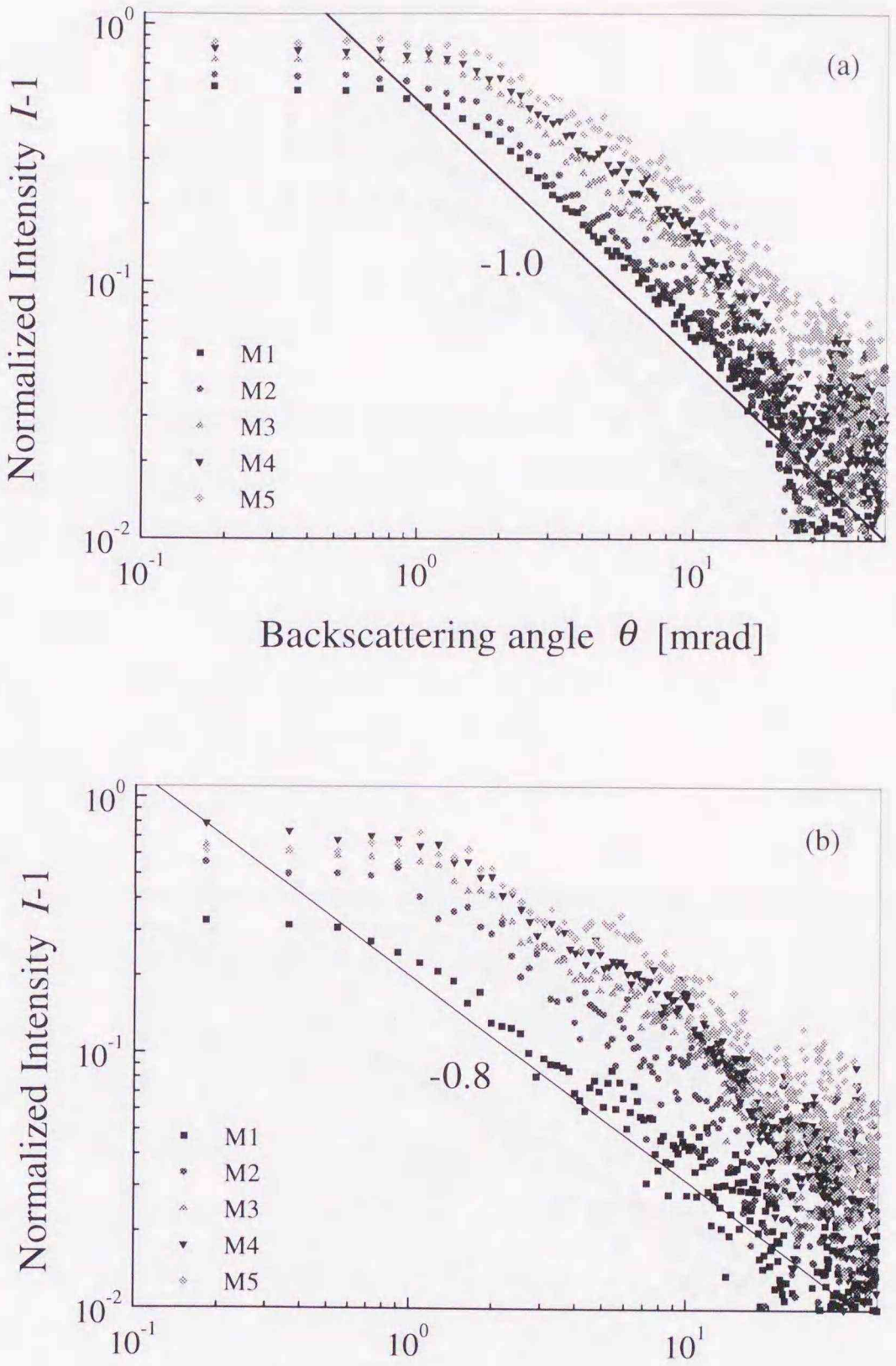

Fig. 7.5 Copolarized peak intensity distributions of the backscattering enhancement produced (a) before and (b) after the aggregation of particles. In the figures, M1, M2, M3, M4 and, M5 denote six different amounts of the added black ink, 0 μl (■), 10 μl (●), 30μl (▲), 50 μl (▼), and 100 μl (◆), respectively. The solid lines show the decreasing lines corresponding to the peak intensity variations and the attached numbers denote their slopes.

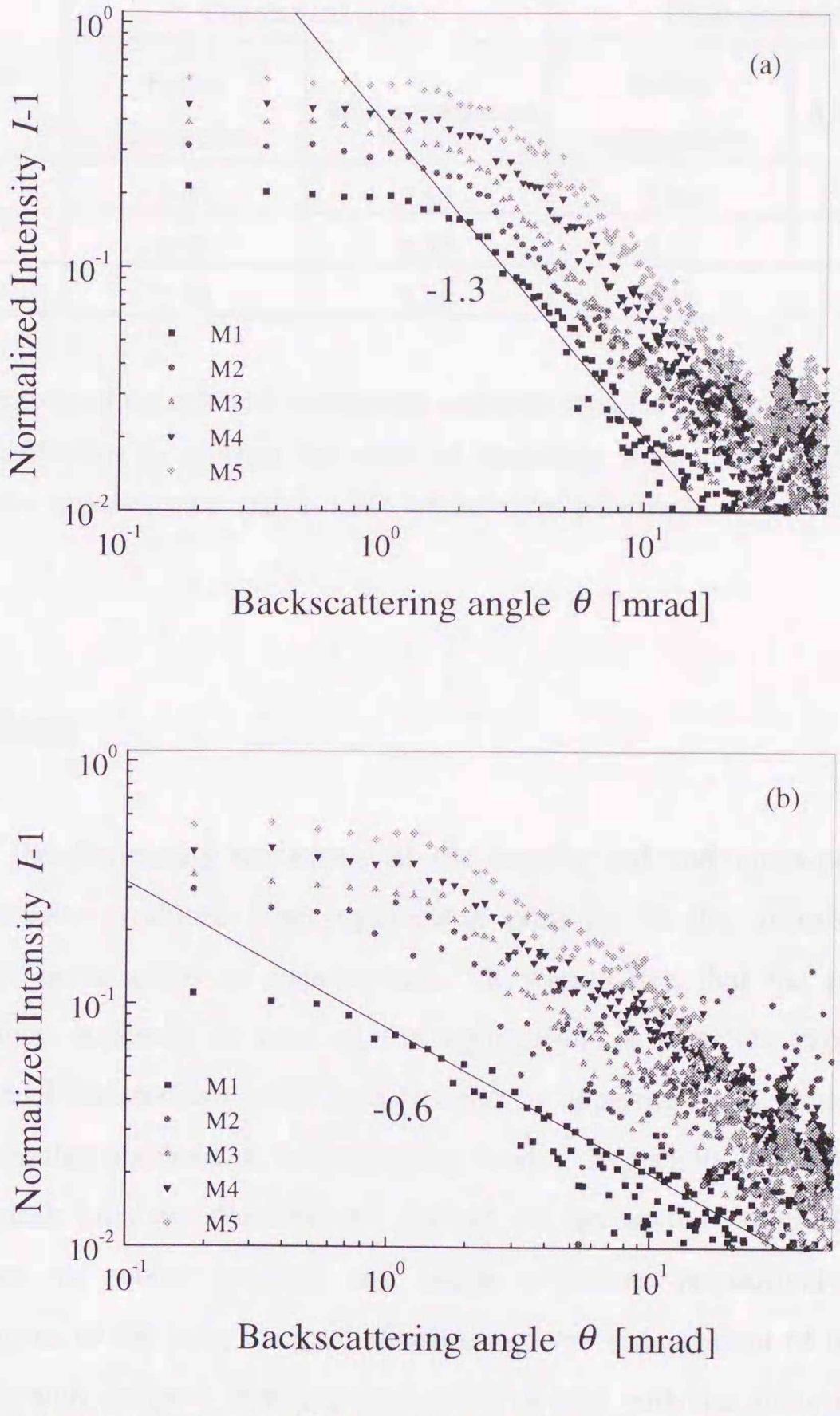

Fig. 7.6 Copolarized peak intensity distributions of the backscattering enhancement produced (a) before and (b) after the aggregation of particles. In the figures, M1, M2, M3, M4 and, M5 denote six different amounts of the added black ink, 0 μl (■), 10 μl (●), 30μl (▲), 50 μl (▼), and 100 μl (◆), respectively. The solid lines show the decreasing lines corresponding to the peak intensity.

Particle size	Copolarized light		Cross-polarized light	
	Before aggregation	After aggregation	Before aggregation	After aggregation
1.0μm	3.07	2.87	2.94	2.56
0.46μm	3.07	2.87	2.94	2.56
0.09μm	2.78	2.78	2.44	2.44

Table 7.1 Dimensions of the colloidal suspensions estimated from the copolarized and cross-polarized peak intensity distributions by applying the values of decreasing slopes to the empirical formulae of $2.16–1.03D$ for the copolarization and $4–1.8D$ for the cross-polarization obtained in the preceding chapter.

7.4 Conclusions

In this chapter, the decreasing variations of the copolarized and cross-polarized peak intensity distributions produced from aggregated particles in the absorbent colloidal suspensions were investigated by experiments. It was shown that the peak intensity distribution changes suddenly as soon as the aggregation of particles happens and the fractal dimension of the medium could be estimated by applying the decreasing slopes to the empirical formulae obtained in the preceding work. Especially, the copolarized and cross-polarized peak intensity distributions depend on the spatial structures of particle distributions over the whole medium and inside a cluster, respectively. Such the decreasing variations of the peak intensity distributions are independent of the absorption of the medium though the peak intensity and width change with the absorption. It was concluded that the analysis on the spatial properties of intensity enhancement phenomenon in the multiple backscattering of light shows the ability to watch the aggregation process of particles and to estimate its dimension for the dense absorbent media. This method has an advantage to apply directly to the dense disordered without any dilution in comparison with the small-angle-scattering method [33,110-112] and second-order-scattering method [113] proposed in the past works.

Chapter 8

Temporal Properties for Fractal Aggregates of Particles under Brownian Motions

8.1 Introduction

A study on the dynamics of internal structures in media such as body, blood, and fluid by using the scattering light is an interesting and important research subject. The temporal autocorrelation functions (TAFs) of light backscattered multiply from homogeneously random media are a powerful tool in this field and known as Diffusive Wave Spectroscopy [73,75,101,125]. As long as the Diffusive Wave Spectroscopy based on the framework of a diffusive transport theory of photons is used, the spatial structure of scattering media is not reflected in the TAFs.

We have recently been interested in optical diagnostics on the dynamics of fractal aggregates of particles using the Diffusive Wave Spectroscopy. To further extend the use of the Diffusive Wave Spectroscopy, the free path-length distribution function was derived theoretically [124] and the spatio-temporal polarization properties of the light intensity backscattered multiply from fractal media were investigated by means of Monte Carlo simulations [122,123,126]. As a result, it is concluded that the spatial and temporal features of light backscattered multiply from the fractal aggregate of particles depend on the fractal dimension of the medium and that the scattering-order distribution function (SODF) and the total path-length distribution function (TPDF) become key functions in the features.

In this chapter, Monte Carlo simulations are conducted to realize numerically the time-varying phenomena of the multiply backscattering light in the fractal aggregate of particles under the Brownian motions. The TAFs of copolarized and cross-polarized components of light backscattered multiply from the fractal aggregate are analyzed numerically on the amplitude basis. Dependency of the TAFs on the fractal dimension and absorption of the

medium and on the backscattering angle is discussed by taking into account the relation between the SODF and the TPDF. It is shown that the fractal property and the absorption of scattering media change a relaxation time and a time shift of the TAFs, respectively.

8.2 Simulations

Monte-Carlo simulations are carried out to trace all scattering events and trajectories of the light backscattered multiply from fractal aggregates of particles. Suppose that an aggregate medium exists in the space of Z>0 in the absolute coordinate system (X,Y,Z) and that the plane light polarized along the X direction is incident onto the medium normally to its boundary plane. The incident light undergoes successive scattering events by many particles, where the scattering angle at the m-th scattering event and the distance between the m-th and (m-1)-th scattering events are denoted by θ_m and r_m, respectively. Finally, the scattering light emerges from the medium in the direction of the backscattering angle θ which is defined as an angle between the direction of the emerging light and the direction opposite to the incident light. The emerging light produces an intensity distribution in a far-field which has an intensity peak referred to as an enhanced backscattering in the direction of retro-reflection. Furthermore, the light varies in time due to the Brownian motions of all scattering particles so that the TAF of the multiply backscattered light monotonically decreases by the accumulative effect of all particle movements.

Concerning with the multiple scattering in the fractal aggregate of particles, the free path-length distribution $p(r)$ plays an important role and is given by [124]

$$p(r_m)=\frac{(D-2)}{\ell_D}\left(\frac{r_m}{\ell_D}\right)^{D-3}\exp\left[-\left(\frac{r_m}{\ell_D}\right)^{D-2}\right], \tag{8.1}$$

in the range of $2.0<D\leqq 3.0$. In Eq.(1), D and ℓ_D denote a fractal dimension and an effective mean free path-length for the fractal aggregate. It is assumed in simulations that the scattering particles are spherical latex beads in water whose size, refractive index and volume fraction are 100nm, 1.59, and 10%, respectively. In this condition, the scattering event at each particle can be approximated by the Rayleigh-Debye scattering [99].

With the assumption that each particle in the medium moves independently of each other due to the Brownian motions even after the particles being aggregated, the TAFs of the multiply scattered light are given by [118]

$$\gamma(\tau,\theta)=\sum_{n=1}^{\infty}p(n,\theta)\left\langle \exp\left(-\frac{4\tau}{\tau_0}\sum_{m=1}^{n}\sin^2\frac{\theta_m}{2}\right)\right\rangle_{\theta_m} . \tag{8.2}$$

In Eq. (8.2), τ and $\tau_0=(D_p k_i^2)^{-1}$ denote a delay time and a single scattering relaxation time in homodyne correlation functions of the time-varying amplitude scattered from particles with the diffusion constant D_p. The TAFs of the multiply backscattered light have an angular dependence which is generated by the interference effect producing the backscattering enhancement. $p(n,\theta)$ denotes a fraction of the intensity emerging in the direction of the backscattering angle θ after a sequence of n scattering events to the total intensity in the same direction.

By taking a polarization effect into consideration, $p_X(n,\theta)$ and $p_Y(n,\theta)$ for copolarized and cross-polarized components of the backscattered light are defined by

$$p_X(n,\theta)=\langle I_{nX}\rangle_{ex}\Big/\sum_{n=1}^{\infty}\langle I_{nX}\rangle_{ex} \tag{8.3a}$$

and

$$p_Y(n,\theta)=\langle I_{nY}\rangle_{ex}\Big/\sum_{n=2}^{\infty}\langle I_{nY}\rangle_{ex}, \tag{8.3b}$$

respectively. $\langle I_{nX}\rangle_{ex}$ and $\langle I_{nY}\rangle_{ex}$ denote the n-th order scattering intensity distributions for the copolarized and cross-polarized components and are numerically calculated by using the data obtained in Monte Carlo simulations [118]. By substituting Eq. (8.3) into Eq. (8.2), the angular dependence of the time-varying light backscattered multiply from the fractal aggregate of particles can be investigated numerically and quantitatively.

8.3 Results and discussion

Figures 8.1 (a) and (b) show the TAFs of the copolarized and cross-polarized light amplitude backscattered multiply from the fractal aggregates of particles with the dimensions of D=2.5, 2.8 and 3.0. In the figures, the black circles stand for the relaxation

times τ_c which are estimated to be $\tau_c = 2/A^2$ by fitting the TAFs to $\exp(-A\sqrt{\tau})$. The TAFs show various features depending on the polarization and the aggregation of particles: the TAFs become wider with a decrease of the dimension, a magnitude in the variations of the TAFs becomes more outstanding with an increase of the delay time, and a magnitude in the variations of the TAFs for the copolarized component is larger than that for the cross-polarized one.

Furthermore, we discuss the properties of TAFs by quoting the two types of TAFs expressed by discrete and continuous definitions for homogeneously random media. The first type of TAFs in a discrete definition is expressed as a summation of the decay function $\exp\left(-\tau n/2\tau_0 n^*\right)$ weighted by the SODF $p(n)$ in a range of the scattering order from a single to infinity and is given by

$$\gamma(\tau) = \sum_{n=1}^{\infty} p(n)\exp\left(-\tau n/\tau_0 n^*\right), \tag{8.4}$$

where n^* denotes the averaged scattering order where the directions of light propagating in the medium are fully randomized. On the other hand, the second type of TAFs in a continuous definition is expressed as an integration of the decay function $\exp\left(-\tau s/\tau_0 \ell^*\right)$ weighted by the TPDF $p(s)$ in a range of the total path-length from zero to infinity and is given by

$$\gamma(\tau) = \int_0^{\infty} p(s)\exp\left(-\tau s/\tau_0 \ell^*\right), \tag{8.5}$$

where the transport mean free path-length ℓ^* denotes the averaged path-length where the directions of light propagating in the medium are fully randomized, and s is the total path-length of trajectories of the scattering light with the n-th scattering order. For homogeneously random media, Eq. (8.4) becomes equivalent to Eq. (8.5) because of $p(s) = p(n\ell)$. It should be noticed in the derivation of Eq. (8.5) that the lower limit of the integration was assumed to be reduced from ℓ^* to zero. However, this assumption will break down whenever the light with the path-length shorter than ℓ^* contributes dominantly to the autocorrelation function of the backscattered light. Nevertheless, the Laplace transform relation of Eq. (8.5) between the autocorrelation function and the TPDF has been fairly well confirmed in experiments for the multiple light scattering [73,75,76,101,104,127].

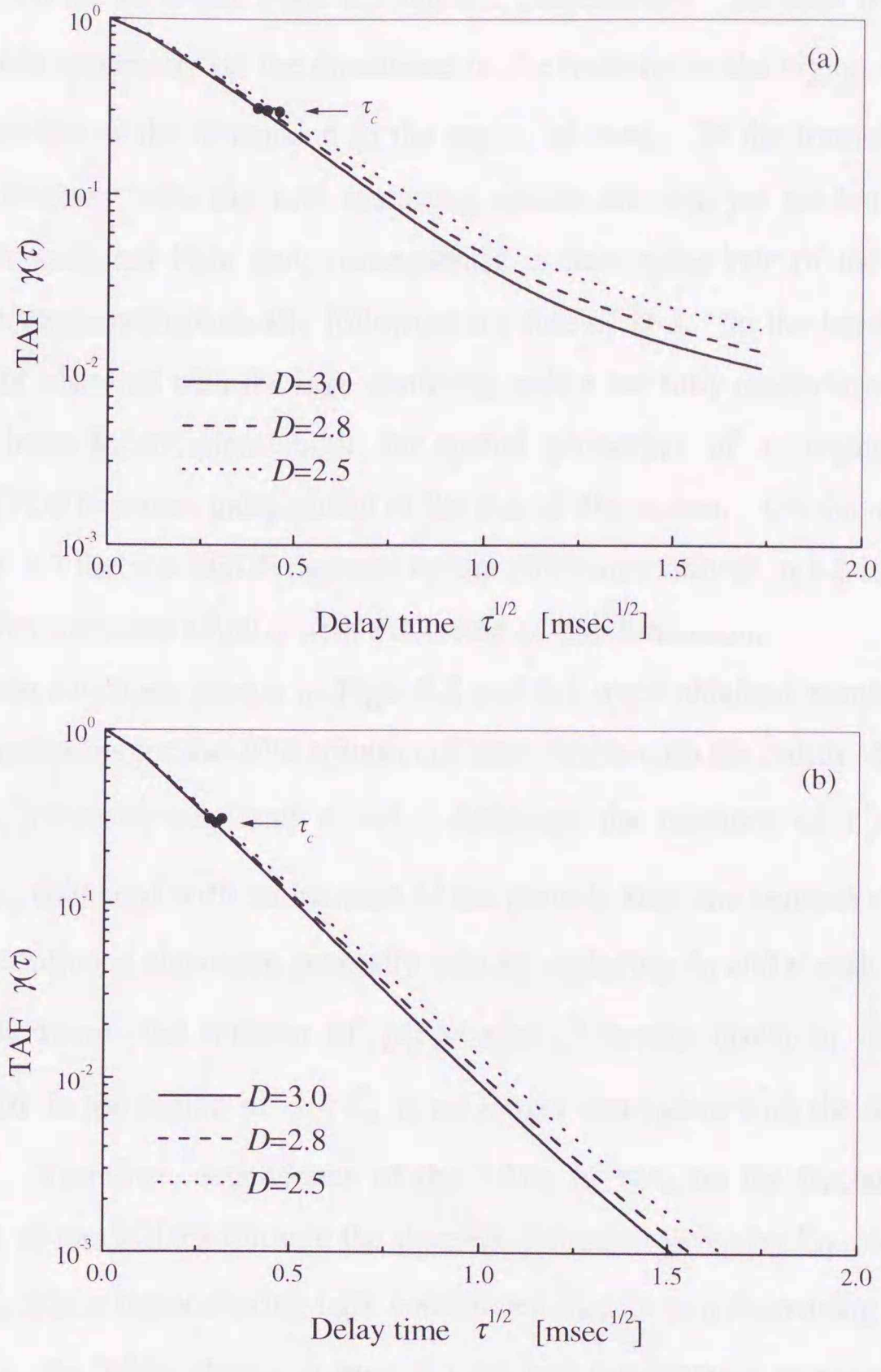

Fig. 8.1 Temporal autocorrelation functions (TAF) of (a) the copolarized and (b) the cross-polarized components of light scattered multiply from the three different media with the dimensions of D=2.5, 2.8, and 3.0 in the direction of retroreflection. The vertical and horizontal axes denote a logarithm of the TAFs and a square root of the delay time, respectively. The black circles stand for the relaxation times τ_c which were estimated to be $\tau_c = 2/A^2$ by fitting the TAFs to $\exp(-A\sqrt{\tau})$.

The TPDFs and the SODFs of light backscattered multiply from the fractal media with D=2.5, 2.8 and 3.0 are shown in Figs. 8.2 and 8.3, respectively. As seen from Fig. 8.2, the TPDF depends apparently on the dimension of the medium in the region of $s<\ell_D$, and becomes independent of the dimension in the region of $s>\ell_D$. In the former region, the dominant contributions with the low scattering orders are not yet randomized in the directions of the scattered light and, consequently, a decreasing rate of the TPDF in a logarithmic plot varies asymptotically following the line of D-3. In the latter region, the directions of light scattered with the high scattering orders are fully randomized so that the scattered light loses information about the spatial properties of aggregated particles. Therefore, the TPDF becomes independent of the fractal dimension. On the other hand, it is seen from Fig. 8.3 that the SODF depends on the dimension only at $n \approx 1$ in such a way that the probability increases slightly with a decrease of the dimension.

The distribution functions shown in Figs. 8.2 and 8.3 were obtained numerically from Monte Carlo simulations for the 10% solution of latex beads with the radius of 100nm, for which $\ell_D^* = \ell_D / \langle 1-\cos\theta \rangle \approx \ell_D$ and $n^* \approx 1$. Although the relations of $\ell_D^* >> \ell_D$ and $n^* >> 1$ are more enhanced with an increase of the particle size, the features of the TPDF and the SODF mentioned above are generally held by replacing ℓ_D and n with ℓ_D^* and n^*, respectively. However, the relation of $p(s) = p(n\ell_D)$ breaks down in fractal media because the TPDF in the region of $s < \ell_D^*$ is no longer equivalent with the SODF in the region of $n<n^*$. Therefore, dependence of the TAFs in $\tau>\tau_c$ on the fractal dimension comes from that of the SODFs through the discrete definition given by Eq. (8.4). In the region of $s > \ell_D^*$ where the scattering light contributes mainly to a decreasing behavior of the TAFs in $\tau<\tau_c$, the TAFs shown in Figs. 8.1 (a) and (b) decrease in accordance with $\exp(-A\sqrt{\tau})$. Therefore, the Laplace transform relation still holds between the TAFs and the TPDFs.

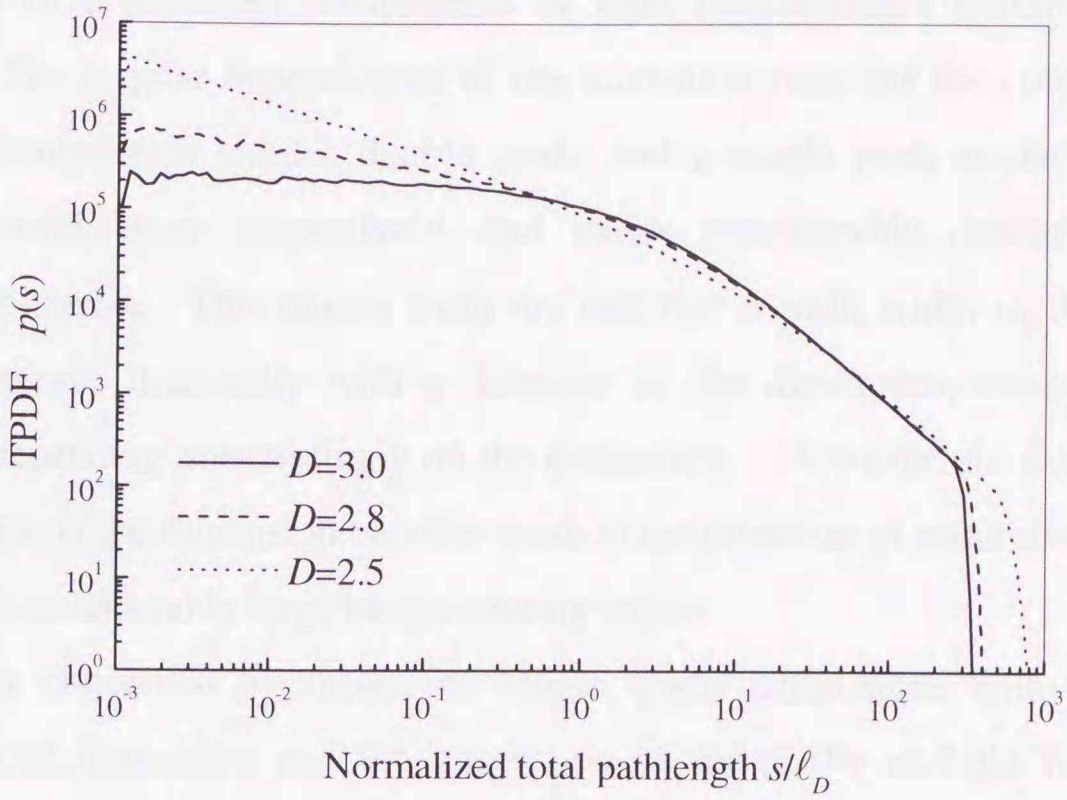

Fig. 8.2 Total path-length distribution functions (TPDF) of light backscattered multiply from the three different media with the dimensions of D=2.5, 2.8, and 3.0, where the horizontal axis is normalized by the effective mean free path-length ℓ_D. In the figure, both the horizontal and vertical axes are plotted in a logarithmic scale.

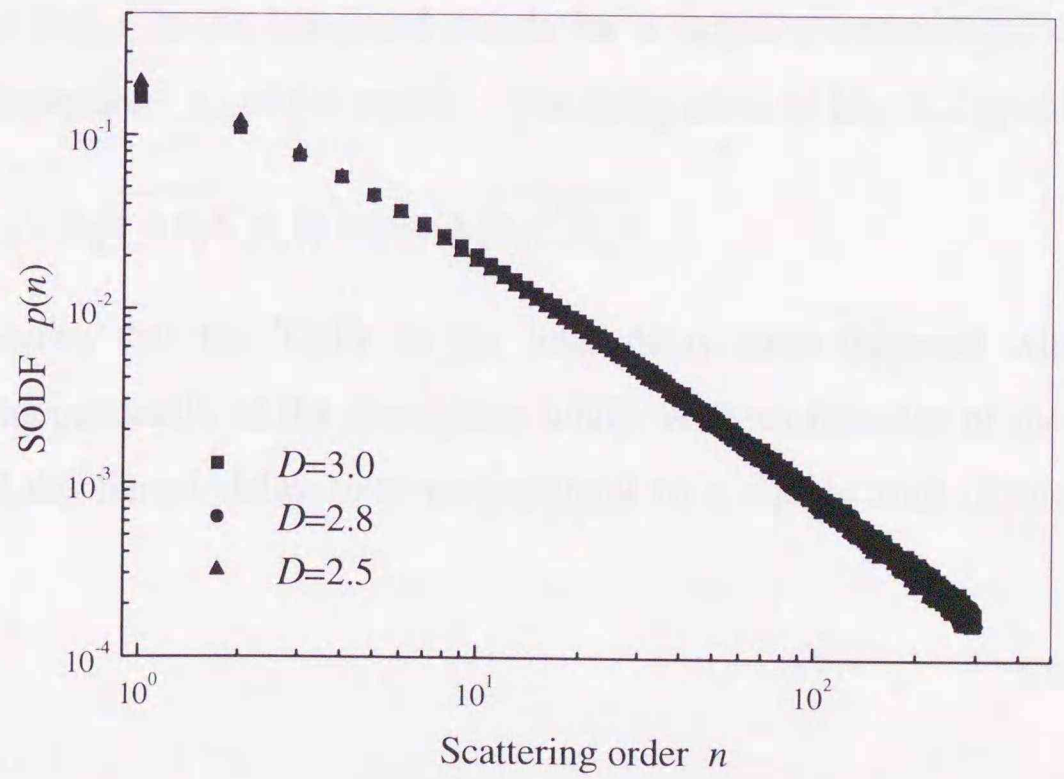

Fig. 8.3 Scattering-order distribution functions (SODF) of light backscattered multiply from the three different media with the dimensions of D=2.5, 2.8, and 3.0. In the figure, the vertical axis is plotted in a logarithmic scale.

Figures 8.4 (a) and (b) show the angular dependences of the relaxation time for the copolarized and cross-polarized components of light backscattered multiply from the fractal media. The angular dependences of the relaxation time for the copolarized and cross-polarized components exhibit double peaks and a single peak around and in the direction of retroreflection, respectively, and varies considerably depending on the dimension of the media. This comes from the fact that a peak width of the enhanced backscattering spreads drastically with a decrease of the dimension, consequently the relaxation time depending outstandingly on the dimension. However, the dependence of the relaxation time on the dimension become weak in the direction of retroreflection and in the direction with considerably large backscattering angles.

We are finally concerned by means of Monte Carlo simulations with the relation between the fractal dimension and the absorption in the TAFs of light backscattered multiply from fractal media. The case of homogeneously random media is discussed for reference before studying the case of fractal media. The TAFs of the multiply backscattered light from homogeneously random media are expressed by [128]

$$\gamma(\tau)=\int_0^\infty p(s)\exp(-\mu_a s)\exp\left(-\tau s/\tau_0\ell^*\right)ds\,, \tag{8.6}$$

where the second factor in the integrand stands for a negative-exponential decay of the light due to the absorption μ_a of the media. The integration of Eq. (8.6) yields

$$\gamma(\tau)=\exp(-A\sqrt{\tau+\tau_0\ell^*\mu_a})\Big/\exp(-A\sqrt{\tau_0\ell^*\mu_a})\,. \tag{8.7}$$

Equation (8.7) shows that the TAFs in the long delay time decrease with the same decreasing rate independently of the absorption while, with an increase of the absorption, they shift toward the longer delay time proportional to a square root of the absorption coefficient.

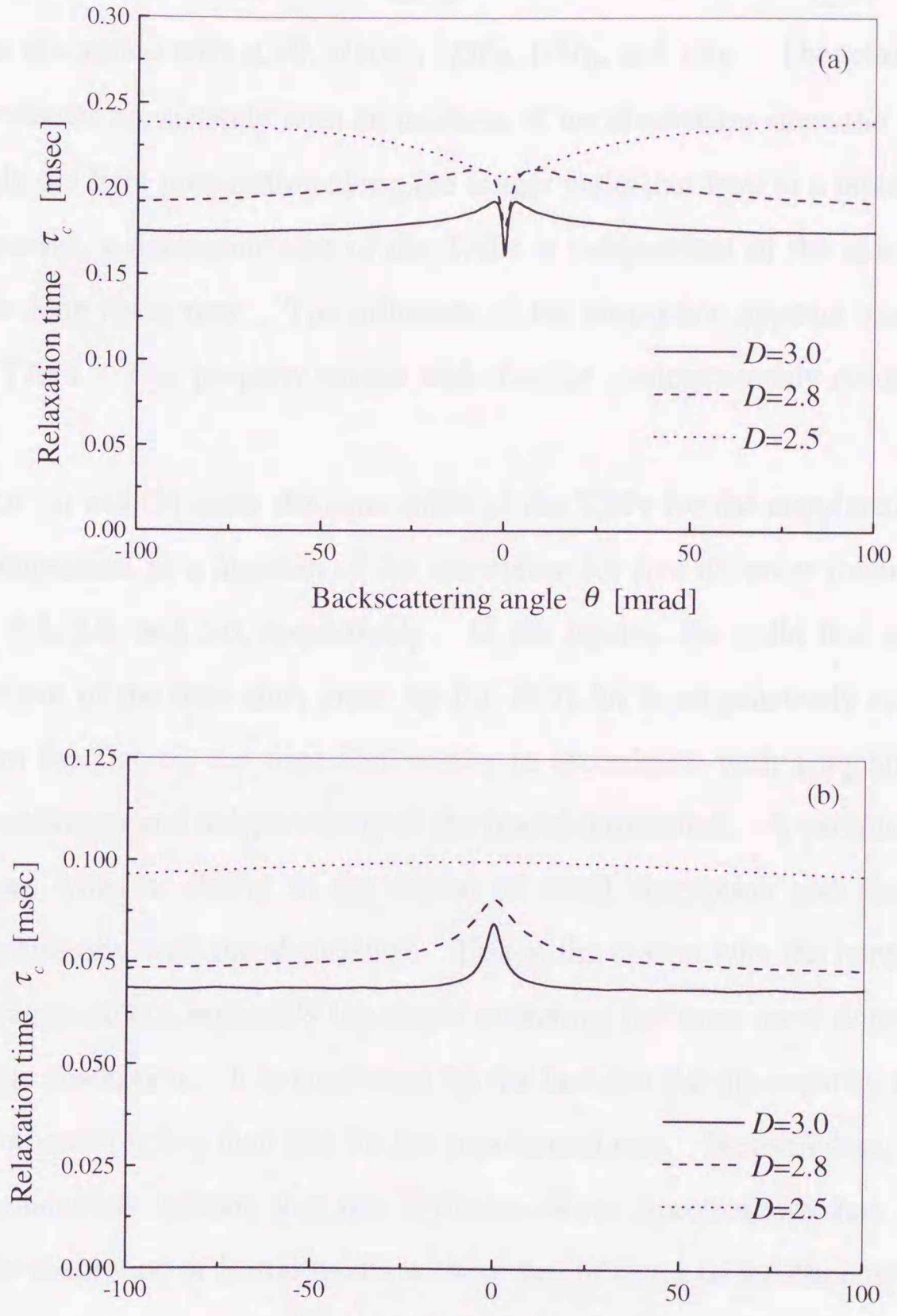

Fig. 8.4 Angular dependence of the relaxation time of (a) the copolarized and (b) the cross-polarized components of light backscattered multiply from the three different media with the dimensions of D=2.5, 2.8, and 3.0. The relaxation time is estimated to be $\tau_c = 2/A^2$ by fitting the TAF to $\exp(-A\sqrt{\tau})$.

Figures 8.5 (a) and (b) show the TAFs for the copolarized and cross-polarized components from the absorbent fractal aggregates of particles with D=2.8 for five different values of the absorption with μ_a=0, 1/10ℓ_D, 1/5ℓ_D, 1/3ℓ_D, and 1/ℓ_D. The relaxation time of the TAFs increases consistently with an increase of the absorption since the media absorb more strongly the light propagating along the longer paths that lead to a rapid decay of the TAFs. However, a decreasing rate of the TAFs is independent of the absorption in the region of the long delay time. The influence of the absorption appears only in the time shift of the TAFs. This property agrees with that for homogeneously random absorbent media.

Figures 8.6 (a) and (b) show the time shifts of the TAFs for the copolarized and cross-polarized components as a function of the absorption for five different fractal media with D=2.5, 2.6, 2.7, 2.8, and 3.0, respectively. In the figures, the solid line stands for the theoretical curve of the time shift given by Eq. (8.7) for homogeneously random media. As seen from the figures, the time shift varies in accordance with a square root of the absorption coefficient and independently of the fractal dimension. A variation of the time shift coincides with the theory in the region of small absorption and the discrepancy increases consistently with the absorption. This is the reason why the contribution with the low scattering orders, especially the single scattering, becomes more dominant with an increase of the absorption. It is confirmed by the fact that the discrepancy for the cross-polarized component is less than that for the copolarized one. Nevertheless, the results in numerical simulations indicate that the Diffusive Wave Spectroscopy has an ability of measuring the absorption of fractal media without the influence of the dimension.

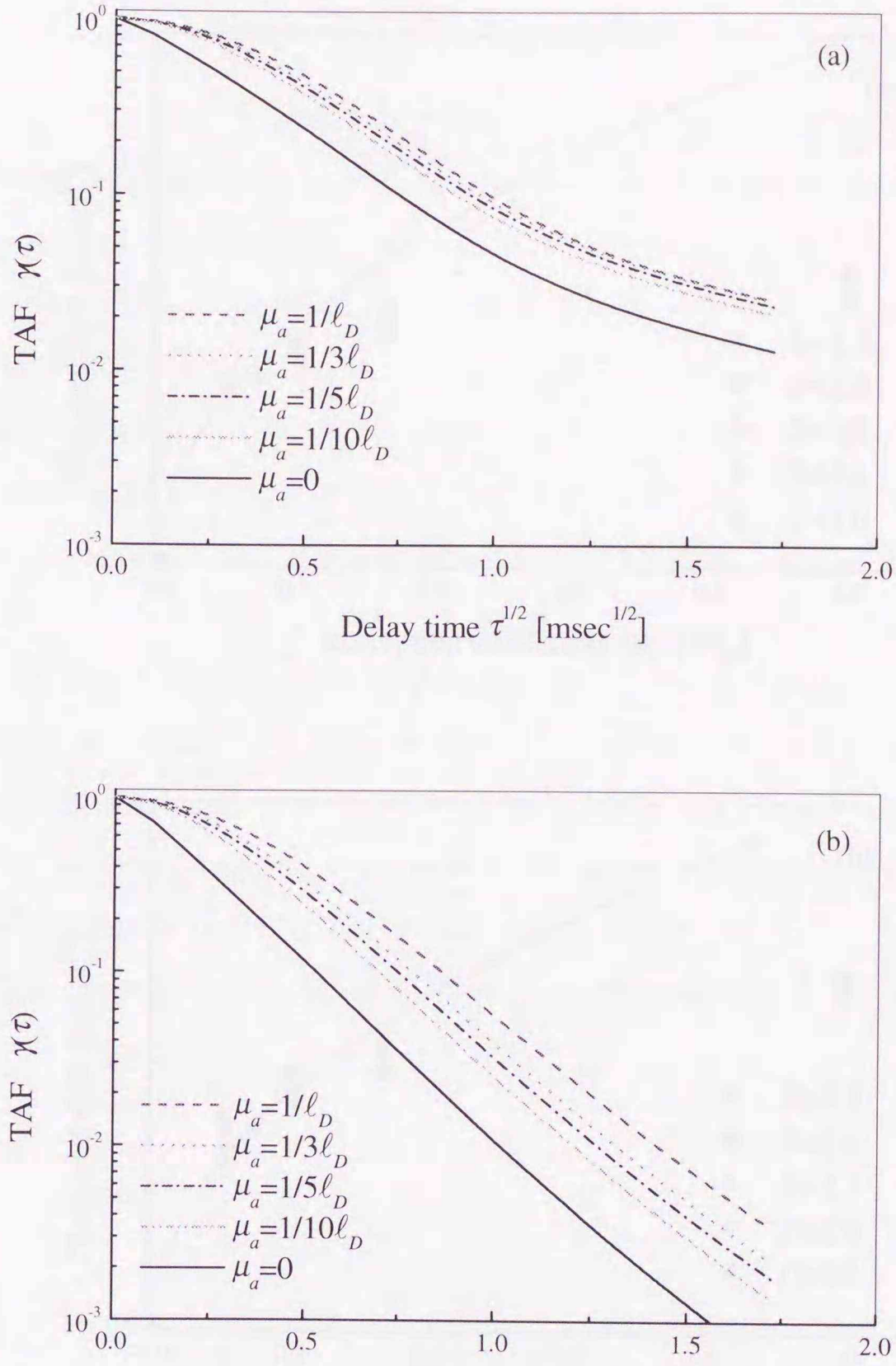

Fig. 8.5 Temporal autocorrelation functions (TAF) of (a) the copolarized and (b) the cross-polarized components of light scattered multiply in the direction of retroreflection from the five different absorbent media of μ_a=0, $1/10\ell_D$, $1/5\ell_D$, $1/3\ell_D$, and $1/\ell_D$ with the dimension of D=2.8. The vertical and horizontal axes denote a logarithm of the TAFs and a square root of the delay time, respectively.

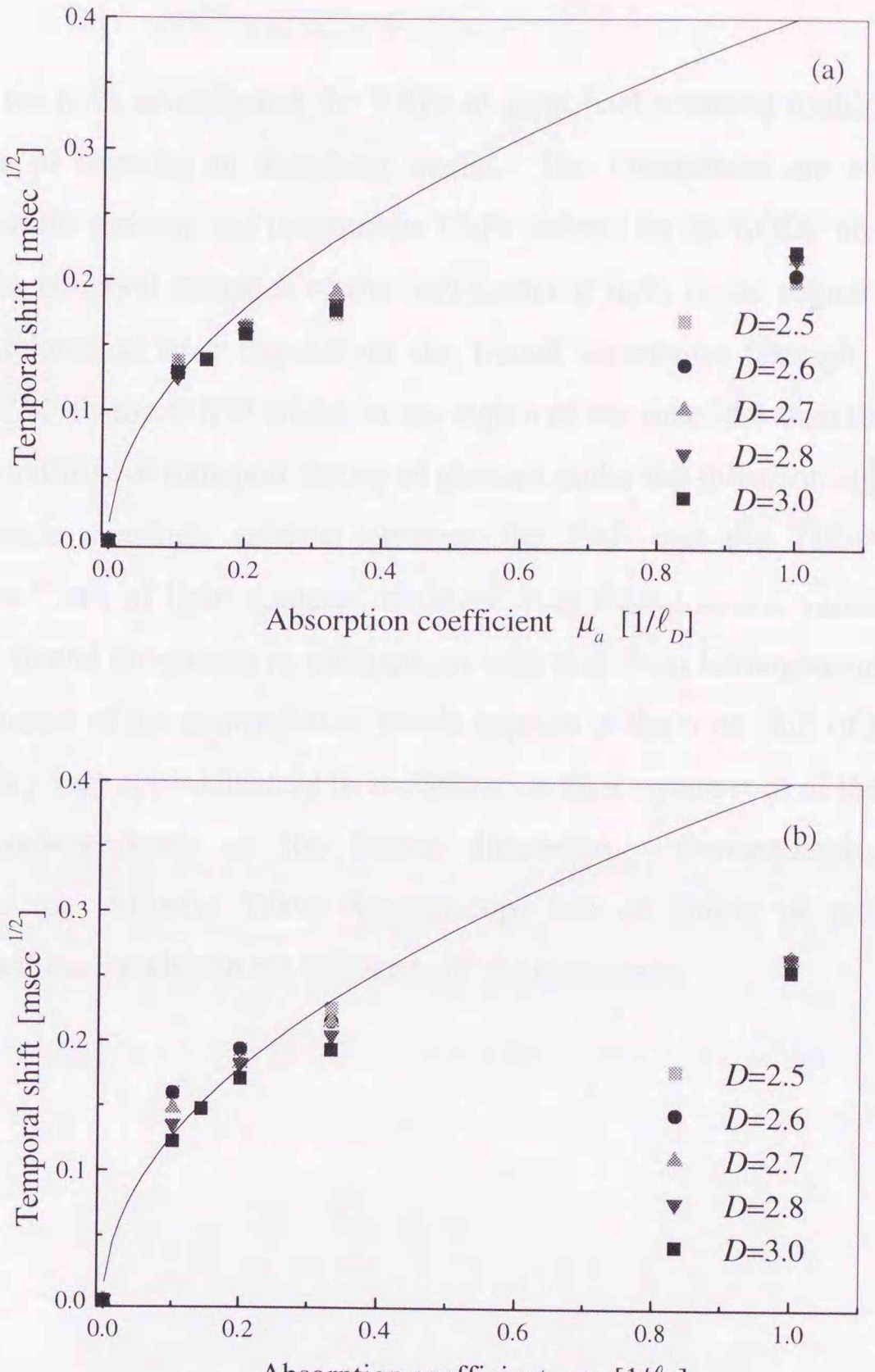

Fig. 8.6 Time shifts of the TAFs of (a) the copolarized and (b) the cross-polarized components of light backscattered multiply from the five different absorbent media with the dimensions of D=2.5, 2.6, 2.7, 2.8, and 3.0. The horizontal axis denotes the absorption coefficient normalized by the effective mean free path-length ℓ_D.

8.4 Conclusions

In this chapter , we have investigated the TAFs of light backscattered multiply from the fractal aggregates of particles in absorbent media. The discussions are conducted by taking into account the discrete and continuous TAFs defined by the SODF and the TPDF, respectively. The temporal statistics of the backscattered light in the region of the time longer than the relaxation time depend on the fractal dimension through the discrete definition of the TAF by the SODF while, in the region of the time less than the relaxation time, they follow a diffusive transport theory of photons under the diffusion approximation through the Laplace transform relation between the TAF and the TPDF. Angular dependence of the TAFs of light scattered multiply from fractal media varies drastically depending on the fractal dimension in comparison with that from homogeneously random media. The influence of the absorption of media appears in the time shift of the TAFs in such a way that they vary approximately in accordance with a square root of the absorption coefficient and independently of the fractal dimension. Consequently, we have demonstrated that the Diffusive Wave Spectroscopy has an ability of measuring the absorption of fractal media without the influence of the dimension.

Chapter 9

Coherent Backscattering of Light from Polydisperse Media

9.1 Introduction

The aggregation of particles is an interesting phenomenon in physics, chemistry biophysics. The acquired knowledge is useful for understanding the dynamics of internal complex structures in blood fluids, biomedical tissues, chemical compounds, particle aggregations and so on [129]. The light scattering methods such as a small-angle-scattering method [33,110-112] and a second-order-scattering method [113] have been widely used in analyzing the spatial structure of particle aggregations. By increasing the fraction of the solution in a dense scattering medium, these measuring methods no longer can be used due to an effect of the multiple scattering. Therefore, we have concentrated our attention to the spatio-temporal properties of the light backscattered multiply from a fractal aggregate of the particles [122,123,126]. Due to the difficulty in controlling experimentally the dimension of

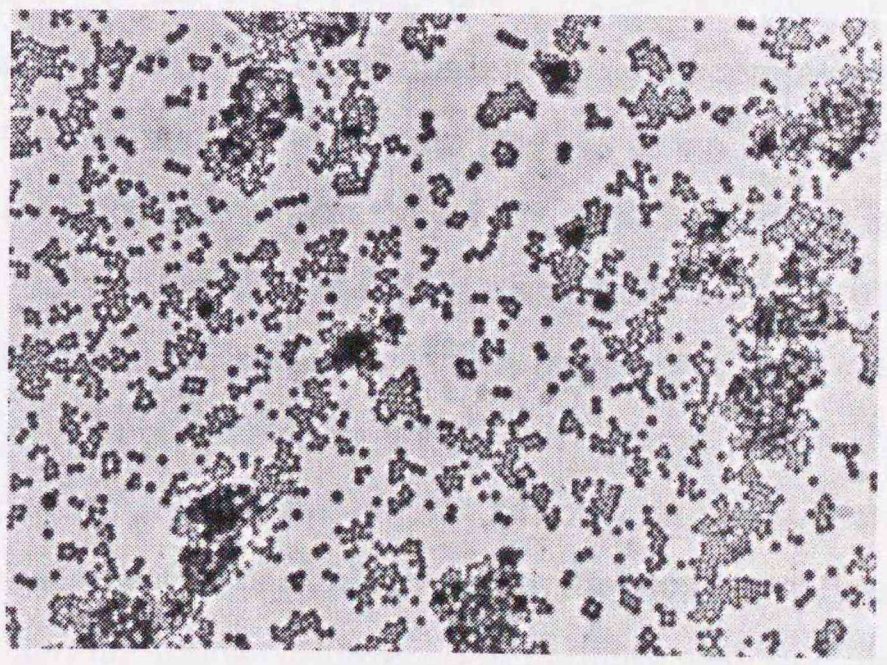

Fig. 9.1 Cluster-cluster aggregation of polystyrene latex beads with the radius of 1μm.

scattering media, the systematic studies have been done by means of Monte Carlo simulations. In simulations, the activation-limited aggregation was assumed, in which each particle in the aggregation can move independently because the particles do not contact with each other. The activation-limited aggregation leads to a change of the path-length distribution function but not any change of the diffusion constant. It is therefore shown that an enhancement in the copolarized backscattering intensity decreases in accordance with $\theta^{2.16-1.03D}$ due to the free path-length distribution function depending on the fractal dimension D of the scattering media and that the temporal autocorrelation functions of the time-varying intensity hardly vary with a variation of the dimension [123].

By developing the aggregation of particles, many clusters become to be distributed in the solvent of the fractal medium shown in Fig. 9.1. The aggregation of this type is called a cluster-cluster aggregation, in which the particles stick on contact with each other so that each cluster behaves as a large single particle. The light backscattered multiply from the cluster-cluster aggregation consists of the lights scattered inside the cluster with extremely short path-lengths and from the clusters with extremely long path-lengths. In the present chapter, we showed in experiments that the light scattering inside a single cluster rather than the light scattered from the distributed clusters contributes dominantly to a formation of the copolarized intensity distribution, consequently a decaying rate of the intensity depending on the fractal dimension of the single cluster. Due to a change of the diffusion constant for the cluster-cluster aggregation, the relaxation time of temporal autocorrelation functions increases with the growth of clusters. Therefore, we expect an applicability of the temporal autocorrelation functions of the light backscattered multiply from the cluster-cluster aggregation to measurements of the averaged cluster size under comparison with a variation of the relaxation time for a monodisperse random medium as a function of the particle size.

The Monte Carlo simulations are conducted for the intensity enhancement and temporal autocorrelation function of the copolarized light backscattered multiply from cluster-cluster aggregations. It is known that the cluster size distribution of cluster-cluster aggregations follows a power law distribution function which is a typical function of the stationary distribution with the self-similarity. Therefore, the simulations are carried out for the power law distribution function, the Gaussian distribution function as a limiting case of the stationary distribution, and the simple summation of particles with two different radii as an

example of the homogeneously random medium. Consequently, we confirm an applicability of the temporal autocorrelation functions to measurements of the cluster size.

9.2 Numerical simulations

9.2.1 Numerical tracings of photon trajectories

The Monte Carlo simulations are conducted by tracing all scattering events and paths in a scattering medium [99]. Figure 9.2 shows two different Cartesian coordinate systems for the absolute coordinates $(\mathrm{X},\mathrm{Y},\mathrm{Z})$ and the m-th scattering coordinates $(\mathrm{x}_m,\mathrm{y}_m,\mathrm{z}_m)$. The incident and backscattering lights are specified by the absolute coordinate system whose origin and Z and X axes are defined by the incident position of light, and the directions of the incident wavevector $\boldsymbol{k}_i$ and the polarization $\boldsymbol{P}_i$, respectively. The scattering coordinate system is defined at each scattering event so that its origin, z_m and x_m axes for the m-th scattering coordinate system are defined by the position of the m-th scattering particle, the directions of the wavevector $\boldsymbol{k}_{m-1}$ and the polarization $\boldsymbol{P}_{m-1}$ of the $(m-1)$-th scattered light, respectively. The light with the wavevector $\boldsymbol{k}_i$ enters the medium, undergoes successive scattering events which generate the scattered light with the wave vectors $\boldsymbol{k}_1,\boldsymbol{k}_2,\cdots,\boldsymbol{k}_{n-1}$ and

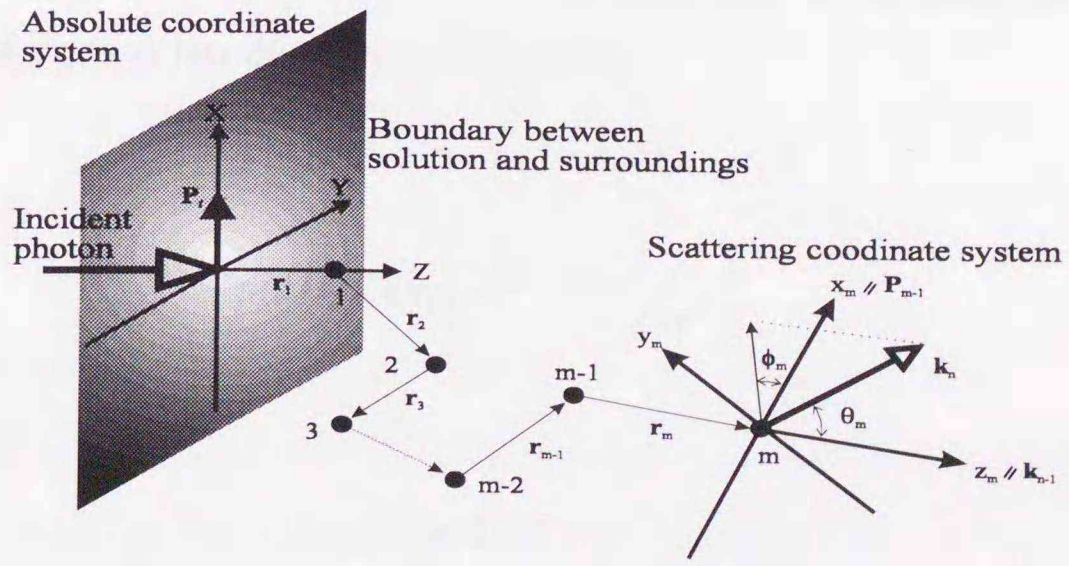

Fig. 9.2 Absolute and scattering coordinate systems used in Monte Carlo simulations.

the scattering angles $\theta_1,\theta_2,\cdots,\theta_{n-1}$ from $n-1$ particles located at $\boldsymbol{r}_1,\boldsymbol{r}_2,\cdots,\boldsymbol{r}_{n-1}$, and leaves from the medium at the location of $\boldsymbol{r}_n$ with the wave vector $\boldsymbol{k}_n$ and the backscattering angle θ_n. It is assumed in this study that the backscattered light is detected on the line parallel to the X axis at $Y=0$ in the far-field plane, consequently the backscattering angle θ being defined as an angle between the directions of the n-th scattered light and the –Z axis of the absolute coordinate system.

9.2.2 Particle size distributions for a cluster-cluster aggregation

As shown in Fig.9.1, the aggregation of particles generates a distribution of the clusters with various sizes rather than a single cluster in the process of the practical growth. Therefore, an analysis of the cluster-cluster aggregation of particles is a quite interesting research subject. In the single cluster, the fractal dimension denotes the static and geometrical features of the particle distribution, which reflects the spatio-temporal features of the multiply backscattering light as studied by means of the Monte Carlo simulations. Since there exist many clusters with the various sizes in the space for cluster-cluster aggregations, the numerical simulations for all the light propagations and scatterings in each cluster consume computing time and seem to be impossible from the practical point of view. Therefore, the cluster size distribution function is renormalized to the particle size distribution function in a polydisperse system. The simulations are conducted by using the three different particle size distribution functions of a simple summation of particles with two different radii, a Gaussian distribution, and a power law distribution defined by

$$p(a)=A_1\delta(a-a_1)+A_2\delta(a-a_2), \tag{9.1a}$$

$$p(a)=C\exp\left[-(a-a_m)^2/\sigma^2\right], \tag{9.1b}$$

and

$$p(a)=Ca^{-\alpha}, \tag{9.1c}$$

respectively. In simulations, a size of the scattering particle is generated by using the

transformation method as random variables following the size distribution functions of Eq. (9.1).

In the cluster-cluster aggregation, the cluster may be naturally regarded as a fractal with the finite size. For the random variables following a stationary distribution function [130], an appropriate linear transformation makes a sum of the random variables obey the same distribution. This can be regarded as a kind of self-similarity. Therefore, the clusters in the cluster-cluster aggregation are assumed to be distributed in size following the stationary distribution. The Gaussian distribution function given by Eq. (9.1c) is the best-known distribution possessing this property. As a matter of fact, the Gaussian distribution function is a limiting case of the stationary distribution. The stationary distribution generally shows a tail following the power law. This fact gives the basis for an application of the power law distribution of Eq. (8.1c) as a cluster size distribution [131].

9.2.3 Free path-length distribution function

In simulations, the distance vector $r_m = |\boldsymbol{r}_m|$ between the successive scattering events statistically follows a negative-exponential probability density function as

$$p(r_m) = \exp(-r_m/\ell_e)/\ell_e \tag{9.2}$$

where $\ell_e = 1/\sum_i \rho_i Q_i$ denotes the effective mean free path-length in the polydisperse random medium, ρ_i and Q_i standing for the number density and the scattering efficiency for particles with different sizes, respectively. The random number r_m following the negative-exponential probability density function of Eq. (9.1) is generated by means of the transformation method [109].

The Rayleigh-Debye scattering is assumed at the scattering event depending on the size and the shape of scattering particles. The zenith angle θ_m and the azimuth angle ϕ_m of the scattered direction at the m-th scattering particle obey probability density functions given by the phase functions [108];

$$p(\theta_m) \propto (\sin q_m a - q_m \cos q_m a)^2 / q_m^6 a^6 \tag{9.3}$$

and

$$p(\phi_m) \propto \sin^2 \theta_m \sin^2 \phi_m + \cos^2 \phi_m , \tag{9.4}$$

respectively, where a denotes the radius of scattering particles. In simulations, the zenith angle θ_m at the m-th scattering event is firstly determined by random number which is distributed by following Eq. (9.3) in the range of [0, π]. The azimuth angle ϕ_m is secondly determined for a given zenith angle θ_m by a random number which is distributed by following Eq. (9.4) in the range of [0, 2π].

In the Rayleigh-Debye scattering theory, the linearly polarized incident light gives rise to the linearly polarized light scattered by a particle, whose polarization is decided by the polarization of the incident light and the wave vector of the scattered light. When the light with the linear polarization $\boldsymbol{P}_{m-1}$ is incident into the m th particle and when the scattered light with the wave vector $\boldsymbol{k}_m$ is generated, the polarization $\boldsymbol{P}_m$ of the scattered light is given by

$$\boldsymbol{P}_m = -\boldsymbol{k}_m \times (\boldsymbol{k}_m \times \boldsymbol{P}_{m-1}) \equiv S(\boldsymbol{k}_m)\boldsymbol{P}_{m-1} . \tag{9.5}$$

There exist the scattered waves propagating along a path from the 1st particle to the n th one and in the reverse order. Their polarizations are expressed by

$$\boldsymbol{P}_{nf} = \prod_{m=1}^{n} S(\boldsymbol{k}_m)\boldsymbol{P}_i \equiv S_{nf}\boldsymbol{P}_i \quad . \tag{9.6a}$$

and

$$\boldsymbol{P}_{nr} = \prod_{m=n}^{1} S(\boldsymbol{k}_m)\boldsymbol{P}_i \equiv S_{nr}\boldsymbol{P}_i , \tag{9.6b}$$

respectively, where $S_{nr} = S_{nf}^t$, S^t being a transpose of S . In Eq. (9.6), the subscripts, f and r, denote the time-forward and -reversed components of light, respectively, Since the time-reversal waves given by Eq. (9.6) are coherent with each other, the constructive interference between them produces an intensity enhancement phenomenon in the backscattering from a

highly disordered medium. In a simple case of the incident light with the wave vector $\boldsymbol{k}_i = (0,0,1)$ and the polarization $\boldsymbol{P}_i = (1,0,0)$, the amplitude components of the scattered lights propagating along time-forward and -reversed paths are given by

$$\boldsymbol{P}_{nf} = (S_{nXX}, S_{nYX}, S_{nZX}) \tag{9.7a}$$

and

$$\boldsymbol{P}_{nr} = (S_{nXX}, S_{nXY}, S_{nXZ}), \tag{9.7b}$$

respectively, where S_{nUV} denotes an amplitude component whose polarization is transformed from the positive-V direction to the positive-U direction after propagating along a path of n scattering events.

9.2.4 Coherent backscattering of light

It is assumed that the intensity is detected by changing the detecting position on the X axis of the observation plane, consequently the intensity distribution as a function of the backscattering angle being obtained. In addition, the copolarized component of the light intensity scattered along the path with the nth scattering order is observed through an analyzer placed in parallel with direction of the polarization of light incident onto the medium. Under such a consideration, the copolarized component of the scattered light is formulated as [99]

$$I_{nX\bar{X}} = \frac{I_{nXf} + I_{nXr}}{I_f}(1 + \Gamma_{nX}\cos\Phi_n). \tag{9.8}$$

where $\Phi_n \approx k\theta X$ denotes the phase difference due to the distance X between the incident and exit points. Since the subscript X denotes the copolarized component, the two intensities of I_{nXf} and I_{nXr} are obtained by

$$I_{nXf} = (S_{XX}\cos\theta + S_{ZX}\sin\theta)^2, \tag{9.9a}$$

and

$$I_{nXr} = \left(S_{XX}\cos\theta + S_{XZ}\sin\theta\right)^2, \tag{9.9b}$$

respectively, and the total intensity propagating in the forward direction is defined by

$$I_f = S_{nXX}^2 + S_{nYX}^2 . \tag{9.9c}$$

Furthermore, Γ_{nX} indicates a degree of the correlation between the waves propagating in time-forward and -reversed directions in the copolarized component and is defined as

$$\Gamma_{nX} = \frac{\sqrt{I_{nXf} I_{nXr}}}{I_{nXf} + I_{nXr}}. \tag{9.10}$$

9.2.5 Temporal autocorrelation functions

The statistical properties of a time-varying amplitude $E(\tau,\theta)$ scattered multiply in the direction of the backscattering angle θ from the disordered medium are described by a temporal autocorrelation function as [118]

$$\Gamma(\tau,\theta) = \left\langle E(\tau,\theta)E^*(0,\theta)\right\rangle = \sum_{n=1}^{\infty}\left\langle \left|E_n(0,\theta)\right|^2\right\rangle_{ex}\left\langle \prod_{m=1}^{n}\exp[i\boldsymbol{q}_m\cdot\Delta\boldsymbol{r}_m(\tau)]\right\rangle_{\boldsymbol{q},\Delta\boldsymbol{r}}, \tag{9.11}$$

where $\boldsymbol{q}_m = \boldsymbol{k}_m - \boldsymbol{k}_{m-1}$ and $\Delta\boldsymbol{r}_m(\tau) = \boldsymbol{r}_m(\tau) - \boldsymbol{r}_m(0)$ denote the scattering vector at the mth scattering event and the displacement of the mth particle motion in time τ, respectively. $E_n(0,\theta)$ is a contribution of the amplitude scattered along a path of n scattering events to the total scattered field, and $\langle\cdots\rangle_{ex}$ stands for the ensemble average over the distribution of the exit positions from the medium. The second term of Eq. (9.11) is a contribution of the total phase change due to the displacement of all n scattering particles, $\langle\cdots\rangle_{\boldsymbol{q},\Delta\boldsymbol{r}}$ standing for the ensemble average over both the distributions of the scattering vector $\boldsymbol{q}_m$ and the particle displacement $\Delta\boldsymbol{r}_m(\tau)$. By assuming that the displacements of all particles are produced by Brownian motions, $\Delta\boldsymbol{r}_m(\tau)$ obeys the zero-mean Gaussian statistics. Therefore, the ensemble average of the second term with respect to the displacement $\Delta\boldsymbol{r}_m(\tau)$ yields

$$\Gamma(\tau,\theta)=\sum_{n=1}^{\infty}\left\langle\left|E_n(0,\theta)\right|^2\right\rangle_{ex}\left\langle\exp\left(-\frac{4\tau}{\tau_0}\sum_{m=1}^{n}\sin^2\frac{\theta_m}{2}\right)\right\rangle_q, \tag{9.12}$$

where $\tau_0=\left(D_p k_i^2\right)^{-1}$ is an order of the single scattering relaxation time in a homodyne autocorrelation function and $q_m=2k_i\sin\theta_m/2$ has been used in the derivation, D_p standing for the diffusion constant of particles depending on the particle size and the notations of $q_m=|\boldsymbol{q}_m|$ and $k_i=|\boldsymbol{k}_i|=|\boldsymbol{k}_m|$ being used. Furthermore in Eq. (9.12), the ensemble average of the second term may be reduced to that over the distribution of the scattering angle at each scattering event. To investigate the dependence of the temporal autocorrelation function on the backscattering angle θ, the normalized autocorrelation function is finally obtained as

$$\gamma(\tau,\theta)=\frac{\Gamma(\tau,\theta)}{\Gamma(0,\theta)}=\sum_{n=1}^{\infty}p(n,\theta)\left\langle\exp\left(-\frac{4\tau}{\tau_0}\sum_{m=1}^{n}\sin^2\frac{\theta_m}{2}\right)\right\rangle_{\theta_m}, \tag{9.13}$$

where $p(n,\theta)$ denotes a fraction of the total intensity leaving in the direction of the backscattering angle θ after scattering along a path of n scattering events and is defined by

$$p(n,\theta)=\left\langle\left|E_n(0,\theta)\right|^2\right\rangle_{ex}\Big/\sum_{n=1}^{\infty}\left\langle\left|E_n(0,\theta)\right|^2\right\rangle_{ex}=\left\langle I_{nX\bar{X}}\right\rangle_{ex}\Big/\sum_{n=1}^{\infty}\left\langle I_{nX\bar{X}}\right\rangle_{ex}. \tag{9.14}$$

At this stage, two ensemble averages, $\left\langle\exp\left(-4\tau/\tau_0\sum_{m=1}^{n}\sin^2\theta_m/2\right)\right\rangle_{\theta_m}$ and $\left\langle\left|E_n(0,\theta)\right|^2\right\rangle_{ex}$, in Eq. (9.13) together with Eq. (9.14) over the distributions of the scattering angle at each scattering event and the exit position from the medium remain without any further formulations. They are evaluated by using the results of Monte Carlo simulations on coherent multiple backscatterings. In simulations, we obtain the scattering order n, all the scattering angles $\theta_m\ (m=1,\cdots,n)$ at all scattering events, the coordinates $(\mathrm{X},\mathrm{Y},\mathrm{Z})$ of the position where the wave leaves from the medium, and the nth order amplitudes of the scattering wave, $\boldsymbol{P}_{nf}$ and $\boldsymbol{P}_{nr}$, for the incidence of a single photon. By changing a seed of the random generator, 10^6 data for a given scattering order n were obtained, from which the

ensemble-averaged $\left\langle \exp\left(-4\tau/\tau_0 \sum_{m=1}^{n} \sin^2 \theta_m / 2 \right) \right\rangle_{\theta_m}$ and the copolarized intensity $\left\langle I_{nX\bar{X}} \right\rangle_{ex}$ are obtained. The normalized autocorrelation functions of the time-varying light on the amplitude basis backscattered multiply from the dense disordered medium are finally evaluated for the copolarized component by substituting Eq. (9.8) into Eq. (9.14).

9.3 Results and discussion

In the proceeding studies, the simulations in the simple summation of particles were conducted for the volume fractions, (10%, 0%), (5%, 5%) and (0%, 10%), of the particles with two different radii of a_1=100nm and a_2=200nm, which correspond to (A_1, A_2)=(1, 0), (0.17, 0.83) and (0, 1) in the coefficients in Eq. (9.1a), respectively. The simulations in Gaussian and the power law distributions of Eqs. (9.1b) and (9.1c) were conducted for the standard deviations of σ=10, 25, 50 and 75nm around the mean particle size of a_m=150nm and for the exponents of α=1, 2 and 3, respectively. Figures 3 and 4 show the intensity enhancements and the temporal autocorrelation functions of the light backscattered multiply from the cluster-cluster aggregations obtained from Eqs. (9.8) and (9.13) for three different cluster size distribution functions of (a) the simple summation of particles of Eq. (9.1a), (b) the Gaussian distribution of Eq. (9.1b), and (c) the power law distribution of Eq. (9.1c). In Fig. 9.3, the vertical and horizontal axes denote the coherent component of the intensity enhancement and the backscattering angle, respectively, which are plotted in a logarithmic scale. On the other hand, the vertical and horizontal axes in Fig. 9.4 denote the temporal autocorrelation function plotted in a logarithmic scale and the delayed time plotted in a linear scale, respectively.

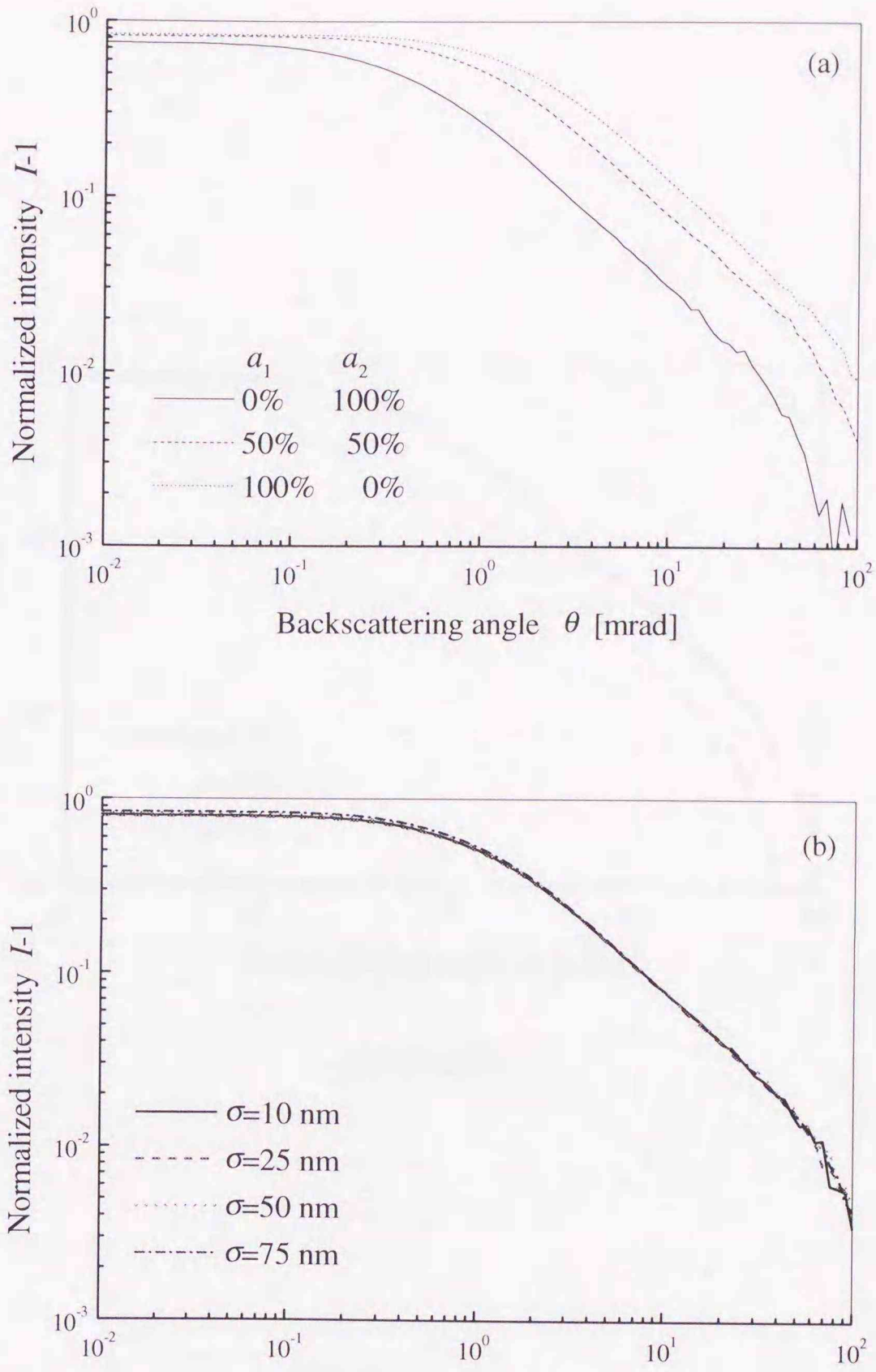

Fig. 9.3 Intensity enhancements of the light backscattered multiply from the random media which are distributed by following (a) the simple summation of particles with the radii of a_1=100nm and a_2=200nm, (b) the Gaussian distribution with the mean size of 150nm and the standard deviation of σ, and (c) the power law distribution with the exponent α.

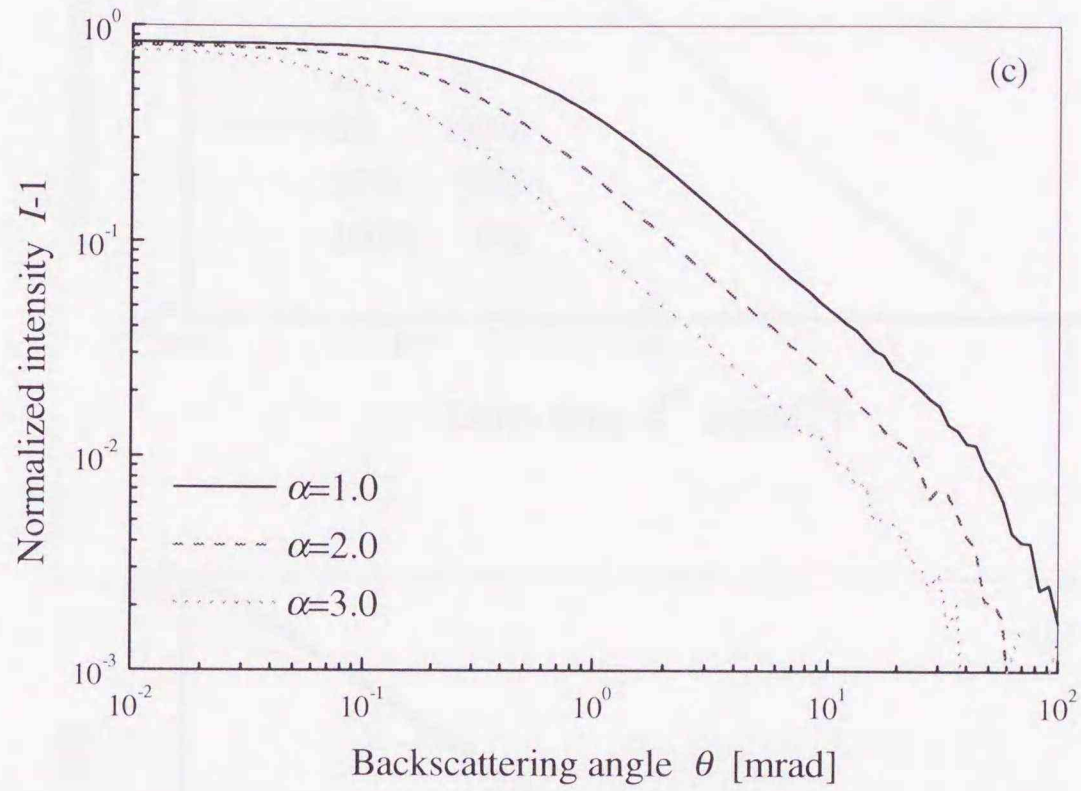
(c)
Normalized intensity I-1
Backscattering angle θ [mrad]
α=1.0
α=2.0
α=3.0
10^0
10^-1
10^-2
10^-3
10^-2
10^-1
10^0
10^1
10^2

(continued)

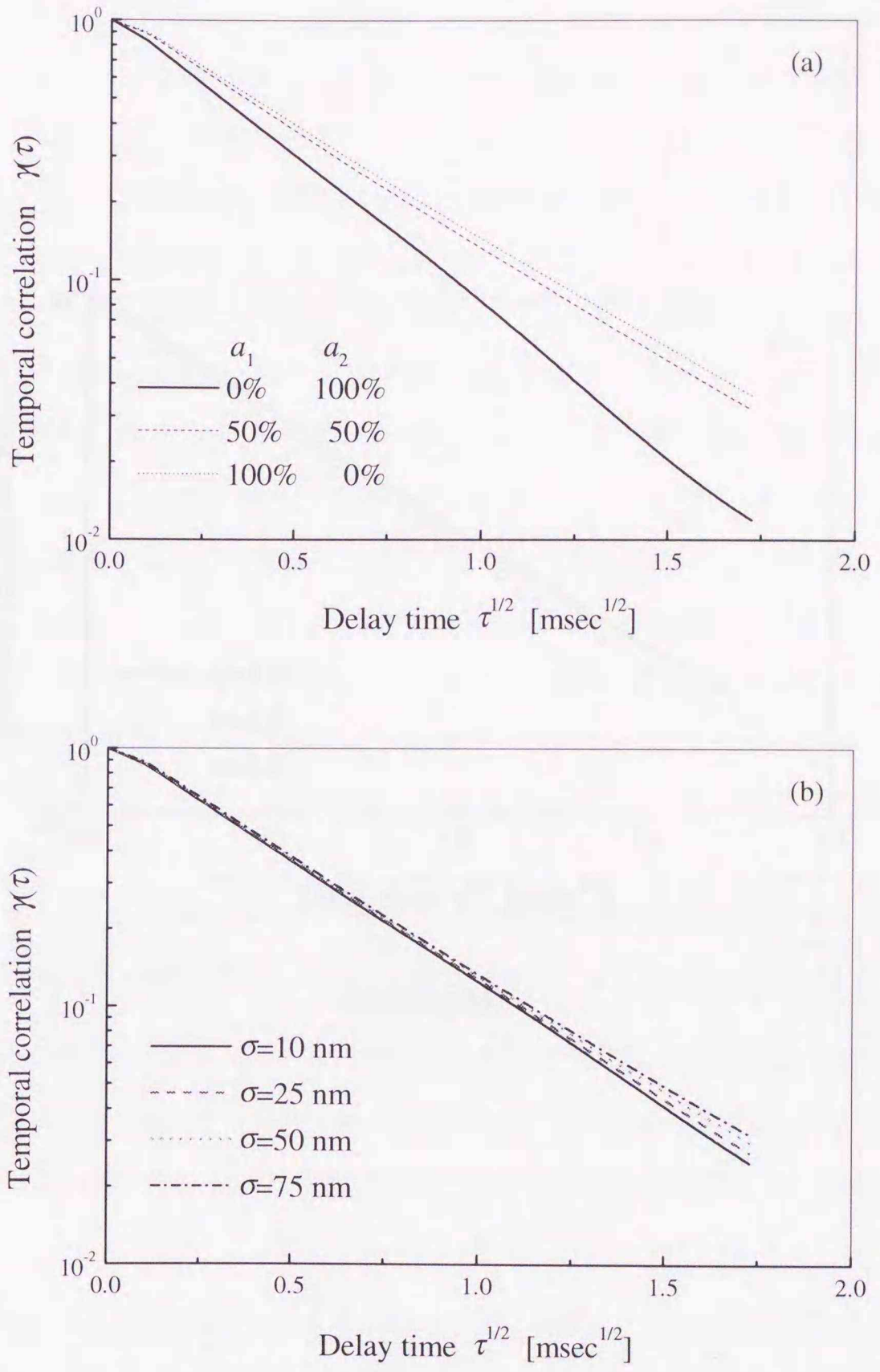

Fig. 9.4 Temporal autocorrelation functions of the light backscattered multiply from the random media which are distributed following (a) the simple summation of particles with the radii of a_1=100nm and a_2=200nm, (b) the Gaussian distribution with the mean size of 150nm and the standard deviation of σ, and (c) the power law distribution with the exponent α.

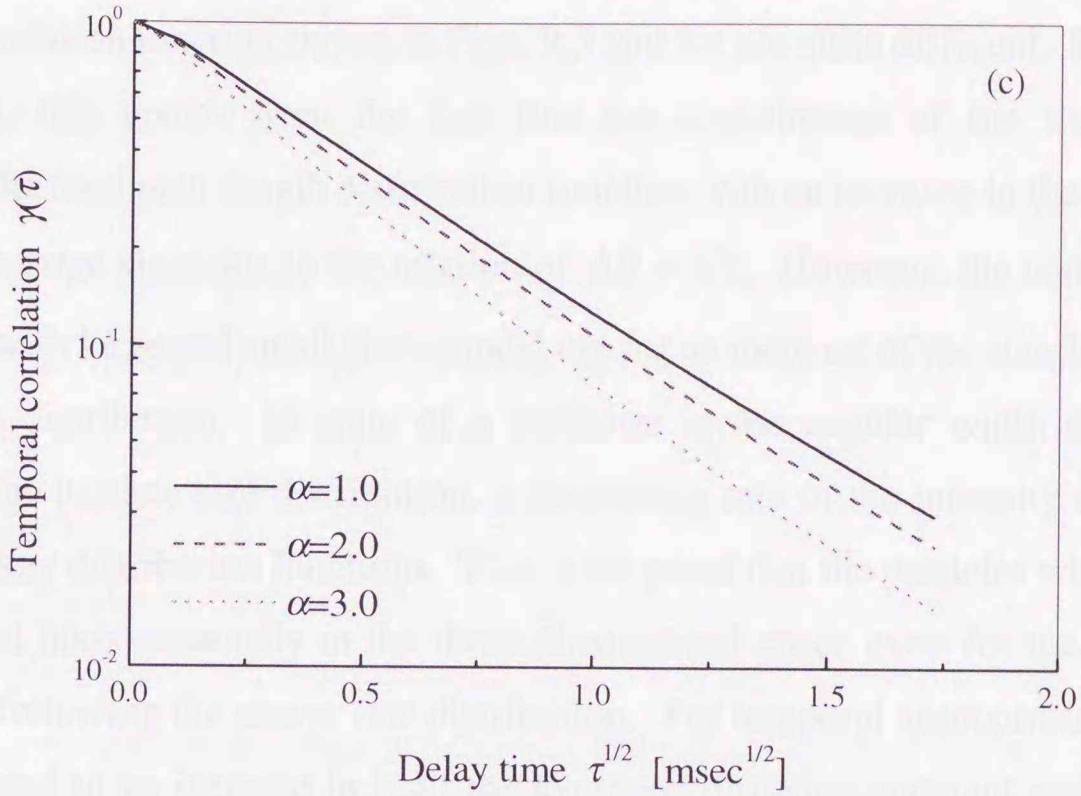
(c)
10^0
10^{-1}
10^{-2}
Temporal correlation $\mathcal{H}(\tau)$
α=1.0
α=2.0
α=3.0
0.0
0.5
1.0
1.5
2.0
Delay time $\tau^{1/2}$ [msec$^{1/2}$]

(continued)

The intensity enhancement and the temporal autocorrelation function spread wider with an increase in the contribution of the light scattered by the particles with larger sizes for the simple summation of particles and the power law distribution, while they are independent of an increase of the standard deviation for the Gaussian distribution. The larger particle size makes the intensity enhancement and the temporal autocorrelation function widen and vice versa. However, the mechanism for both variations of the intensity enhancement and the temporal correlation function shown in Figs. 9.3 and 9.4 are quite different. For the intensity enhancement, this comes from the fact that the contribution of the short path-length increases in the total path-length distribution function with an increase in the contribution of particles with large sizes due to the relation of $\Delta\theta \propto 1/\ell$. However, the contributions from the particles with large and small sizes cancel out for an increase of the standard deviation in the Gaussian distribution. In spite of a variation in the angular width depending on a variation of the particle size distribution, a decreasing rate of the intensity enhancement is invariant for any distribution functions. This is the proof that the particles with various sizes are distributed homogeneously in the three-dimensional space even for the distribution of the particles following the power law distribution. For temporal autocorrelation functions, this is attributed to an increase in both the averaged diffusion constant and the scattering probability with an increase of the particle size because of the relation $\tau_c \propto D_p/\ell$. The temporal correlation functions follow $\exp\left(-A\sqrt{\tau}\right)$ which is derived under the diffusion approximation since they decay proportionally to a square root of the delay time as shown in Fig. 9.4. Therefore, the relaxation time can be estimated by fitting the numerical data to $\exp\left(-A\sqrt{\tau}\right)$.

To estimate the averaged cluster size for three different distributions given by Eq. (9.1) by using the multiple backscattering light from the cluster-cluster aggregation, the angular width of the intensity enhancement and the relaxation time obtained from the numerical results of Figs. 9.3 and 9.4 are renormalized to those for the monodisperse random media. As a function of the particle size, Fig. 9.5 shows the variations in the angular width of the intensity enhancement and the relaxation time of temporal autocorrelation functions of the light backscattered multiply from the monodisperse random media. The angular width and the relaxation time are obtained from the intensity enhancement and the temporal

autocorrelation function of the time-varying light backscattered multiply from the cluster-cluster aggregation of particles, with which the averaged cluster size is finally estimated from comparison of the angular width and relaxation time for the monodisperse random medium.

Figure 9.6 shows the averaged cluster sizes estimated from the angular width and the relaxation time of the time-varying light backscattered multiply from the polydisperse random media with the particle sizes following (a) the simple summation of particles, (b) the Gaussian distribution, and (c) the power law distribution. In the figures for (a) the simple summation and (b) the power law distribution, the horizontal axis stands for the particle size and the thin solid lines denote $f(a)=a$. For (b) the Gaussian distribution, the horizontal axis stands for the standard deviation and the dotted line denotes $f(a)=150nm$. As shown in the figures, the averaged sizes estimated from the angular widths of the intensity enhancements coincide with the lines of $f(a)=a$ and $f(a)=150nm$ so that the averaged size of particles in the polydisperse random medium seems to be estimated exactly by means of the renormalization to the monodisperse case. However, this result is supported only for the homogeneously random medium with the dimension of D=3 but not for the cluster-cluster aggregation of particles because of the dominant contribution of the light scattered inside the cluster as mentioned previously. On the other hand, the averaged sizes estimated from the relaxation times of temporal autocorrelation functions deviates toward a larger value from the line of $f(a)=a$ and even from $f(a)=150nm$ for the case of the Gaussian distribution. This ensures us that the relaxation time of temporal autocorrelation functions is proportional to a product of the diffusion constant and the reciprocal of the mean free path-length rather than the total path-length distribution function of the backscattering light. It is also shown that the larger diffusion constant plays a more significant role than the smaller one. If the particle size in the three-dimensional random medium is regarded as the standard value in the estimation of the averaged cluster size in cluster-cluster aggregations, the averaged size needs to be compensated to reduce the effect of the large clusters.

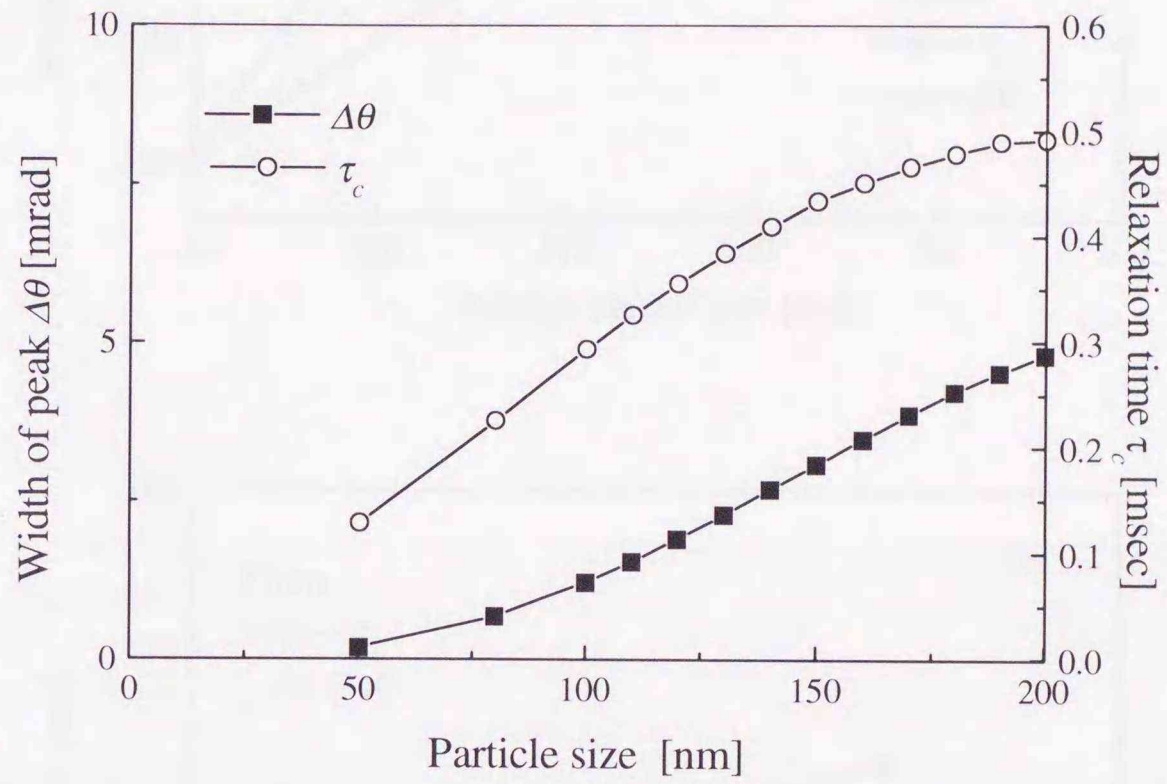

Fig. 9.5 Variations of the angular width of the intensity enhancement and the relaxation time of the temporal autocorrelation function of the light backscattered multiply from the monodisperse random media, as a function of the particle size.

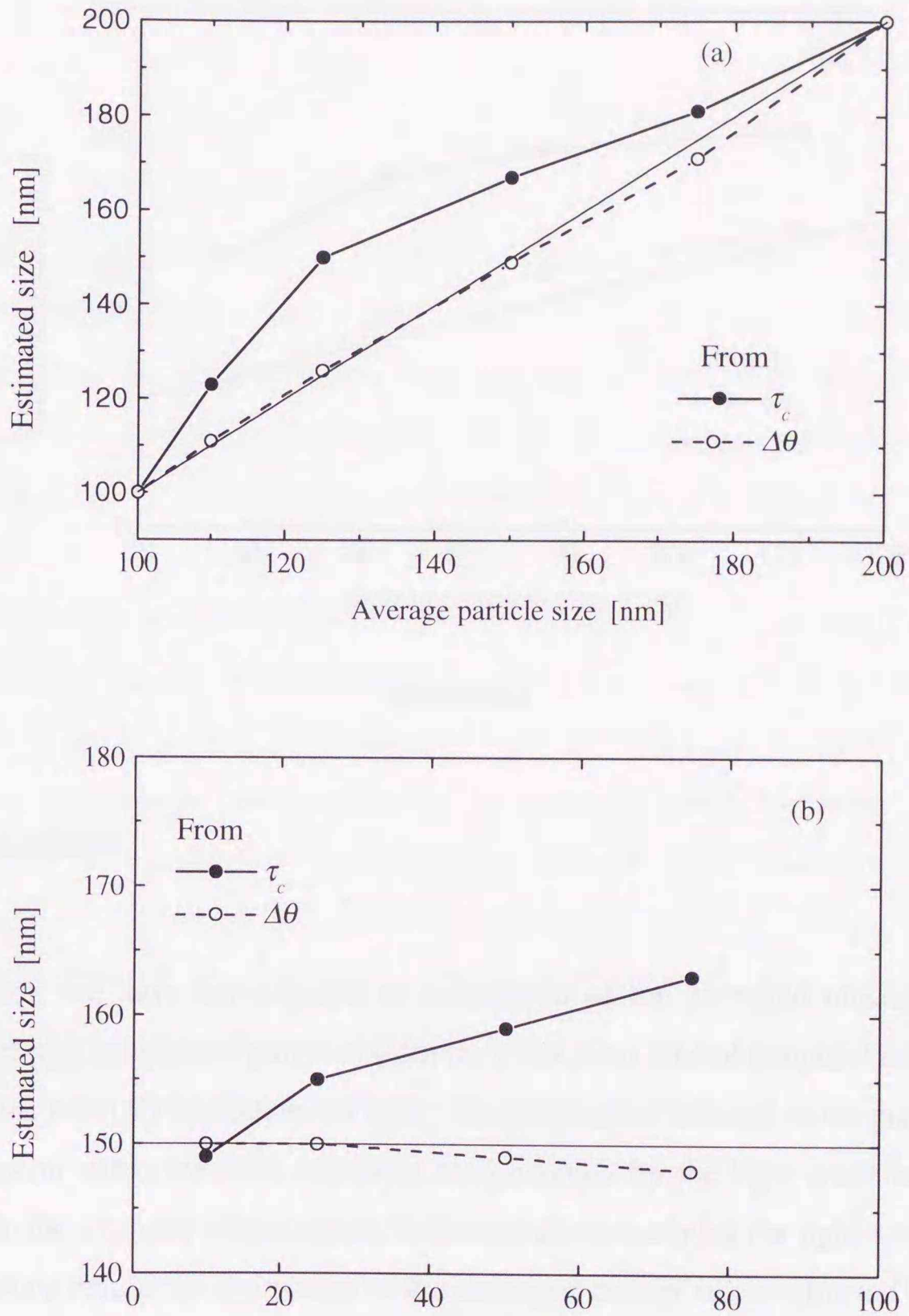

Fig. 9.6 Averaged particle sizes estimated from the light backscattered multiply from the random media which are distributed by following (a) the simple summation of particles with the radii of a_1=100nm and a_2=200nm, (b) the Gaussian distribution with the mean size of 150nm and the standard deviation of σ, and (c) the power law distribution with the exponent α.

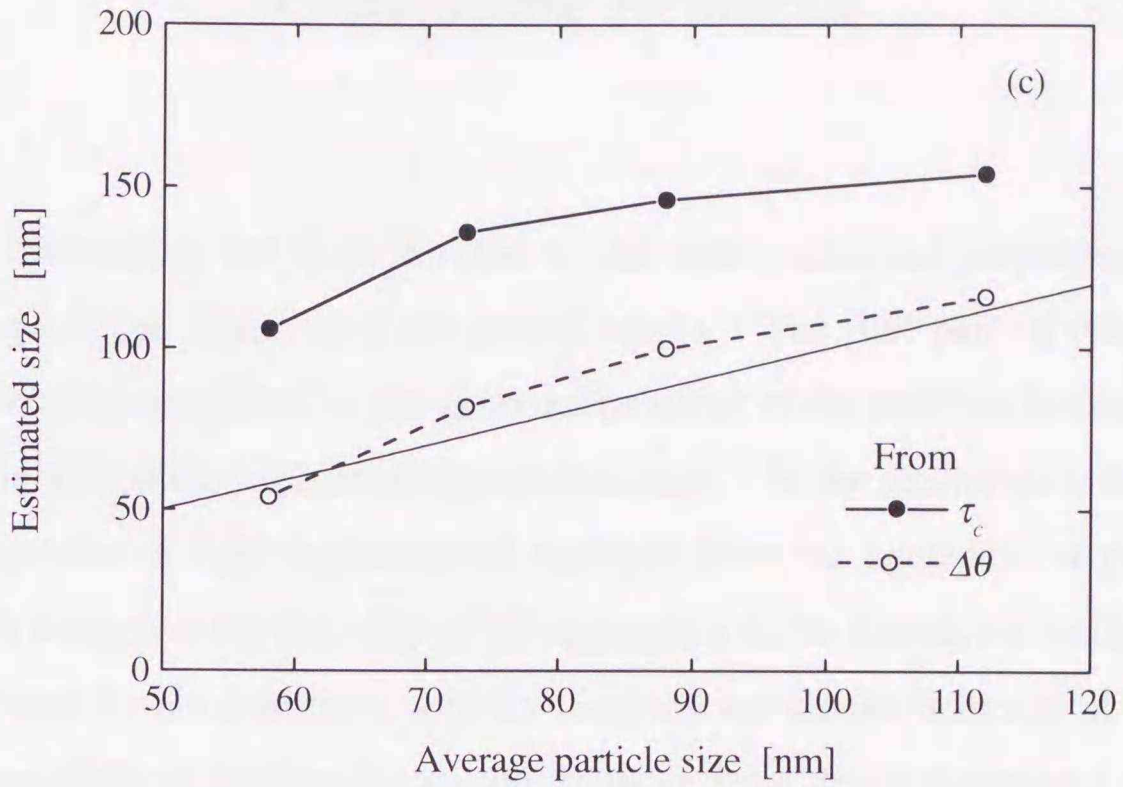

(continued)

9.4 Conclusions

In this chapter, we have investigated an estimation of the averaged cluster size in the cluster-cluster aggregations of particles from the relaxation time of temporal autocorrelation functions of the multiply backscattered light. The motivation is based on the previous results that the temporal autocorrelation functions are governed by the light scattered among the clusters while the intensity enhancement is formed dominantly by the light scattered inside the cluster. As a result, the estimation of the averaged cluster size is affected by the larger size of clusters so that the size is estimated to be larger than the true one. Therefore, the estimated size needs to be compensated by the numerical relation between the relaxation times for a stationary distribution, e.g. the power low distribution, and for the homogeneously random medium with the dimension of D=3 as shown in Fig. 9.6.

Chapter 10

Concluding Remarks

The present dissertation has been devoted to the spatio-temporal properties of coherent backscattering of light from dense disordered media. The first part of this dissertation was dealt with an investigation on the temporal behavior of the multiply backscattered light under the influence of the backscattering enhancement. In the second part, the spatial and temporal properties of light backscattered multiply from the aggregate of particles were surveyed with relation to the fractality of the aggregates in the disordered media.

Chapters 3 and 4 were concerned with the temporal correlation behavior of time-varying intensity fluctuations of light backscattered multiply from dense disordered media. The investigations were conducted with relation to the spatial properties of the backscattering enhancement produced from the interference effect between the scattered wave and its time-reversed counterpart. In chapter 3, the temporal autocorrelation function was theoretically derived by renormalizing the interference effect to the path-length distribution function under the framework of the diffusive transport theory of photons. The theory enabled us to study the characteristic dependence of the relaxation time in multiply-backscattered intensity fluctuation on the backscattering angle. Therefore, it is concluded on the basis of the experimental confirmation that the theory can describe the temporal behavior of the multiply backscattered light under the phenomenon of the backscattering enhancement.

In Chapter 4, the dependence of the angular polarization properties of the temporal autocorrelation function on the particle size was investigated. The temporal autocorrelation functions were calculated by means of the Monte Carlo simulations based on the Rayleigh-Debye scattering theory. The simulations demonstrated successfully the polarization properties in the variation of the relaxation time as a function of the scattering angle obtained experimentally by Qu and Dainty [76]. In addition, we demonstrated the dependence of the angular polarization properties of the relaxation time on the particle size by means of the simulations and confirmed experimentally the simulated results.

Especially, the simulations revealed that the angular polarization behaviors could be clearly interpreted by showing the dependence of the contribution of the coherent component to the copolarized and cross-polarized intensity variations depending on the scattering angle, the scattering order, and the particle size. The criterion in the validity of the present simulation algorithm based on the Rayleigh-Debye scattering theory was shown by the quantitative comparisons between the simulated and the experimental data.

Chapters 5-9 were devoted to the investigations on the coherent backscattering of light from the aggregate of particles with relation to the fractal dimension of the medium. In Chapter 5, a free path-length distribution function (FPDF) of the multiply backscattered light was theoretically derived for the aggregate of particles. The validity of the FPDF was confirmed by demonstrating the agreement between the dimensions designed in particle distributions generated by random walks on the basis of the derived FPDF and estimated by using the radius-gyration method. The FPDF was also applied to Monte Carlo simulations for the light backscattered multiply from the fractal aggregate of particles to demonstrate its applicability. As a result, the angular width with an order of λ/ℓ_D and the θ^{2-D} dependence of peak intensity distribution in the backscattering enhancement have been demonstrated successfully. From the metrological point of view, the results show clearly the applicability of the backscattering enhancement of light to measure the dimension of particle aggregation.

In Chapter 6, the angular intensity distributions of the copolarized and cross-polarized light backscattered multiply from the fractal aggregate of particles were investigated using Monte Carlo simulations. The dependences of the angular width and the decreasing slope of the intensity peak on the dimension of the medium, the effective mean free path-length, and the absorption of the medium were demonstrated. It was revealed that the effective mean free path-length ℓ_D has the same physical meaning as the mean free path-length ℓ for the homogeneously random medium and the backscattering enhancement of light can be applied to estimation of the dimension of the medium. Moreover, by simulating the intensity distributions of copolarized and cross-polarized components in the boundary plane between the scattering medium and the air, the two-dimensional Fourier transform relation between the intensity distributions in the far-field and the boundary planes is shown only for the copolarized component but not for cross-polarized one. This

difference might be attributed to the correlation factor Γ between the lights propagating along the time-forward and -reversed paths in the formation of the cross-polarized intensity.

In Chapter 7, the decreasing variations of the copolarized and cross-polarized peak intensity distributions produced from aggregated particles in the absorbent colloidal suspensions were investigated by experiments. It was shown that the peak intensity distribution changes suddenly as soon as the aggregation of particles happens and the fractal dimension of the medium can be estimated by applying the decreasing slopes to the empirical formulae obtained in Chapter 6. The fractal dimensions estimated from the copolarized and cross-polarized peak intensity distributions characterize the spatial structures of particle distributions over the whole medium and inside a cluster, respectively. Such the decreasing variations of the peak intensity distributions are independent of the absorption of the medium though the peak intensity and width change with the absorption. It was concluded that the analyses on the spatial properties of the backscattering enhancement phenomena in the coherent backscattering of light show the ability to watch the aggregation process of particles and to estimate its dimension for the dense absorbent media.

In Chapter 8, the temporal statistics of light backscattered multiply from the aggregated particles in absorbent media were investigated with relation to the absorption. The temporal autocorrelation functions of the backscattered light in the region of the time longer than the relaxation time depend on the fractal dimension while, in the region of the time less than the relaxation time, they follow the diffusion approximation through the Laplace transform relation between the autocorrelation function and the total path-length distribution function. The angular dependence of the temporal autocorrelation functions for fractal media varies drastically depending on the fractal dimension in comparison with that from homogeneously random media. The influence of the absorption in the media appears as the time shift of the temporal autocorrelation function in such a way that it varies approximately in accordance with a square root of the absorption coefficient and independently of the fractal dimension. It is concluded that that the Diffusive Wave Spectroscopy has an ability of measuring the absorption of fractal media without the influence of the dimension.

In Chapter 9, the estimation of the averaged cluster size in the cluster-cluster aggregation of particles from the relaxation time of temporal autocorrelation functions of the multiply backscattered light was examined numerically by using the renormalization of the cluster-cluster distribution to the particle size distribution. The motivation is based on the results obtained in the previous chapter that the temporal autocorrelation functions follow the radiative transport theory even for fractal media and, thereby, that they depend only on diffusion coefficients of clusters. As a result, the estimation of the cluster size is governed by the larger size of clusters so that the size is estimated to be larger than the true one. Therefore, it was shown that the estimated size needs to be compensated by the numerical relation between the relaxation times for the stationary distribution.

Acknowledgments

I would like to express my sincere appreciation to Prof. T. Asakura for his continuous guidance and encouragement throughout the course of the present work, without which this dissertation would not have been possible. I wish to extend my deepest gratitude to Dr. T. Iwai for his kind encouragement and many helpful suggestions throughout the present work. I also send my appreciation to Profs. N. Nagai, M. Koshiba, T. Mishima, and K. Sasaki for their various advices.

I also wish to acknowledge valuable discussions with Dr. J. Uozumi, Dr, T. Okamoto, Dr. Y. Harada and Dr. H. Yoshimura on various problems. I would like to extend my thanks to Mr. T. Ushizaka for his useful suggestions and technical advice. I am grateful to all the other members at Laboratory of Optical System Engineering for creating a pleasant atmosphere. With support of the above colleagues, the present dissertation has been successfully accomplished.

References

[1] M. Faraday, "Experimental relations of gold (and other metals) to light," Phil. Trans. Roy. Soc. London **147**, 145-181 (1857).

[2] J. Tyndall, "On the blue colour of the sky, the polarization of skylight, and on the polarization of light by cloudy matter generally," Proc. R. Soc. London **17**, 223-233 (1869).

[3] J. Tyndall, "On the action of rays of high refragibility upon gaseous matter," Phil. Trans. Roy. Soc. London **160**, 333-365 (1870).

[4] J. W. S. Rayleigh, "On the light from the sky, its polarization and color," Phil. Mag. **41**, 107-120, 274-279 (1871).

[5] J. W. S. Rayleigh, "On the scattering of light by small particles," Phil. Mag. **41**, 447-454 (1871).

[6] J. W. S. Rayleigh, "On the electromagnetic theory of light," Phil. Mag. **12**, 81-101 (1881).

[7] J. W. S. Rayleigh, "On the transmission of light through an atmosphere containing small particles in suspension, and on the origin of the blue of the sky," Phil. Mag. **47**, 375-384 (1899).

[8] J. W. S. Rayleigh, "The incident light upon a transparent sphere of dimensions comparable with the wave length," Proc. Roy. Soc. A **84**, 25-46 (1910).

[9] J. W. S. Rayleigh, "On the diffraction of light by spheres of small relative index," Proc. Roy. Soc. A **90**, 219-255 (1914).

[10] J. W. S. Rayleigh, " On the scattering of light by spherical shell, and by complete sphere of periodic structure, when the refractivity is small," Proc. Roy. Soc. A **94**, 296-300 (1918).

[11] P. Debye, "Zerstreuum von Röntgenstrahlen," Ann. d. Physik **46**, 809-823 (1915).

[12] R. Gans, "Asymmetric von gasmolekeln. Ein beitragzur Bestimmung der molekularen form," Ann. d. Physik **65**, 97-123 (1921).

[13] R. Gans, "Das tyndallphänomen in Flüssigkeiten," Ann. d. Physik **17**, 353-397 (1923).

[14] R. Gans, "Strahlungsdiagramme ultramikroskopischer teilchen," Ann. d. Physik **76**, 29-38 (1925).

[15] G. Mie, "Beiträge zur Optik Trüber Medien, Speziell kolloidaler Mot- allösungen," Ann. d. Physik **25**, 377-442 (1908).

[16] P. Debye, "Das Verhalten von lichtwellen in der nähe eines brennpunktes oder einer brennlinie," Ann. d. Physik **30**, 755-776 (1909).

[17] H. C. van de Hulst, *Light Scattering by Small Particles*, Dover Publications, New York (1981).

[18] M. Kerker, *The Scattering of Light and other electromagnetic radiation*, Academic Press, INC., San Diego (1969).

[19] N. A. Logan, "Survey of some early studies of the scattering of plane waves by a sphere," in *Selected Papers on Light Scattering*, M. Kerker ed., 3-18, SPIE **951** (1988).

[20] P. Lilienfeld, "Gustav Mie: the person," Appl. Opt. **30**, 4696-4698 (1991).

[21] M. Kerker, "Founding fathers of light scattering and surface-enhanced Raman scattering," Appl. Opt. **30**, 4699-4704 (1991).

[22] M. Smoluchowski, "Molekular-kinetische theorie der opaleszenz von gasen im kritischen zustande, sowie einiger verwandter erscheinung," Ann. d. Physik **25**, 205-226 (1908).

[23] A. Einstein, "Theorie der opaleszenz von homogenen flüssigkeiten und flüssigkeitsgemischen in der Nähe des kritischen zustandes," Ann. d. Physik **33**, 1275-1290 (1910).

[24] L. S. Ornstein and F. Zernike, "accidental deviations of density and opalescence at the critical point," Proc. Acad. Sci.Amsterdam **17**, 793 (1914).

[25] L. S. Ornstein and F. Zernike, "The clustering tendency of the molecules in the critical state and the extinction of light caused thereby," Proc. Acad. Sci.Amsterdam **18**, 1520 (1915).

[26] L. S. Ornstein and F. Zernike, "Bemerkung zur arbeit von herrn k. c. kar: Die molekularzerstreuung des lichtes beim kritischen zustande," Physik Z. **27**, 761-764 (1926).

[27] F. Zernike and T. H. Prins, "Die Beugung von röntgenstrahlen in flüssigkeiten als effekt der molekülanordnung," Z. Physik **41**, 184-194 (1927).

[28] J. Cabannes, *La Diffusion Moleculair de la Lumiere*, Les Presses Universitaires de France, Paris (1929).

[29] D. McIntyre and F. Gornick, *Light Scattering from Dilute Polymer Solution*, Gordon and Breach, New York (1964).

[30] J. Feder, *Fractals*, Plenum Press, New York (1988).

[31] T. Vicsek, *Fractal Growth Phenomena*, World Scientific Publishing, Singapore (1989).

[32] J.Teixeira, "Experimental methods for studying fractal aggregates," in *On Growth and Form*, H. E. Staney and N. Ostrowski, eds., 145-162, Martinus Nijhoff Publishing Dordrecht (1986).

[33] D. W. Schaefer and J. E. Martin, "Fractal Geometry of Colloidal Aggregates," Phys. Rev. Lett. **52**, 2371-2374 (1984).

[34] D. A. Weitz, J. S. Huang, M. Y. Lin, and J. Sung, "Limits of the fractal dimension for irreversible kinetic aggregation of gold colloids," Phys. Rev. Lett., **54**, 1416-1419 (1985).

[35] L. Brillouin, "Diffusion de la limière par un corps transparent homogène," C. R. Acad. Sci. **158**, 1331-1334 (1914).

[36] L. Brillouin, Ann. de Physique **17**, 88 (1922).

[37] L. I. Mandel'shtam, Zh. Russ. Fiz. Khim. Obshchestva **58**, 381 (1926).

[38] E. Gross, "Change of wavelength of light due to elastic heat wave at scattering in liquids," Nature **126**, 201-202 (1930).

[39] E. Gross, "Modification of light quanta by elastic oscillations in scattering media," Nature **128**, 722-723 (1932).

[40] L. D. Landau and G. Placzek, "Struktur der unverschobenen streulinie," Physik Z. Sowjetunion **5**, 172-173 (1934).

[41] C. V. Raman, "A new radiation," Indian J. Phys. **2**, 387-398 (1928).

[42] T. Maiman, "Stimulated optical radiation in ruby," Nature **187**, 493-494 (1960).

[43] R. Pecora, "Doppler shifts in light scattering from pure liquids and polymer solutions," J. Chem. Phys. **40**, 1604-1614 (1964).

[44] H. Z. Cummins, N. Knable, and Y. Yeh, " Observation of diffusion broadening of

Rayleigh-Brillouin spectrum," Phys. Rev. Lett. **12**, 150-153 (1964).

[45] N. C. Ford and G. B. Benedek, " Observation of the spectrum of light scattered from a pure fluid near its critical point," Phys. Rev. Lett. **15**, 649-653 (1965).

[46] B. J. Berne and R. Pecora, *Dynamic Light Scattering*, John Wiley and Sons, New York (1976).

[47] K. S. Schmitz, *An Introduction to Dynamic Light Scattering by Macromolecules*, Academic Press, San Diego (1990).

[48] B. R. Ware and W. H. Flygare, "The simultaneous measurement of the electrophoretic mobility and diffusion coefficient in bovine serum albumin solutions by light scattering," Chem. Phys. Lett. **12**, 81-85 (1971).

[49] B. R. Ware and W. H. Flygare, "Light scattering in mixtures of BSA, BSA dimers and fibrinogen under the influence of electric fields," J. Colloid and Interface Sci. **39**, 670-675 (1972).

[50] A. T. Forrester, R. A. Gudmunsen, and P. O. Johnson, "Photoelectric mixing of incoherent light," Phys. Rev. **99**, 1691-1700 (1955).

[51] A. T. Forrester, "Photoelectric mixing as a spectroscopic tool," J. Opt. Soc. Am. **51**, 253-259 (1961).

[52] Y. Yeh and H. Z. Cummins, "Localized flow measurements with an He-Ne laser," Appl. Phys. Lett. **4**, 176-178 (1964).

[53] E. R. Pike, Riv. Nuovo Cimento, "Photon statistics," Ser. 1 **1**, Numero Speciale, 277-314 (1969).

[54] D. A. Weitz, J. S. Huang, M. Y. Lin, and J. Sung, "Dynamics of diffusion-limited kinetic aggregation," Phys. Rev. Lett., **53**, 1657-1660 (1984).

[55] J. Feder, T. Jossang, and E. Rosenqvist, "Scaling behavior and cluster fractal dimension determined by light scattering from aggregating proteins," Phys. Rev. Lett., **53**, 1403-1406 (1984).

[56] M. Born and E. Wolf, *Principles of Optics*, Macmillan, New York (1964).

[57] P. A. Bello, "Characterization of randomly time-variant linear channels," IEEE Trans. Commun. Syst. **11**, 360-393 (1963).

[58] R. S. Kennedy and S. Karp, "Optical space communication," Proc. Of MIT-NASA Workshop NASA SP-217. U.S. Govt. Printing Office, Washington, D.C. (1969).

[59] L. A. Zadeh, "Frequency analysis of variable networks," Proc. IRE **38**, 291-299 (1950).

[60] A. Ishimaru and S. T. Hong, "Multiple scattering effect on coherent bandwidth and pulse distortion of wave propagation in a random distribution of particles," Radio Sci. **10**, 6, 637-644 (1975).

[61] A. Schuster, "Radiation through a foggy atmosphere," Astrophys. J. **21**, 1-22 (1905).

[62] S. Chandrasekhar, *Radiative Transfer*, Oxford Univ. Press, London (1950).

[63] V. V. Sobolev, *A Treaties on Radiative Transfer*, Van Nostrand-Reinhold, Princeton (1963).

[64] R. W. Preisendorfer, *Radiative Transfer on Discrete Space*, Oxford Univ. Press, London (1965).

[65] D. H. Menzel, ed. *Selected Papers on the Transfer of Radiation*, Dover Publications, New York (1966).

[66] A. Sommerfeld, *Thermodynamics of Statistical Mechanics*, Academic Press, New York (1956).

[67] B. Davison, *Neutron Transport theory*, Oxford Univ. Press, London (1958).

[68] A. Ishimaru, "Correlation function of a wave in a random distribution of stationary and moving scatterers," Radio Sci. **10**, 1, 45-52 (1975).

[69] A. Ishimaru, "Theory and application of wave propagation and scattering in random media," Proc. IEEE **65**, 1030-1061 (1977).

[70] C. C. Johnson, "Optical diffusion in blood," IEEE Trans. **BME-17**, 129-133 (1970).

[71] C. C. Johnson and A. W. Guy, "Normalizing electromagnetic wave effects in biological material and Systems," Proc. IEEE **60**, 6, 692-718 (1972).

[72] L. Reynolds, C. C. Johnson, and A. Ishimaru, "Diffuse reflectance from a finite blood medium: Applications to the modeling of fiber optic catheters," Appl. Opt. **15**, 2059-2067 (1976).

[73] D. J. Pine, D. A. Weitz, P.M. Chaikin, and E. Herbolzheimer, "Diffusing-Wave Spectroscopy," Phys. Rev. Lett. **60**, 1134-1137 (1988).

[74] F. C. Mackintosh and S. John, "Diffusing-wave spectroscopy and multiple scattering of light in correlated random media," Phys. Rev. B **40**, 2383-2406 (1989).

[75] D. J. Pine, D. A. Weitz, G. Maret, P. E. Wolf, E. Herbolzheimer, and P. M. Chaikin, "Dynamic correlations of multiply scattered light," in *Scattering and Localization of Classical Waves in Random Media*, P. Sheng, ed., 312-372, World Scientific Publishing, Singapore (1990).

[76] D. N. Qu and J. C. Dainty, "Polarization dependence of dynamic light scattering by dense disordered media," Opt. Lett. **13**, 1066-1068 (1988).

[77] T. Iwai and J. C. Dainty, "Pathlength distribution function of dynamic multiple light backscattering in dense disordered media," in *Photon Correlation and Scattering: Theory and Applications* Technical Digest **20**, 50-52, Optical Society of America, Washington, D. C. (1992).

[78] P. Sheng, *Introduction to Wave Scattering, Localization, and Mesoscopic Phenomena*, Chap. 5, 177-192, Academic Press, San Diego (1995).

[79] X. L. Wu, D. J. Pine, J. S. Huang, P. M. Chaikin, and D. A. Weitz, "Diffusing-wave spectroscopy in a shear flow," J. Opt. Soc. Am. B **7**, 15-20 (1990).

[80] D. Bicout, E. Akkermans, and R. Maynard, "Dynamical correlations for multiple light scattering in laminar flow," J. Phys. I **1**, 471-491 (1991).

[81] J. W. Ryde, "The scattering of light by turbid media—Part I," Proc. Roy. Soc. London Ser. A **131**, 451-464 (1931).

[82] J. W. Ryde and B. S. Cooper, "The scattering of light by turbid media—Part II," Proc. Roy. Soc. London Ser. A **131**, 464-475 (1931).

[83] L. O. Foldy, "The multiple scattering of waves," Phys. Rev. **67**, 3, 4, 107-119 (1945).

[84] M. Lax, "Multiple scattering of waves," Rev. Mod. Phys. **23**, 4, 287-310 (1951).

[85] H. S. Snyder and W. T. Scott, "Multiple scattering of fast charged particles," Rev. Phys. **76**, 220-225 (1949).

[86] V. Twersky, "On propagation in random media of discrete scatterers," Proc. Am. Math. Soc. Symp. Stochas. Proc. Math. Phys. Eng. **16**, 84-116 (1964).

[87] J. B. Keller, "Stochastic equation and wave propagation in random media," Proc Symp. Appl. Math. **16**, 145-170 (1966).

[88] V. Twersky, "Interference effects in multiple scattering by large, low-reflecting, absorbing particles," J. Opt. Soc. Am. **60**, 908-914 (1970).

[89] V. Twersky, "Absorbing and multiple scattering by biological suspensions" J. Opt. Soc. Am. **60**, 1084-1093 (1970).

[90] V. Twersky, "Mutiple scattering of sound by a periodic line of obstacles" J. Acoust. Soc. Am. **53**, 1, 96-112 (1973).

[91] V. Frisch, "Wave propagation in romdom media", in *Probabilistic Method in Applied Mathematics*, **1**, 76-198, Academic Press, New York (1968).

[92] N. Marcuvitz, "On the theory of plasma turbulence," J. Math. Phys. **15**, 869-879 (1974).

[93] Y. Kuga and A. Ishimaru, "Retroreflectance from a dense distribution of spherical particles," J. Opt. Soc. Am. A **1**, 831-835 (1984).

[94] L. Tsang and A. Ishimaru, "Backscattering enhancement of random discrete scatterers," J. Opt. Soc. Am A**1**, 836-839 (1984).

[95] M. P. van Albada and A. Lagendijk, "Observation of weak localization of light in a random medium," Phys. Rev. Lett. **55**, 2692-2695 (1985).

[96] P. -E. Wolf and G. Maret, "Weak localization and coherent backscattering of photons in disordered media," Phys. Rev. Lett. **55**, 2696-2699 (1985).

[97] M. J. Stephen and G. Cwilich, "Rayleigh scattering and weak localization: Effects of polarization," Phys. Rev. B **34**, 7564-7572 (1986).

[98] S. Etemad, "Coherent backscattering of light by disordered media: The vector nature of a photon," Phys. Rev. B **37**, 3652-3653 (1988).

[99] T. Iwai, H. Furukawa, and T. Asakura, "Numerical analysis on enhanced backscatterings of light based on Rayleigh-Debye scattering theory," Opt. Rev. **2**, 413-419 (1995).

[100] E. Akkermans, P. -E. Wolf, R. Maynard, and G. Maret, "Theoretical study of the coherent backscattering of light by disordered media," J. Phys. (France) **49**, 77-98 (1988).

[101] G. Maret and P. -E. Wolf, "Multiple light scattering from disordered media. The effect of Brownian motion of scatterers," Z. Phys. B **65**, 409-413 (1987).

[102] M. P. van Albada, M. B. van der Mark, and A. Lagendijk, Phys. "Observation of Weak Localization of Light in a Finite Slab: Anisotropy Effects and Light-Path Classification," Rev. Lett. **58**, 361-364 (1987).

[103] M. P. van Albada and A. Lagendijk, "Vector character of light in weak localization: Spatial anisotropy in coherent backscattering from a random medium," Phys. Rev. B **36**, 2353-2356 (1987).

[104] K. Ishii, T. Iwai, and T. Asakura, "Angular dependence of enhanced backscatterings of light by the Brownian dynamics under the diffusive transport theory of photons," J. Opt. Soc. Am. A **14**, 179-184 (1997).

[105] P. E. Wolf and G. Maret, "Dynamics of Brownian particles from strongly multiple light scattering", in *Scattering in Volumes and Surfaces*, M. Nieto-Vesperinas and J. C. Dainty, eds., 37-52, North-Holland, Amsterdam (1990).

[106] M. P. van Albada, M. B. van der Mark, and A. Lagendijk, "Polarisation effects in weak localisation of light," J. Phys. D: Appl. Phys. **21**, 28-31 (1988).

[107] J. Stratton, *Electromagnetic Theory*, McGraw-Hill, New York (1941).

[108] A. Ishimaru, *Wave Propagation and Scattering in Random Media*, Academic Press, San Diego (1978).

[109] W. H. Press, B. P. Flannery, S. A. Teukolsky, and W. T. Vetterling, *Numerical Recipes in C* , Chap. 14, 540-547, Cambridge Univ. Press, New York (1998).

[110] J. E. Martin and B. J. Ackerson, "Static and dynamic scattering from fractals," Phys. Rev. A **31**, 1180-1182 (1985).

[111] J. Teixeira, "Small-angle scattering by fractal systems," J. Appl. Cryst. **21**, 781-785 (1988).

[112] C. M. Sorensen, J. Cai, and N. Lu, "Light-scattering measurements of monomer size, monomers per aggregate, and fractal dimension for soot aggregates in flames," Appl. Opt. **31**, 6547-6557 (1992).

[113] Z. -Y. Chen, P. Weaklien, W. M. Gelbart, and P. Meakin, "Second-order light scattering and local anisotropy of diffusion-limited aggregates and bond-percolation clusters," Phys. Rev. Lett. **58**, 1996-1999 (1987).

[114] A. Dogariu, J. Uozumi, and T. Asakura, "Enhancement of backscattered intensity from fractal aggregates," Waves Random Media **2**, 259-263 (1992).

[115] A. Dogariu, J. Uozumi, and T. Asakura, "Source of error in optical measurements of fractal dimension," Pure Appl. Opt. **2**, 339-350 (1993).

[116] B. C. Wilson and G. Adam, "A Monte Carlo model for the absorption and flux distributions of light in tissue," Med. Phys. 10, 824-830 (1983).

[117] Y. Hasegawa, Y. Yamada, M. Tamura, and Y. Nomura, "Monte Carlo simulation of light transmission through living tissues," Appl. Opt. **30**, 4515-4520 (1991).

[118] K. Ishii, T. Iwai, and T. Asakura, "Angular polarization properties of dynamic light scattering under influence of enhanced backscatterings," Opt. Commun. **140**, 99-109 (1997).

[119] D. Schmeltzer and M. Kaveh, "Back-scattering of electromagnetic waves in random dielectric media," J. Phys. C: Solid State Phys. **20**, L175-L179 (1987).

[120] M. Rosenbluh, I. Edrei, M. Kaveh, and I. Freund, "Precision determination of the line shape for coherently backscattered light from disordered solids: Comparison of vector and scalar theories," Phys. Rev. A **35**, 4458-4460 (1987).

[121] E. Akkermans, P.E. Wolf, and R. Maynard, "Coherent backscattering of light by disordered media: analysis of the peak line shape." Phys. Rev. Lett. **56**, 1471-1474 (1986).

[122] T. Iwai, K. Ishii and T. Asakura, "Coherent backscattering of light from a polydisperse random medium as a model of fractal aggregations of particles," Proc. SPIE **3252** (1998) (in press).

[123] K. Ishii, T. Iwai, and T. Asakura, "Polarization properties of the enhanced backscattering of light from the fractal aggregate of particles," Opt. Rev. **4**, 643-647 (1997).

[124] K. Ishii, T. Iwai, and T. Asakura, "Free pathlength distribution function of enhanced backscattering light from fractal aggregates," Appl. Opt. **37** (1998) (in press).

[125] F. C. Mackintosh and S. John, "Diffusing-wave spectroscopy and multiple scattering of light in correlated random media," Phys. Rev. B **40**, 2383-2406 (1989).

[126] K. Ishii, T. Iwai, and T. Asakura, "Monte Carlo simulations of the polarization anisotropy in light backscattered from a fractal aggregation," Proc. SPIE **2979**, 566-573 (1997).

[127] T. Iwai and J. C. Dainty, "Pathlength distribution function of dynamic multiple light backscattering in dense disordered media," Opt. Soc. Am. Tech. Digest, **20**, 50-52 (1992).

[128] K. Katayama, G. Nishimura, M. Kinjo, and M. Tamura, "Absorbance measurements in turbid media by photon correlation method," Appl. Opt. **34**, 7419-7427 (1995).

[129] K. S. Schmitz, *An Introduction to Dynamic Light Scattering by Macromolecules*, Academic Press, San Diego (1990).

[130] W. Feller, *An Introduction to Probability Theory and Its Applications*, John Wiley and Sons, New York (1966).

[131] H. Takayasu, *Fractals in the Physical Sciences*, Manchester Univ. Press, Manchester (1990).

List of works by the author

[1] K. Ishii, T. Iwai, and T. Asakura, "Angular dependence of enhanced backscattering of light by Brownian dynamics in the diffusive transport theory of photons," J. Opt. Soc. Am. A, Vol.**14**, No. 1, pp. 179-184 (1997).

[2] K. Ishii, T. Iwai, and T. Asakura, "Angular polarization properties of dynamic light scattering under influence of enhanced backscatterings," Opt. Commun., Vol.**140**, pp. 99-109 (1997).

[3] K. Ishii, T. Iwai, and T. Asakura, "Polarization properties of the enhanced backscattering of light from the fractal aggregate of particles," Opt. Rev., Vol **4**, No.4, pp.643-647 (1997).

[4] K. Ishii, T. Iwai, J. Uozumi, and T. Asakura, "Free pathlength distribution function of enhanced backscattering light from fractal aggregates," Appl. Opt., Vol **37** (in press).

[5] K. Ishii, T. Iwai, and T. Asakura, "Correlation properties of light backscattered multiply from fractal aggregates of particles under Brownian motions," Bio. Med. Opt. (to be submitted).

[6] K. Ishii, T. Iwai, and T. Asakura, "Experimental study on the backscattering enhancement of light produced from aggregated and non-aggregated particles in colloidal suspension" (to be submitted).

[7] K. Ishii, T. Iwai, and T. Asakura, "Space-time properties of the enhanced backscattering from highly disordered media," Proc. Int. Soc. Opt. Eng., Vol. **2778**, pp. 379-380 (1996).

[8] K. Ishii, T. Iwai, J. Uozumi, and T. Asakura, "Weak localization of light backscattered multiply from fractal media," Proc. Int. Soc. Opt. Eng., Vol. **2778**, pp. 292-293 (1996).

[9] T. Iwai, K. Ishii, H. Furukawa, M. Dogariu, and T. Asakura, "Polarization anisotropy in near-field intensity patterns scattered multiply from dense random media," Proc. Int. Soc. Opt. Eng., Vol. **2778**, pp. 313-314 (1996).

[10] T. Iwai, K. Ishii, and T. Asakura, "Space-time statistics of the coherent light

backscattered from fractal and nonfractal random media with absorption," Proc. Int. Soc. Opt. Eng., Vol. **2982**, pp. 104-115 (1997) (invited).

[11] K. Ishii, T. Iwai, and T. Asakura, "Monte Carlo simulations of the polarization anisotropy in light backscattered from a fractal aggregation," Proc. Int. Soc. Opt. Eng., Vol. **2979**, pp. 566-573(1997).

[12] T. Iwai, K. Ishii, and T. Asakura, "Coherent backscattering of light from a polydisperse random medium as a model of fractal aggregations of particles," Proc. Int. Soc. Opt. Eng., Vol. **3252**, (1998) (in press).

[13] K. Ishii, T. Iwai, and T. Asakura, "Experimental study on the backscattering enhancement of light produced from fractal aggregates of particles", Proc. of Topical Meeting of the International Commission for Optics (ICO) "Optics for Information Infrastructure" OII'98 (in press).

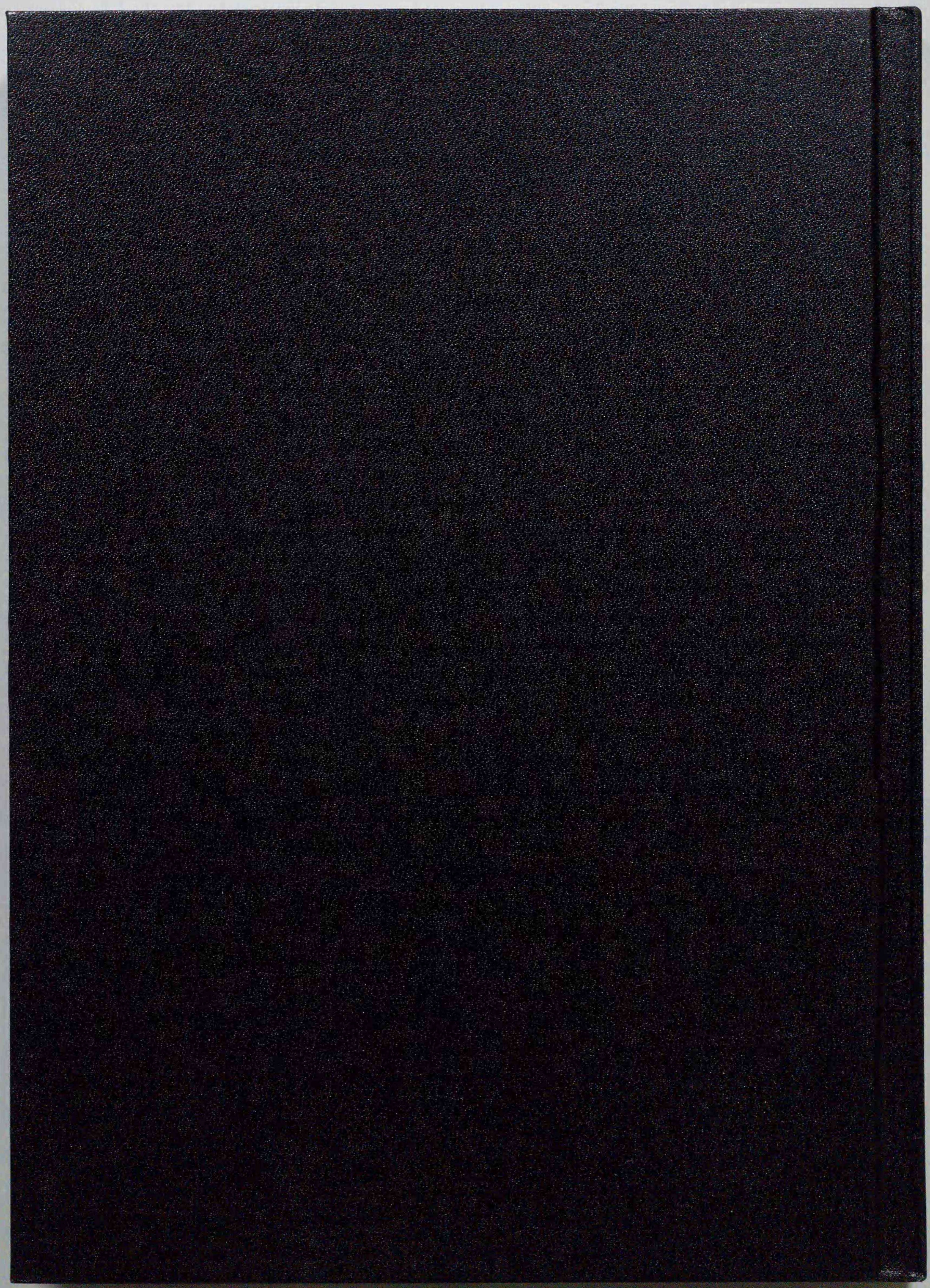

inches 1 2 3 4 5 6 7 8

cm 1 2 3 4 5 6 7 8 9 10 11 12 13 14 15 16 17 18 19

Kodak Color Control Patches

Blue Cyan Green Yellow Red Magenta White 3/Color Black

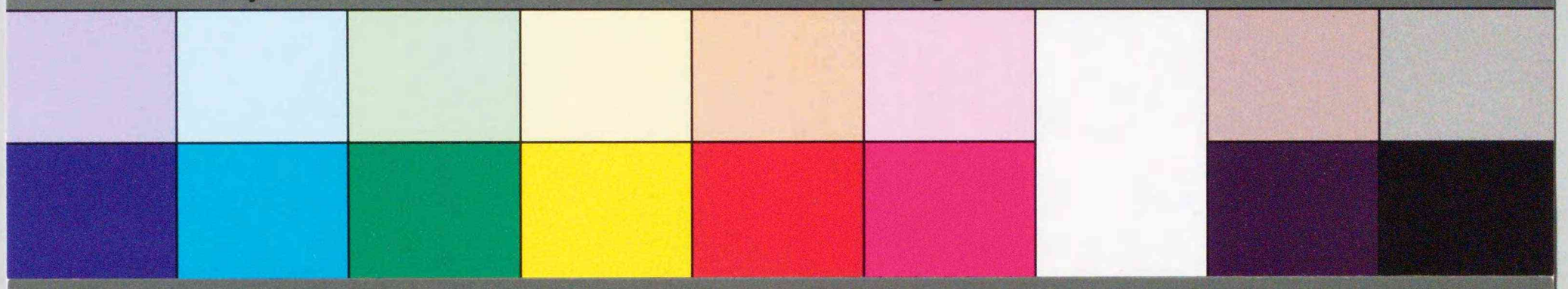

Kodak Gray Scale

C Y M

A 1 2 3 4 5 6 **M** 8 9 10 11 12 13 14 15 **B** 17 18 19